12-2015

Picosecond Time-Resolved Studies of Multiple Energy Transfer in Conjugated Polymer Nanoparticles

Louis Charles Groff II
Clemson University, lgroff@g.clemson.edu

PICOSECOND TIME-RESOLVED STUDIES OF MULTIPLE ENERGY TRANSFER IN CONJUGATED POLYMER NANOPARTICLES

A Dissertation
Presented to
the Graduate School of
Clemson University

In Partial Fulfillment
of the Requirements for the Degree
Doctor of Philosophy
Chemistry

---

by
Louis Charles Groff II
December 2015

Accepted by:
Dr. Jason D. McNeill, Committee Chair
Dr. Steven J. Stuart
Dr. Dvora Perahia
Dr. Brian Dominy

ABSTRACT

Conjugated polymer nanoparticles (CPNs) are a model system for the study of complex, nanoscale, multichromophoric interactions. In this dissertation, we are focused on furthering our understanding of the physical picture, processes, length scales, and time scales of energy transport in conjugated polymers. In particular, we are interested in determining how parameters related to the nanoscale structure and composition of CPs affect energy transport, which is investigated using steady-state and time-resolved fluorescence spectroscopy in conjunction with Monte Carlo simulation methods. Such information could prove useful for optimizing the structure and composition of device layers (e.g., in photovoltaic devices). We additionally seek to develop brighter, red-emitting CPNs through Förster Resonance Energy Transfer (FRET) for their use in biomedical imaging applications. Analysis of dye-doped and polymer blended CPNs shows that the doped CPNs exhibit bright, red-shifted emission, owing to the highly efficient energy transfer from the host polymer PFBT to the respective dopants (the fluorescent dye perylene red in dye-doped CPNs, and the polymer MEH-PPV in blended CPNs). An exciton diffusion energy transfer model was employed to simulate exciton dynamics in doped CPNs, and additionally to determine the intrinsic exciton diffusion length for PFBT in the absence of quenching defects. Solvent-induced swelling methods were utilized to study how swelling affects the multiple energy transfer cascade to intrinsic defects and/or aggregate species in CPNs, which modulates the exciton dynamics and fluorescence properties of CPNs. Changes in the rate of exciton transport over a range of solvent compositions were measured using picosecond fluorescence

anisotropy decay (FAD). Analysis of the results indicates increased fluorescence lifetimes and fluorescence quantum yield with increasing THF concentration. Additionally, the FAD and model results indicate that the rate of exciton transport is significantly increased in the nanoparticle state compared to polymer in good solvent. The results elucidate a tradeoff between exciton transport rates and fluorescence quantum efficiency in conjugated polymer systems, which can be exploited for improvement of organic semiconductor-based devices.

ACKNOWLEDGMENTS

I would first like to thank my research advisor Dr. Jason D. McNeill for all that he has helped me to accomplish in the last six years at Clemson University. He is an excellent example of a committed, hard-working researcher, and a kind and patient mentor. His clever ideas in the laboratory along with his patience and guidance have led me to learn invaluable skills in the laboratory, and to understand and achieve more than I thought possible in my time in graduate school.

I would like to thank the current and previous graduate students, as well as the previous post-doctoral fellows in the McNeill group who helped to make my experience in the group more enjoyable. It has been a pleasure to work with all of you. I would like to express my gratitude to Chuck Sisson and Dr. Jennifer Grimland for showing me the ropes in my early years in the group, and to Dr. Xiaoli Wang and Yifei Jiang both for their friendship, and for their assistance in my research projects.

I also want to thank Dr. Brian Dominy, Dr. Steven Stuart, and Dr. Dvora Perahia for their education, support, and encouragement in my time at Clemson. They have been excellent sources of knowledge, and provided unique perspectives on my research, making them invaluable to my learning experience.

I would also like to thank my loving wife, Emily, for her unending support throughout the last six years. She has been an excellent motivator, both by example in her own educational pursuits, and through her patience and encouragement when progress seemed to elude me.

Lastly, I would like to thank my family and the countless friends both near and far who have been a part of my life throughout my graduate education. You have all made my graduate experience easier with good times, laughter, and sometimes the simple reminder that there is life beyond graduate school to look forward to.

TABLE OF CONTENTS

Page

Table of Contents (Continued)

Page

LIST OF TABLES

LIST OF FIGURES

List of Figures (Continued)

Figure Page

List of Figures (Continued)

Figure Page

List of Figures (Continued)

Figure Page

CHAPTER ONE

OVERVIEW

1.1 Introduction

Conjugated polymers (CPs) are a class of organic semiconducting materials that have been widely studied over the past few decades, owing to their use as active materials for low-cost photovoltaic (PV) and light-emitting diode (LED) technologies.[1-4] These materials exhibit efficient emission in the UV and visible spectrum (fluorescence quantum yields ranging from ~30% to nearly 80%),[5,6] as well as efficient energy and charge transport.[7,8] The observed fluorescence emission in the UV-visible spectrum is due to the extended π-conjugation along the polymer backbone, as well as the structure and heteroatoms that comprise each monomer unit.[9-11] In order to tune conjugated polymers toward specific applications (e.g., fluorescent probes and/or devices), it is necessary to further understand the complex photo physics and amplified energy transport phenomena that are often observed in disordered CP aggregates such as thin films. Specifically, it is advantageous to understand how intrinsic defects and polymer structure and conformation affect the fluorescence properties of CPs. Conjugated polymer nanoparticles (CPNs) exhibit similar photo physics to those of CP thin films, but provide a more reliable means of controlling nanoscale interactions (e.g., energy transport to lower energy chromophores, defects, molecular ions, and/or weakly-emissive aggregates) that lead to heterogeneous dynamics in CPs.

Many fluorescence imaging applications such as particle tracking and biological imaging methods require high brightness to ensure adequate signal-to-noise ratios, high

photostability for experiments requiring high excitation powers and/or extended acquisition times, and red-shifted emission to overcome background autofluorescence signals from biological media and optical components.[12] CPNs meet (or exceed) the requirements for a wide variety of fluorescence imaging applications. In addition to possessing small (4-30 nm) particle diameters, CPNs are easily doped,[11,13] functionalized,[14] and encapsulated,[15] providing exceptional control over both emission wavelength and surface properties for biological imaging applications. The photostability figures of merit for CPNs such as ~10^9 photons emitted prior to irreversible photobleaching and photobleaching quantum yields of ~10^{-9} are 2 to 3 orders of magnitude better than inorganic semiconductor quantum dots and dye-labeled proteins.[14] In addition, CPNs exhibit exceptional absorption and fluorescence characteristics, including extinction coefficients of ~10^9 M^{-1} cm^{-1}, absorption and fluorescence cross sections of ~10^{-13} cm^2, and radiative rates of ~10^8 photons/s.[16-18] The ratio of fluorescence cross-section to particle volume indicates that CPNs are the brightest fluorescent probes of their size (<15 nm) to date, 1-2 orders of magnitude brighter than dye-loaded silica nanoparticles, CdSe and CdSe/ZnS quantum dots, and fluorescent proteins of comparable volume (e.g., green fluorescent protein and phycoerythrin).[16] However, improvements in nanoparticle fluorescence quantum yield and red-shifting of emission are still required for effective use in complex biological samples to ensure sufficient signal-to-noise ratios and to overcome background fluorescence inherent in biological media. [12]

1.2 Frenkel Excitons in Conjugated Polymers

The absorption and emission of conjugated polymers in the UV and visible spectrum arises from the extended π-conjugation (alternating single and double bonds) along the polymer backbone.[10] π-conjugation leads to delocalized electrons over several monomer units, which make up a chromophore (typically 2-8 monomer units in CPs and CPNs, depending on conjugation length). Upon absorption of a photon, an electron is excited from the π to π* electronic band, generating a neutral excitation that is shared along several chromophores (via strongly coupled chromophore transition dipoles), known as a Frenkel (or molecular) exciton.[19]

Transition dipole coupling strength determines the extent to which excitons form in CPs, as well as effective exciton size in CPs. Also, transition dipole coupling is a critical component of the various energy transport processes observed in CPs, such as Förster resonance energy transfer or FRET (termed homo-FRET for molecules that are energetically degenerate or hetero-FRET for non-degenerate molecules, discussed below), as well as coherent energy transfer between degenerate molecules, depending on the magnitude of the coupling strength, temperature, and the amount of disorder in the polymer. What follows is a presentation of a simplified theory for Frenkel-like excitons, based loosely on the theory as presented in a review by Kasha et al.,[20] but omitting several higher-order effects and expressed in more modern notation. Here the discussion is limited to the basic features, key interactions, and some of the key phenomena such as Davydov splitting, "dark" excitons, and delocalized excitations or coherent energy transport. More rigorous, extensive, higher-level discussions including many phenomena not discussed here are provided by Silinsh and Capek [21] and Pope and Swenberg.[22]

In CPs, chromophores are formed as a result of the delocalization of p_z orbitals between sp^2-hybridized atoms, and chromophore size is dictated by the conjugation length of the polymer (typically 2-10 monomers per chromophore). Then, interactions between transition dipoles of two or more like chromophores result in Frenkel (or molecular) excitons,[19] which can be described using perturbation theory. The coupling strength is quantified via the perturbation to the energy of the electronic states of the interacting chromophores. The following is a variant on a dimer model used to describe aggregates. The notation and approach is based on two-state perturbation theory as given by Atkins and Friedman.[23] This approach is valid for non-degenerate chromophores (which describes energy transfer to a dopant, or energy transfer between weakly coupled chromophores in the presence of significant disorder), as well as degenerate chromophores (i.e., excitons). The Hamiltonian $\hat{H}$ is defined as

$$\hat{H} = \hat{H}^{(0)} + \hat{V}, \tag{1.1}$$

where $\hat{H}^{(0)}$ is the zero-order (unperturbed) Hamiltonian and $\hat{V}$ is the perturbation to the system. For two non-interacting chromophores a and b, the states are given by $|a^{(0)}\rangle$, $|b^{(0)}\rangle$ with site energies given by $H^{(0)}|a^{(0)}\rangle = E_a^{(0)}|a^{(0)}\rangle$ and $H^{(0)}|b^{(0)}\rangle = E_b^{(0)}|b^{(0)}\rangle$ respectively (note: for degenerate chromophores, $E_a^{(0)} = E_b^{(0)}$). Next we introduce a perturbation representing the interaction between the sites. In the case of two interacting (transition) dipoles, we can represent the interaction potential (perturbation) as

$$\hat{V} = V_{ad}\{|a^{(0)}\rangle\langle b^{(0)}| + |b^{(0)}\rangle\langle a^{(0)}|\}, \tag{1.2}$$

where V_{dd} is the transition dipole coupling strength. Once the perturbation is applied, the perturbed wavefunctions that describe the system are given by linear combinations of the zero-order wavefunctions of the general form

$$|+\rangle = c_a|a^{(0)}\rangle + c_b|b^{(0)}\rangle, \tag{1.2}$$

and

$$|-\rangle = c_a|a^{(0)}\rangle - c_b|b^{(0)}\rangle, \tag{1.3}$$

where c_a and c_b are constants. For non-degenerate chromophore interactions, the wavefunctions for the mixed state depend on the coupling strength and the chromophore energy difference $\Delta E^{(0)}$, given by

$$|+\rangle = |a^{(0)}\rangle + \frac{|V_{dd}|}{\Delta E^{(0)}}|b^{(0)}\rangle, \tag{1.4}$$

and

$$|-\rangle = |b^{(0)}\rangle + \frac{|V_{dd}|}{\Delta E^{(0)}}|a^{(0)}\rangle \tag{1.5}$$

(it should be noted that the expressions for $|+\rangle$, $|-\rangle$ are not normalized), with energies

$$E_+ = E_a^{(0)} + \frac{V_{dd}^2}{\Delta E^{(0)}}, \tag{1.6}$$

and

$$E_- = E_b^{(0)} - \frac{V_{dd}^2}{\Delta E^{(0)}}. \tag{1.7}$$

Thus, the strength of the perturbation (which gives the amount of wavefunction mixing in Equations 1.4 and 1.5, and the magnitude of the energy shift in Equations 1.6 and 1.7) depends upon the magnitude of the coupling strength and the energy difference between chromophores. The weakly mixed state that results from the perturbation (either $|+\rangle$ or $|-\rangle$) depends on which of the mixed states is lower in energy (and which chromophore is

lower in energy), since both homo-FRET and hetero-FRET occur from a higher energy chromophore to the lower energy chromophore.

For a degenerate two-state system (which is a reasonable description of interactions between excited states on identical interacting chromophores), the first-order exciton states are determined by symmetry, given by

$$|+\rangle = \frac{1}{\sqrt{2}}\left[|a^{(0)}\rangle + |b^{(0)}\rangle\right], \tag{1.8}$$

and

$$|-\rangle = \frac{1}{\sqrt{2}}\left[|a^{(0)}\rangle - |b^{(0)}\rangle\right]. \tag{1.9}$$

The first-order energies $E_{\pm}$ are then given by:

$$E_{+} = E^{(0)} + V_{dd}, \tag{1.10}$$

and

$$E_{-} = E^{(0)} - V_{dd}. \tag{1.11}$$

Thus, the perturbation acting on a set of degenerate (or nearly degenerate) electronic states results in fairly complete mixing of the wavefunctions, as well as increased splitting of the previously degenerate energy levels of the individual chromophores sharing the excitation. By extending this approach to a large number of chromophores, the splitting increases to a limiting value: the Davydov splitting.[24] The resulting Davydov splitting leads to energy shifting of the UV-Vis and fluorescence spectra of CPs in the nanoparticle or thin film state due to interchain and/or intrachain interactions. Given the total dipole moment operator

$$\hat{\mu} = \mu\{|a^{(0)}\rangle\langle a^{(0)}| + |b^{(0)}\rangle\langle b^{(0)}|\}, \tag{1.12}$$

calculation of the modulus squared of the total dipole moment, $|\langle \pm|\hat{\mu}|\pm\rangle|^2$ yields the transition dipole moment μ_{TD}, and determines whether or not a given exciton state ($|+\rangle$ or $|-\rangle$) contributes to the emission signal. If the transition dipole moment is nonzero, emission is allowed from the respective state ($\mu_{TD} = 0$ corresponds to a forbidden transition, or dark exciton state), and is the basis of the spectral characteristics of H- and J-aggregates (i.e., they are different principal general types of excitons). Favorable arrangements of transition dipole moments between coupled chromophores yield emission from the lower energy $|+\rangle$ state in J-aggregates, with the $|-\rangle$ state being a dark exciton state (with the reverse relationship for H-aggregates). Other phenomena that result from favorable arrangements of transition dipoles are superradiance and fluorescence line-narrowing. Superradiance is typically observed in J-aggregates (both polymer J-aggregates such as PPVs, and small molecule J-aggregates such as pseudoisocyanine/PIC), due to excellent overlap between J-aggregate absorption and emission (for strong transition dipole coupling), resulting in an *N*-fold increase in the radiative rate, where *N* is the number of coupled chromophores.[25-27] Fluorescence line-narrowing is an effect of strong transition dipole coupling in conjunction with strong excitation, in which the emission spectrum of an aggregate collapses into a superradiant, narrow peak.[28,29]

Thermal effects (thermal disorder) as well as packing disorder, conformational disorder, and energetic disorder lead to partial localization of excitons. The localized excitons are able to migrate along or between polymer chains via several processes, including incoherent processes such as Förster resonance energy transfer (FRET) and

Dexter energy transfer (described in detail in section 1.3), or by coherent energy transfer (i.e., if the thermal or energetic disorder is weak relative to the dipole-dipole coupling strength); all of these processes encompass what is often referred to as "exciton diffusion,"[30] or multiple energy transfer. These terms will be used interchangeably in this dissertation. The contributions from each transport process occur on differing length scales and time scales. Coherent transport occurs in disordered CPs over short lengths and subpicosecond time scales, whereas incoherent transport occurs over longer (2-5 nm) lengths and on the time scale of ps or greater. It is likely that a mixture of both coherent and incoherent transport occurs in disordered CP systems, in which there is mostly coherent ET between the chromophores within a given weakly localized or partially delocalized exciton, followed by one or more incoherent energy transfer events during the excited state lifetime.

Coherent energy transfer is understood by calculating the time-dependent probability of energy transfer between strongly coupled, degenerate chromophores. For the aforementioned two-molecule system, the probability amplitude of an excitation transferring from a chromophore in state $|a\rangle$ to a degenerate chromophore in state $|b\rangle$ is given by

$$A(t) = \left\langle b \middle| \exp\left(\frac{iHt}{\hbar}\right) \middle| a \right\rangle = \frac{1}{2}[\exp(i\omega t) - \exp(-i\omega t)] = isin(\omega t), \qquad (1.13)$$

where $\omega = V_{dd}/\hbar$, and $\hbar$ is the reduced Planck constant $h/2\pi$. The resulting tunneling probability is given by $|A(t)|^2 = sin^2(\omega t)$. Thus, the probability of finding the excited state electron on one of the participating chromophores oscillates back and forth between the coupled chromophores with an energy transfer rate constant of $k_{et} = V_{dd}/\hbar$. This

tunneling process occurs on the femtosecond time scale, and represents the strong coupling or coherent limit and is a good approximation as long as thermal disorder and energetic disorder are low relative to the coupling strength. Given a set of chromophores with strongly coupled transition dipoles, an excitation on one of the chromophores will yield an oscillating excitation across the set of interacting chromophores. Förster transfer between identical chromophores involves the same basic physical picture, but thermal or energetic disorder breaks up the coherence and the mixing of the states (introduces additional frequencies in Eq. 1.13), and the resulting transport process is better described as excitation localized on a single chromophore undergoing hopping via an incoherent process. It is important to note that the underlying physical picture and interactions are the same for homo-FRET and the Frenkel picture, and that there is no clear demarcation between when homo-FRET becomes coherent transfer (i.e., excitons). Rather, these transport processes exist as a gradient, where the contributions from each depend on the coupling strength and the temperature (and other forms of disorder). It is possible even for the same system that at high temperatures homo-FRET dominates, whereas at low temperatures, excitons dominate.[20,31,32] The effects of disorder are discussed in greater detail as follows.

As mentioned above, temperature and disorder in CPs and CPNs also affect the rate of exciton transport. At high temperatures (e.g. room temperature) excitons can resonantly couple to optical phonons (exciton-phonon coupling), which breaks up exciton coherence, forcing exciton transport to occur via incoherent, phonon-assisted processes. At low temperatures, exciton transport is dominated by coherent energy transfer.[32-35]

Conformational variability, variability in interchain interactions associated with more or less amorphous packing, and/or chemical defects in the CP chain give rise to energetic disorder that can affect various excited state processes as well as lead to shifts in emission spectra. Conformational variability (structural defects, i.e. bends or kinks in the polymer chain) arise most commonly in aggregated CP samples such as nanoparticles or thin films, whereas chemical defects in CPs are often the result of oxidation of the polymer (e.g. fluorenone/keto defects in polyfluorenes) or side products in the polymerization reaction.[36] The presence of various defects result in conjugation breaks along CP chains, which in turn yields inhomogeneous broadening of optical spectra due to the distribution of chromophore energies associated with a random distribution of conjugation lengths within the polymer.[37] Exciton energies can vary due to the underlying energetic disorder of the chromophores (i.e., variation in the site energies), variability in the transition dipole coupling strength (which is in turn highly dependent on interchromophore separation and orientation), and exciton energies vary depending on their spatial extent and symmetry. The various types and effects of disorder contribute to variability in exciton transport pathways and rates, thus broadening the distribution of fluorescence lifetimes within CPs and CPNs, leading to complex fluorescence intensity decay kinetics.

Exciton transport is not limited to singlet excited states. Singlet excitons may undergo intersystem crossing to form triplet excitons, which are typically much longer lived (ns-ms) compared to singlet excitons (fs-ns), and can have higher non-radiative decay rates (as in PPV-based polymers) than radiative (phosphorescence) decay rates.[38,39]

As such, triplet excitons in conjugated polymers are sometimes termed "dark excitons" (but should not be confused with the dark excitonic states resulting from a net zero transition dipole moment in the previous dimer model discussion).[40] Like singlet excitons, triplet excitons are capable of both coherent and incoherent transfer pathways (though Davydov splitting effects and coherent transport are minimal for most triplet systems, except for systems with heavy ions due to increased singlet-triplet mixing).[41] However, incoherent triplet exciton transport is restricted to nearest-neighbor mechanisms such as Dexter electron transfer (c.f. Section 1.3). As such, triplet exciton diffusion constants are typically much less than singlet exciton diffusion constants (typically by ~1-3 orders of magnitude).[8,42] On the other hand, triplet diffusion lengths can be quite large, due to the higher triplet lifetime as compared to singlets.[43]

1.2.1 Exciton Decay Processes in CPs

In addition to the exciton diffusion processes mentioned above, there are various decay processes in CPs and CPNs that determine the fate of a given exciton after photon absorption (c.f. Fig 1.1).

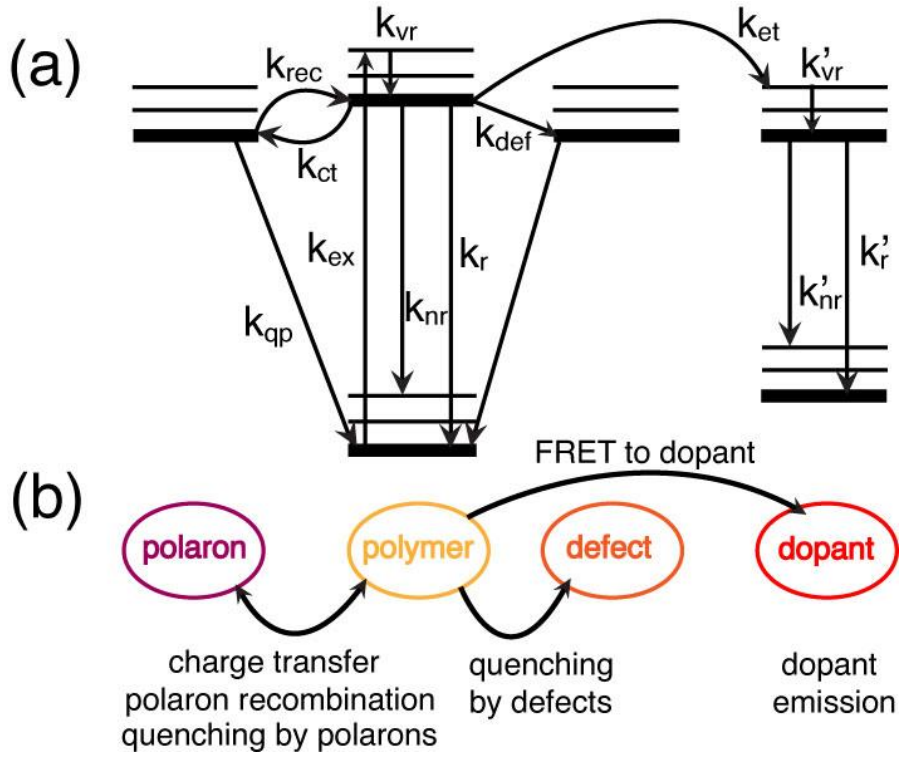

Fig. 1.1. (a) Jablonski diagram illustrating the exciton decay processes in doped CPNs. (b) Illustration relating the rate processes in (a) to their respective physical observables.

After vibrational relaxation to the ground vibrational state of the excited electronic state (k_{vr}), an exciton may either decay radiatively (k_r), or non-radiatively via internal conversion (k_{nr}). The exciton may also undergo Förster resonance energy transfer (FRET) to a defect site (k_{def}) where the exciton is quenched. Excitons may undergo charge transfer to form hole polarons (k_{ct}, discussed later), or the hole and electron recombine to reform the neutral exciton (k_{rec}). If subsequent excitons are generated in the vicinity of a polaron, they may be quenched by the polaron (k_{qp}). If a dopant species is introduced into the system, an exciton may undergo FRET to the dopant (k_{et}, discussed below), where similar processes apply if the dopant is a conjugated polymer, or radiative and non-radiative decay may occur if a fluorescent dye dopant is used.

1.3 Förster Resonance Energy Transfer (FRET) and Dexter Energy Transfer

Conjugated polymers exhibit two main mechanisms of incoherent energy transport, Förster resonance energy transfer (FRET) (which was discovered in the 1940s by Förster,[44] and is a useful tool for measuring interactions between molecules for distances <10 nm. As such, FRET is often referred to as a "molecular ruler."[45-47]) and Dexter energy transfer (discovered several years later in the 1950s by Dexter,[48] which occurs at short ranges, and when the conditions for FRET are unfavorable). The key differences between each process are discussed in detail below.

The process of FRET involves long-range transition dipole coupled energy transfer from an energy donor to an energy acceptor, resulting in non-radiative relaxation of the donor electron from the excited state back to the ground state, and concomitant

HOMO→LUMO excitation in the acceptor.[44] If transfer occurs between like molecules (e.g. equivalent chromophores of a conjugated polymer), this is referred to as homotransfer or homo-FRET. If transfer occurs between chemically distinct molecules, this is referred to as heterotransfer/hetero-FRET. The FRET process is dependent upon several variables, including intermolecular separation, spectral overlap of the donor fluorescence spectrum with the acceptor absorption spectrum, and relative alignment of transition dipole moments between the donor and acceptor. It is convenient to define a distance R_0 known as the Förster radius, where FRET between the donor and acceptor is 50% efficient (typically 1-6 nm).[49,50] Förster posited that, under favorable conditions, the transition dipoles of nearby chromophores can couple in such a way as to lead to energy transfer. Due to the dipole-dipole nature of the interaction, the rate of ET is given by

$$k_{et} = \tau_0^{-1}\left(\frac{R_0}{R}\right)^6, \tag{1.14}$$

where R is the intermolecular separation and τ_0 is the fluorescence lifetime of the donor. R_0 depends on the spectroscopic properties of the donor and acceptor, including the spectroscopic overlap. If the spectra are given as a function of wavelength in nm, then R_0 is given by

$$R_0 = \left(\frac{9000\ln(10)\kappa^2\Phi_D}{128\pi^5 N n^4} J(\lambda)\right)^{1/6}, \tag{1.15}$$

where n is the refractive index of the solvent, N is Avogadro's number, Φ_D is the fluorescence quantum yield of the donor (a measure of the percentage of photon absorption events that result in fluorescence photons). κ^2 is the transition dipole

orientation factor (typically assumed to be 2/3 for random transition dipole orientations), given by

$$\kappa^2 = (\cos\alpha - 3\cos\beta\cos\gamma)^2, \tag{1.16}$$

where the angle α corresponds to the angle between the donor and acceptor transition dipole vectors, β corresponds to the angle between the donor transition dipole vector and the intermolecular axis, and γ corresponds to the angle between the acceptor transition dipole vector and the intermolecular axis (c.f. Fig 1.2).

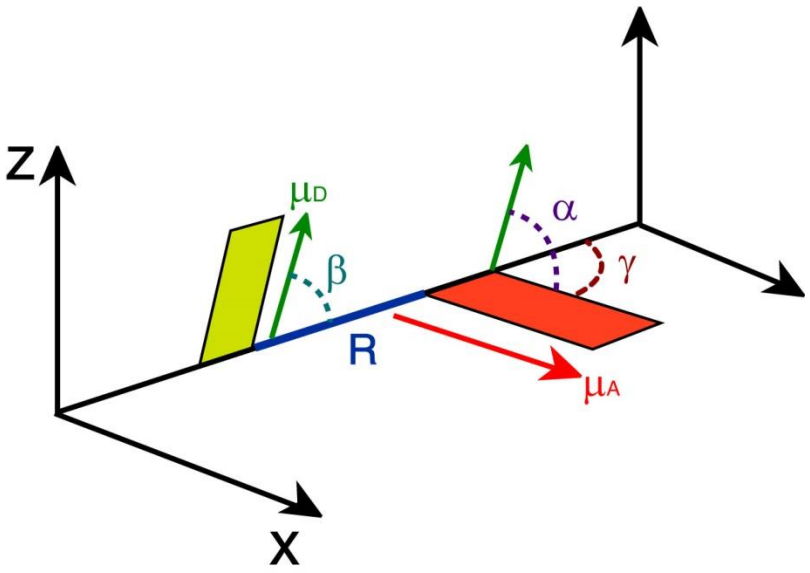

Fig. 1.2. Illustration of transition dipole vectors and angles used to calculate κ^2 for a donor and acceptor pair. μ_D (green) and μ_A (red) correspond to the donor and acceptor transition dipole vectors, R (blue) is the intermolecular distance along the intermolecular axis.

Lastly, $J(\lambda)$ is the spectral overlap integral, calculated by

$$J(\lambda) = \int_0^\infty F_D(\lambda)\varepsilon_A(\lambda)\lambda^4 d\lambda\,, \tag{1.17}$$

where λ and $d\lambda$ are the wavelength and wavelength spacing, respectively, $F_D(\lambda)$ is the normalized emission spectrum of the donor, and $\varepsilon_A(\lambda)$ is the extinction spectrum of the acceptor (converted from the absorption spectrum using Beer's Law).

The dependence of the FRET rate constant on the inverse sixth power of intermolecular separation arises initially from the fact that FRET is facilitated by interacting excited-state transition dipoles, whose coupling strength is proportional to the interchromophore separation R as R^{-3}, which is taken to be a first-order perturbation between the excited donor and acceptor. Using a Fermi Golden Rule approach, we see that the time-dependent probability of energy transfer derived from the dimer model can be reduced from its $\sin^2$ relationship with time to a linear relationship with time

$$P_{et}(t) = 2\pi\hbar t|V_{dd}|^2\rho(E_{res}), \tag{1.18}$$

where $\hbar$ is the reduced Planck constant and $\rho(E_{res})$ is the density of resonant states, proportional to the spectral overlap $J(\lambda)$ (Note that the time derivative of Equation 1.18 is Fermi's Golden Rule). Thus the interaction potential is squared, yielding an R^{-6} proportionality in the energy transfer rate.[23,51] The distinction between Förster transfer and coherent transfer is that Förster transfer is assumed for weakly coupled transition dipoles (and/or higher disorder), whereas coherent transfer requires strong coupling. As is seen in the analogous two-state perturbation model (Eqs. 1.4–1.7), the degree of mixing in the perturbed states (i.e., the strength of coupling between sites) depends on the

strength of the dipole-dipole coupling (V_{dd}) as compared to the level of thermal disorder k_bT, where k_b is the Boltzmann constant and *T* is temperature.

1.3.1 Dexter Energy Transfer

In organic semiconductors, another significant mechanism of energy transfer is Dexter electron transfer. In Dexter transfer, an electron in the ground state of the acceptor is exchanged with an electron in the excited state of the donor. These electrons possess identical spins, and remain in similar electronic states (e.g., an excited state donor electron is transferred to the excited electronic state of the acceptor, and a ground state electron in the acceptor is transferred to the ground state of the donor). The spin criterion holds true for singlet Dexter transfer, but not for triplet transfer, or triplet-triplet annihilation,[52] in which the transferred electrons possess opposite spins. The Dexter process is facilitated by molecular orbital (wavefunction) overlap, as well as spectral overlap of the donor fluorescence spectrum with the acceptor absorption spectrum. Given the former criterion, the Dexter transfer mechanism is very sensitive to changes in intermolecular separation. The distance-sensitivity of Dexter transfer is made clear upon inspection of the probability of electron exchange, given by:

$$p_{exchange} \approx \frac{2\pi}{\hbar} Z^2 J(\lambda) \exp(-2R/L), \tag{1.19}$$

where *Z* is a constant ($\ll 1$), $J(\lambda)$ is the is the normalized spectral overlap integral given by Equation 1.17, *R* is the intermolecular separation (in angstroms), and *L* is the average of the van der Waals radii of the donor and acceptor (in angstroms).[48] Inspection of the

exponential term alone in Equation 1.18 elucidates the distance sensitivity of Dexter transfer. Depending on the average van der Waals radius *L*, the probability of electron exchange falls to essentially zero within ~1-2 nm or less, and is reduced further depending on the spectral overlap and *Z*, proving that Dexter transfer is only efficient at very small intermolecular separations. However, for cases in which chromophores are tightly packed and Förster transfer is not favored (for example, due to unfavorable dipole alignment, or in the case of triplet excited states, which exhibit low acceptor extinction), Dexter transfer may be the dominant energy transfer mechanism.[53]

1.4 Conjugated Polymer Device Structure

Conjugated polymers have been utilized in several device types including photovoltaics and LEDs. Thin films are used in these devices in order to minimize device size and due to the need to layer active materials specifically for electron and hole injection and transport, or as an emissive material layer. In a typical organic photovoltaic (c.f. Fig 1.3), a substrate such as glass is deposited with several thin films, the first being an optically transparent conducting anode material that acts as a hole injection material (e.g. indium tin oxide, ITO). Due to the efficiency of energy transport and hole transport, hole-conducting CPs such as the ones used in this research would comprise the hole transport material in these devices. An efficient electron transport layer material (e.g. thiophene polymer, fullerene polymer) is blended with the hole transport material in the same solution, and then the blend is deposited on top of the cathode, forming a bulk heterojunction. A metal cathode (typically aluminum) is deposited on top of the bulk

heterojunction. In these devices, neutral photoexcitations known as Frenkel excitons (described in the next section) are generated in the bulk heterojunction where the hole and electron transport materials overlap, and the neutral exciton is separated into individual charges (electrons, holes) via charge transfer. The electron and hole are then transported through the respective transport layers to the cathode or anode, generating electrical current in the device. [54-56] Running a similar device in reverse produces light (as charges recombine and excitons decay radiatively), and is the basis of organic LED technology. The efficiency of these devices is determined partially by the work functions of the cathode and anode materials, as well as the efficiency of charge transfer and recombination. Typical power conversion efficiencies for these devices are up to ~9% for OPVs (similar to quantum dot based PVs), and up to 8% for OLEDs (compared to ~10% for quantum dot LEDs).[1,54,55,57-59]

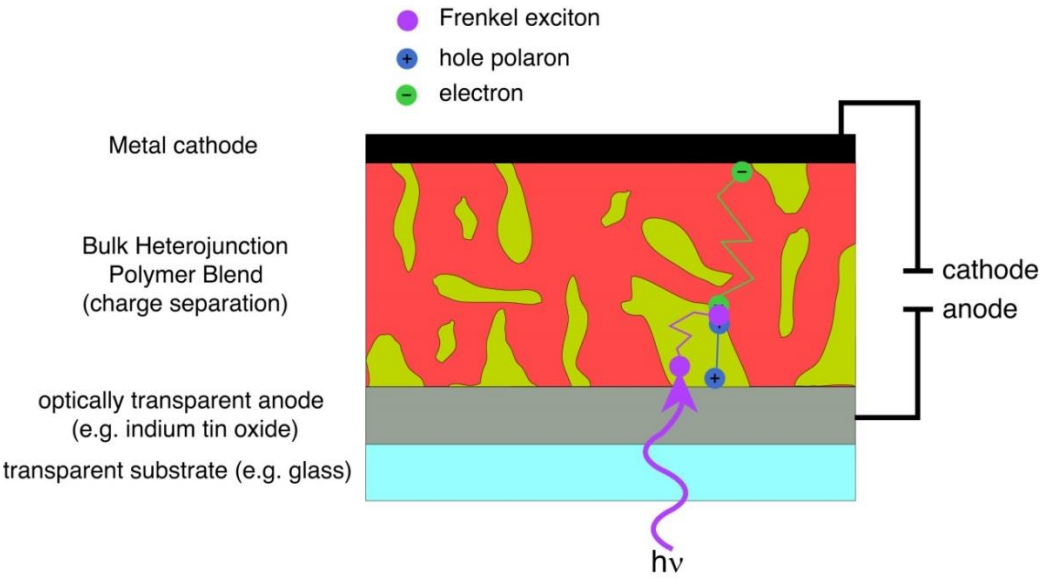

Fig. 1.3. Schematic of a bulk heterojunction organic photovoltaic/LED device depicting exciton generation and exciton, electron, and hole transport.

1.5 Polarons in Conjugated Polymers

In addition to mobile exciton states, organic semiconductors intrinsically possess mobile charged states that act as charge carrier states, which have been exploited for photovoltaic/LED device applications. In these devices, charges are either injected into the polymer through cathode/anode materials, or formed by dissociation of excitons through charge transfer events in the bulk heterojunction (c.f. section 1.4). Additionally, many fluorescence measurements on conjugated polymers and nanoparticles are complicated by photoejection of charges at higher excitation powers, resulting in a leftover isolated charge on the polymer chain that quenches the excited state via charge-transfer complex formation or damages the polymer resulting in photobleaching. These molecular ions along with the polarized volume surrounding them within the polymer are treated as quasiparticles and referred to as polarons.

The majority of measurements performed in this research were performed in air, and thus the presence of oxygen provides an oxidizing environment. This is combined with the fact that under ambient conditions, the CPs used in this study are inherently hole-conducting/electron donating. As such, hole polarons are assumed to be the prominent type of polaron occurring in these CPs. However, under reducing conditions, or by using intrinsically electron-conducting conjugated polymers based on perylene diimide structures, or based on fullerenes such as PCBM, electron polarons can be more prominent.[60-62] Hole polarons can recombine with electrons to reform Frenkel excitons, and the combined processes of exciton dissociation and charge recombination (together with luminescence quenching by polarons) lead to blinking phenomena in CP single

molecules and CPNs. [63-65] Polaron formation introduces red-shifted features into CP absorption spectra that overlap with the emission spectra.[66] Thus, the spectral overlap of hole polaron absorption with CP emission yields efficient FRET to polarons, substantially quenching fluorescence (and causing blinking when polarons are generated and recombine rapidly). In early device work, the observation of substantial quenching of CP film emission under only modest bias voltages (corresponding to relatively low fields of ~1 MV/cm or less) led to the conclusion that excitons in CPs have relatively low binding energies (<0.01 eV), similar to those of Wannier excitons,[67,68] which are typically only stable at low (a few K) temperatures.[30] However, later work by Bässler and others indicated that Frenkel excitons have much higher binding energies (~0.1-0.5 eV), and that emission quenching was due to high densities of hole polarons in the device acting as efficient fluorescence quenchers.[69,70] Indeed, polarons are able to quench ~90% of the fluorescence of a CP chain consisting of ~10^3 chromophores, and they can possess quenching volumes as high as ~400 nm^3, making them extremely efficient fluorescence quenchers.[64,70,71] Polaron quenching becomes significant at a density of $5x10^{17}$ polarons/cm^3, which is typically exceeded in devices.[7,72] In addition, polarons can diffuse throughout the conjugated polymer medium, given that conjugated polymers are disordered semiconductors. The localized quenching behavior of hole polarons has also been exploited for tracking of charge carrier motion in CPNs, [64,73] and can be utilized to determine the rates of polaron generation and recombination in CPNs via determination of blinking rates using single molecule fluorescence microscopy.

1.6 Aggregate Species in Conjugated Polymer Nanoparticles

Conjugated polymer nanoparticles are comprised of one or more collapsed CP chains. Given the dramatic increase in chromophore density, energetically favorable interactions between many closely spaced chromophores lead to the formation of aggregate species. These aggregate species can be in the form of H- or J- aggregates (which are two of the principal general types of exciton states discussed earlier in Section 1.2), excimers, or exciplexes.[74-76] These interacting species are given in detail below. In addition to the aforementioned aggregate species, conformational variability introduced upon chain collapse (e.g. bending/kinking of the polymer backbone) breaks up the conjugation along the polymer backbone. All of the aforementioned interactions yield changes in the emission characteristics of CPNs compared to polymer in good solvent (i.e., shifting and inhomogeneous broadening of the nanoparticle absorption and emission spectra, as well as increased lifetime heterogeneity), where aggregates and their corresponding photophysics contribute in greater proportion overall than conformational variability to the changes in CP photophysics upon nanoparticle formation.

The differentiating characteristics between H- and J-aggregates are their structural alignments, spectral shifts (that arise from the orientation of coupled transition dipoles), and fluorescence lifetimes. As previously mentioned, H- and J-aggregates both arise from Davydov splitting effects resulting from favorably arranged transition dipoles between interacting chromophores (the Frenkel exciton picture described in Section 1.2). While transition dipole orientation-dependence is implicit in the Frenkel picture, modern studies on H- and J-aggregates often prefer to discuss orientation dependence directly through

the structural alignment of the interacting molecules, known as the "slippage angle." This is the angle formed by the long axis of one molecule, and the line connecting the centers of the molecules. For high slippage aggregates (angles < 54.7°), the transition dipoles are aligned in a head-to-tail orientation, which leads to J-aggregate spectral characteristics. For low slippage aggregates (angles > 54.7°), the transition dipoles are in parallel orientation, leading to H-aggregate spectral characteristics (c.f. Fig 1.4).[77] In H-aggregates, the absorption and fluorescence spectra are shifted toward higher energy (hypsochromically shifted or blue-shifted) and the emission spectrum is broadened. The lifetimes of H-aggregates are also either similar to or longer than that of the monomer.[78-80] In contrast, J-aggregates exhibit bathochromically shifted (shifted toward lower energy or red-shifted) absorption and emission, with a narrowing of the emission band, an increase in fluorescence quantum yield, and a substantial reduction in lifetime compared to the monomer. (While Scheibe and Jelley both independently discovered J-aggregates in the same year, Jelley is formally credited for their discovery through their nomenclature, and Frenkel developed the quantum mechanical description).[19,75,77,81,82] The energy shifting in H- and J-aggregates results from exciton formation between the aggregated chromophores resulting in Davydov splitting into a higher and lower energy state relative to the degenerate monomers. Calculating the transition dipole moment for the higher and lower energy states in each case determines the optically allowed transitions for both aggregate species (c.f. Section 1.2), with the allowed transition for each case being the transition to the higher energy state for an H-aggregate, and the lower energy state for a J-aggregate. These states correspond a nonzero vector sum of transition

dipoles (parallel transition dipole arrangement for H-aggregates, head-to-tail arrangement for J-aggregates), whereas the opposite states yield transition dipole vector sums of zero (antiparallel transition dipole arrangement for H-aggregates, head-to-head transition dipole arrangement for J-aggregates), forming dark exciton states.[20,83]

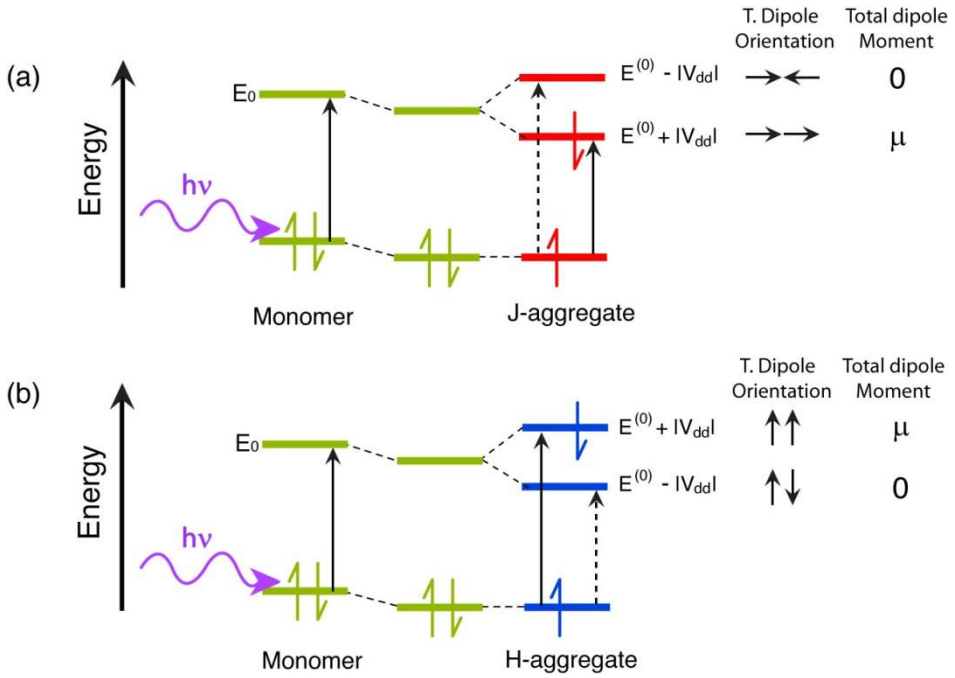

Fig 1.4. Molecular orbital illustration of ideal (a) J-aggregate and (b) H-aggregate states. Transition dipole coupling stabilizes the dimer. The allowed transitions for each aggregate are given by the solid black arrow, and forbidden transitions are given by a dashed black arrow. Transition dipole orientations and total dipole moments are given to the right of each M.O. diagram.

Excimers (excited dimers) and exciplexes (excited complexes) are another pair of aggregate species in CPs, and both result from an interaction of one molecule in its excited state with another molecule in its ground state. Excimers result from RET and/or electron transfer interactions (due to orbital overlap) between like molecules to form an electronically neutral dimer (similar to H- and J-aggregates, except that there is a net, though possibly slight, bonding interaction due to orbital overlap, and the ground state is dissociated, which gives rise to a characteristic broad, red-shifted spectrum). The main factors that impact whether excimers or H- or J-aggregates form includes the structural arrangement of the molecules, the relative transition dipole coupling strength between the interacting monomers, and whether there is a net bonding interaction in the excited state, (i.e., intermolecular bonding via a pi* orbital). Excimers and H-aggregates form under similar structural arrangements; however, excimers have several differentiating characteristics from H-aggregates. Unlike H-aggregates, constituent monomers of an excimer are only electronically coupled in the excited state, possessing a weak bonding interaction in the excited state, and a dissociative ground state (the individual molecules of the dimer repel following emission). In addition to the dissociative ground state, the other distinguishing photophysical features of excimers include a broad, red-shifted emission spectrum (due to the electronic stabilization of the dimer upon formation) lacking vibronic structure, and a substantial reduction in fluorescence lifetime.[83] Exciplexes are formed by electron transfer between two chemically distinct molecules (e.g. following charge transfer in a bulk heterojunction), where the excited electron donor becomes positively charged, and the electron acceptor becomes negatively charged.

Formation of the charge-transfer state results in either back-transfer to reform either the ground state or the Frenkel exciton on the donor, or coulombic attraction between the electron/hole pair to form the exciplex. Like excimers, exciplexes have a dissociative ground state following emission, and exhibit broad, structureless, red-shifted emission due to energetic stabilization of the charge-transfer complex. However, in contrast to excimers, exciplexes have longer lifetimes, where the exciplex state is either similar in lifetime or much longer-lived compared to the lifetime of the donor molecule, as well as a reduced fluorescence quantum yield.[76,83,84] Due to the conditions required for efficient electron transfer (c.f. section 1.4), exciplexes form most efficiently for arrangements of donor and acceptor that maximize molecular orbital overlap (c.f. Fig 1.5). Exciplexes also tend to be favored in nonpolar solvents, as polar solvents stabilize the interacting charges leading to solvent-separated ion pairing and exciplex quenching.[85]

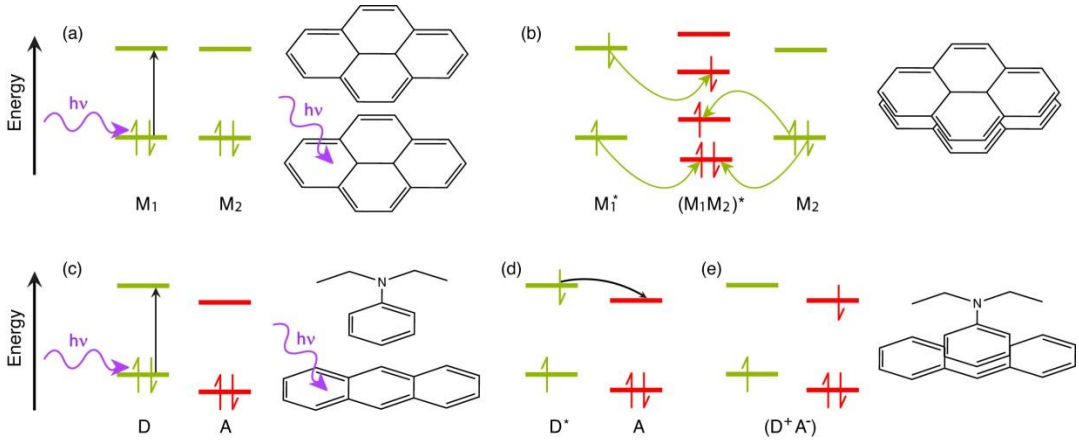

Fig. 1.5. Molecular orbital illustration of excimer (a, b) and exciplex (c-e) formation, accompanied by molecular illustrations of pyrene excimer formation (top) and anthracene/N,N-diethylaniline exciplex formation (bottom). In the excimer case, two like molecules M_1 and M_2 interact, with (a) M_1 initially excited to M_1*, followed by (b) RET (yellow arrows) to form a neutral excited dimer (M_1M_2)* (though RET may be replaced by electron transfer). In the exciplex case, two distinct molecules, one electron donor D and one electron acceptor A interact. (c) The donor is excited from D to D*, followed by (d) electron transfer (black arrow) from D* to the acceptor A to form an excited state charge-transfer complex (D^+A^-).[83]

1.7 Measurement of Exciton Diffusion Length

For some device types, it is required for excitons to travel long distances over the course of their excited state lifetime for optimum device efficiency (i.e., excitons must travel far enough to encounter a bulk heterojunction, so that charge transfer can occur, as in organic photovoltaics). In the experiments detailed in the later chapters of this dissertation, we aim to determine the length scale in which exciton diffusion occurs in conjugated polymer nanoparticles. Given the difficulty in determining the exciton diffusion constant directly, the quantity typically reported instead is the exciton diffusion length, L_D. The relationship between L_D and the diffusion constant D is derived from Brownian motion theory, which assumes that diffusion is given by Gaussian probability distribution function, given in 1D by

$$p(x) = \frac{1}{\sigma\sqrt{2\pi}} \exp\left(-(x - x_0)/2\sigma^2\right), \tag{1.20}$$

where x_0 is the initial position of a particle at time t_0, x is the positon at a later time t, and

$$\sigma = \sqrt{2Dt}\,, \tag{1.21}$$

where D is the diffusion constant. Extending Equation 1.21 to the exciton diffusion picture, and accounting for the probabilities of radiative decay and energy transfer over the course of the excited state lifetime, the diffusion length is given by

$$L_D = \sqrt{2nD\tau}\,, \tag{1.22}$$

where n is the dimensionality (n = 1, 2, 3), and τ is the exciton lifetime.

While Wannier excitons in crystalline inorganic semiconductors can possess diffusion lengths of several microns,[86] (Frenkel/molecular) exciton diffusion lengths in

organic semiconductors are typically much shorter. For example, measured exciton diffusion lengths for single crystals of anthracene range from ~30 nm to 60 nm,[87-89] and diffusion lengths of under 15 nm are typically reported for conjugated polymers.[13,90,91] The probability of energy transfer to polarons, chemical defects, and aggregate species (resulting from chromophore interactions) can reduce the observed exciton diffusion length. There are various experimental methods employed to characterize exciton diffusion in organic semiconductors that lead to a wide range of reported exciton diffusion lengths due to various experimental complications.[92] Many of the reported exciton diffusion lengths have been determined via various thin film methods, such as doped thin films, or photoluminescence quenching in bilayer device structures (where the donor/exciton transport layer and acceptor/quencher layer exist as adjacent thin film layers). [8,93,94] However, these methods are complicated by several factors, including pinholes in the film (that lead to direct excitation of the acceptor layer), quenching by surface plasmons from the metal contacts, interdiffusion of the quencher layer into the donor layer (i.e. poor layer segregation), waveguiding effects, and that the optical penetration depth (given by the inverse of the absorption coefficient of the material at the respective wavelength) is often significantly larger than the diffusion length of the material. It is also possible to image exciton diffusion with methods such as near-field scanning optical microscopy (NSOM),[3] but diffraction becomes an issue in that it places a lower limit on the measureable diffusion length (~50 nm). The experiments in this dissertation determine the exciton diffusion length indirectly with time-resolved

fluorescence spectroscopy, in conjunction with a model based on a Monte Carlo approach with a random-walk algorithm (given in detail in later chapters).

Exciton diffusion in CPNs involves both diffusion-like transport processes and decay to quenchers (e.g. defects, dopants). The simplest version of this physical picture involves modeling a series of excitons undergoing random walk trajectories in the presence of a single point-like quencher. The analytical solution for diffusion and decay from a point source (or to a point sink) is proportional to the zero-order Modified Bessel Function of Second Kind (K_0, which is a function of distance divided by L_D). At steady-state, diffusion and decay from a point source/sink is given in 3D by

$$n(R) = \frac{n_0 K_0(R/L_D)}{R}, \tag{1.23}$$

in 2D by

$$n(R) = \frac{n_0 K_0(R/L_D)}{\sqrt{R}}, \tag{1.24}$$

and 1D by

$$n(x) = n_0 K_0(x/L_D), \tag{1.25}$$

where n is the density of excitons that have decayed at distance R (or x in 1D) from the point source, n_0 is the initial density of excitons at the source, and L_D is the exciton diffusion length. Our exciton diffusion energy transfer model is tested using decay to a point sink (assuming L_D = 3 nm, and a single quencher of Förster radius of 0.1 nm for the sink). The results for 3D exciton diffusion and decay from our model (with comparison to Equation 1.23) indicate that the model reproduces diffusion and decay accurately (c.f. Fig. 1.6).

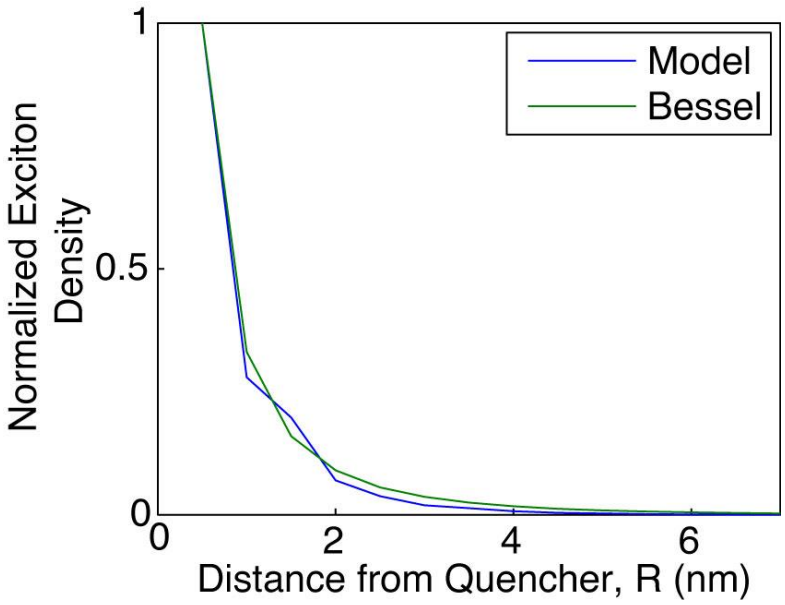

Fig. 1.6. Density of decayed excitons as a function of distance from a point-like source from the exciton diffusion energy transfer model (blue), with comparison to Equation 1.23 (green).

1.8 Fluorescence Anisotropy Decay in Conjugated Polymer Nanoparticles

Exciton transport in conjugated polymers and nanoparticles is the result of multiple energy transfer events between (essentially) equivalent chromophores. In these systems, energy transfer is more or less indistinguishable from one event to the next, and while steady-state UV-Vis and fluorescence can help to elucidate significantly different species in the ensemble via their spectral signatures (e.g. H-/J-aggregates, chemical defects), and decay rates can be probed by measuring fluorescence lifetimes for each distinguishable part of the ensemble, it is not possible to determine average energy transfer rates between equivalent chromophores using these methods. By examining changes in the polarization of the time-resolved fluorescence signal, it is possible to probe the rate of energy homotransfer (in the absence of rotational diffusion), and reveal underlying relationships between exciton transport rates and corresponding physical observables (e.g., differences in quenching between CPNs and CPs in solution, differences in fluorescence quantum yield and lifetime for similar polymers, etc.).

Fluorescence anisotropy is a measure of the average polarization of fluorophore emission upon excitation with plane-polarized light. Typically, the excitation source is linearly polarized, and the emission is analyzed after being passed through a linear polarizer oriented parallel (0°) or perpendicular (90°) relative to the excitation source. These components of the emission are given by I_0 and I_{90}, respectively, and the anisotropy *r* is then calculated by

$$r = \frac{I_0 - I_{90}}{I_0 + 2I_{90}}, \tag{1.26}$$

which forms a ratio of the difference between the parallel and perpendicular emission components relative to the total intensity. Extending this into the time domain, Equation 1.26 becomes

$$r(t) = \frac{D(t)}{S(t)} = \frac{I_0(t) - I_{90}(t)}{I_0(t) + 2I_{90}(t)}, \tag{1.27}$$

where $r(t)$ is the fluorescence anisotropy decay (FAD), $D(t)$ is the difference in the parallel and perpendicular components of the emission (given by $I_0(t)$ and $I_{90}(t)$, respectively), and $S(t)$ is the total polarized fluorescence intensity, given as the sum of the parallel component of the emission, and the two perpendicular components of the emission. FAD allows us to quantify the rate at which different processes (e.g. rotation, multiple energy transfer) cause depolarization of the fluorescence signal. It is worth noting that the relative amplitude of $I_0 \propto \cos^2\theta$ and $I_{90} \propto \sin^2\theta$, where θ is the angle of the emission polarizer. When the emission polarizer is set to θ = 54.7° (magic angle, ~55°), this results in $\cos^2\theta$ = 0.333 and $\sin^2\theta = 0.667$, which corresponds to a twofold amplitude of the perpendicular component of the emission relative to the parallel component of the emission, or $I_{55} \propto I_0 + 2I_{90}$.[47] Thus, it is possible to measure the total intensity $S(t)$ by magic angle orientation of the emission polarizer, and the anisotropy decay is calculated by

$$r(t) = \frac{I_0(t) - I_{90}(t)}{3I_{55}(t)}. \tag{1.28}$$

Conformational variability in CPNs results in many closely-spaced chromophores in varied orientations in space. Thus, it follows that a linearly polarized excitation source (e.g. a pulsed laser) would preferentially excite certain chromophores (those with their transition dipole moments oriented similarly to the polarized excitation pulse). While FAD is typically used to measure rotational dynamics of small molecules in solution (or rotational dynamics in macromolecules such as proteins),[95,96] in an aqueous suspension of CPNs, particles are typically large enough that rotational diffusion at room temperature occurs on time scales several orders of magnitude slower than the lifetime of the nanoparticles (rotational correlation times are tens of ns to μs, depending on particle size, whereas CPN lifetimes are typically on the picosecond time scale). Thus, we assume that any depolarization of fluorescence can effectively be ascribed to energy homotransfer events. As previously discussed, exciton homo-transfer on the ps-ns time scale is typically driven by incoherent methods of energy transfer (e.g., FRET, Dexter transfer). Given that the interchromophore distance is minimal (~1 nm) and assuming sufficient spectral overlap, the efficiency of each energy transfer event is then essentially governed by the alignment of transition dipole moments, accounted for in the κ^2 term in equation 1.15, which need not be perfectly aligned for energy transfer to occur. Therefore, each energy transfer event depolarizes the resulting emission, as is illustrated in Fig. 1.7 (though, the extent to which any two chromophores that may be exchanging energy are orientationally-correlated is not known). The rate of depolarization, and thus the rate of exciton motion (given by the inverse of the measured correlation time τ_c) can be probed using picosecond fluorescence anisotropy decay. Using the assumption that the

correlation time τ_c is a measure of the time it takes for a single incoherent transfer event to occur in conjunction with the fluorescence lifetime τ, the average number of energy transfer events occurring within the fluorescence lifetime can be approximated by the ratio of the lifetime and correlation time. Taking the approximate number of incoherent transfer events with the exciton diffusion length L_D (determined from- numerical random walk simulations), the typical distance per energy transfer event can be determined (if ~3 transfer events occur within the fluorescence lifetime, with a 12 nm L_D, this gives ~4 nm distance traveled per energy transfer event).

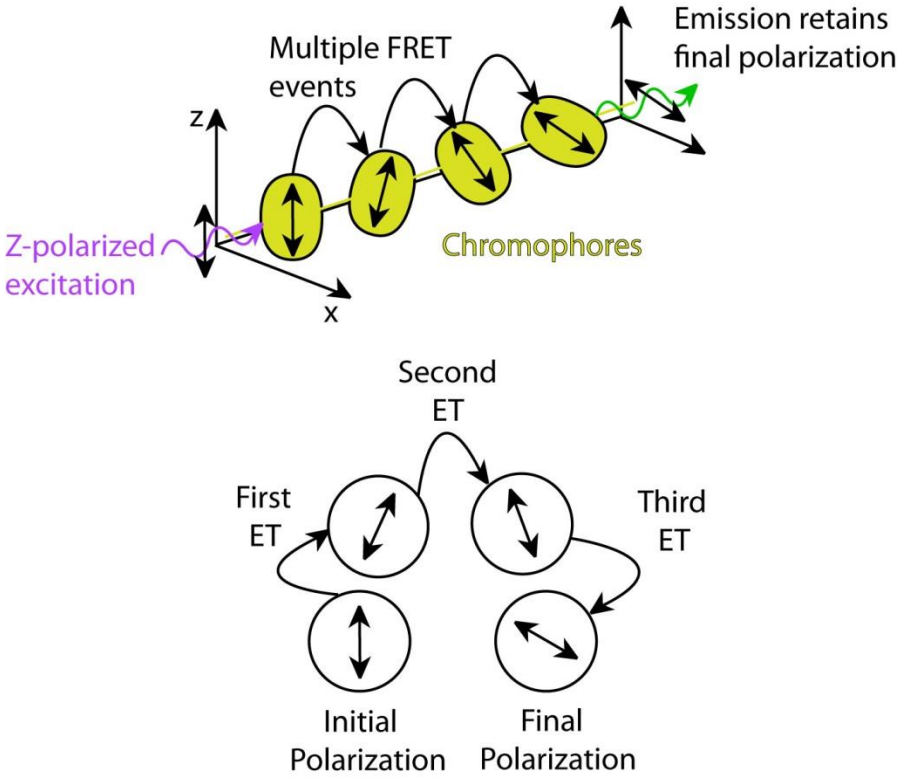

Fig. 1.7. (top) Diagram depicting polarization loss via multiple energy transfer. (bottom) Illustration of polarization changes after each FRET event.

The chapters within this dissertation principally focus on steady-state and time-resolved fluorescence spectroscopy of conjugated polymer nanoparticles and solutions with the goal of better understanding exciton transport in CPNs and related phenomena such as amplified energy transfer. Additionally, we examine the effects of nanoscale disorder on the excited state kinetics and spectra of CPNs. By understanding the various nanoscale interactions occurring in CPs and CPNs, we can better exploit factors such as particle size, swelling, or doping to tune the fluorescence properties of these materials (e.g., emission color, fluorescence lifetime, fluorescence quantum yield, energy transport rates, etc.) to improve upon fluorescent probes and organic semiconductor devices. We also estimate the length scales of exciton transport in addition to the rates of exciton transport between CPNs and linear CPs to elucidate the relationships between nanoscale interactions and physical observables (such as fluorescence quantum yield and fluorescence lifetimes) in these systems. In addition, we aim to improve the fluorescence characteristics of CPNs (e.g. brightness and red-shifting of emission) for fluorescence imaging applications. Chapter 2 describes the materials, experimental methods, spectroscopic techniques, and instruments utilized in this research. Chapter 3 details the use of dye doping and polymer blending in CPNs with the aim of improving fluorescence brightness and red-shifting emission for fluorescence imaging applications, as well as to estimate the exciton diffusion length while accounting for defects in CPNs. Chapter 4 delineates the use of solvent-induced swelling coupled with time-resolved fluorescence anisotropy decay measurements to determine the rate of exciton transport in undoped CPNs compared to the linear polymer, as well as to assess the reversibility of quenching

by defects via swelling. Both projects utilize a combination of steady-state and time-resolved spectroscopy in conjunction with Monte Carlo simulation to address these issues from multiple angles.

CHAPTER TWO

EXPERIMENTAL METHODS

2.1 Materials

The two principal fluorescent conjugated polymers used to prepare conjugated polymer nanoparticles (CPNs) in these studies were poly[(9,9-dioctylfluorenyl-2,7-diyl)-*co*-(1,4-benzo-{2,1',3}-thiadiazole)] (PFBT, MW 10,000, polydispersity 1.7), and poly[2-methoxy-5-(2'-ethyl-hexyloxy)-1,4-phenylene vinylene] (MEH-PPV, average MW 200,000, polydispersity 4.0), and were purchased from ADS Dyes, Inc. (Quebec, Canada). The fluorescent dye perylene red (Exalite 613) was purchased from Exciton (Dayton, OH). Polystyrene microspheres, and the fluorescent dye fluorescein were purchased from Life Technologies (Invitrogen, Grand Island, NY). The fluorescent dye Lucifer Yellow CH dipotassium salt (LY, 1 mg/mL in water), 3-aminopropyl-trimethoxysilane (APS, 97%), sodium hydroxide (SigmaUltra, minimum 98%), and solvents tetrahydrofuran (THF, anhydrous, inhibitor-free, 99.9%), and ethanol (200 proof, anhydrous, ≥99.5%) were purchased from Sigma-Aldrich (Milwaukee, WI). All materials were used without further purification.

2.2 Nanoparticle Preparation

The method used to prepare fluorescent conjugated polymer nanoparticles is based on a previously described nano-precipitation method,[97] adapted from Kurokawa and co-workers.[98] A stock solution of a given conjugated polymer was prepared at a

concentration of 1000 ppm (mg/kg) in THF. The polymers were sufficiently dissolved by gentle agitation of the solution at room temperature. For these experiments, the precursor solution to the nanoparticle suspension was prepared by diluting an aliquot of stock solution to a concentration of 20 ppm. For doped samples, dopant fluorescent dyes or polymers were added into the solution in their respective amounts prior to the addition of the diluting solvent such that their concentration in the diluted precursor solution was 0.1%–10% by weight, relative to the polymer concentration (further details given in Chapter 3). The resulting solutions were agitated gently to ensure solution homogeneity. A 2 mL aliquot of precursor solution was then rapidly injected via micropipette into 8 mL of deionized water under bath sonication at a frequency of 40 kHz and room temperature for ~30 seconds.

Conjugated polymers respond in similar, yet different ways to changes in solvent environment depending on the rate of incorporation of polymer from a good solvent into a poor solvent. It is thermodynamically favorable for a hydrophobic, long-chained molecule like a conjugated polymer to aggregate with itself in water (a poor solvent). By first dissolving the polymer into a good solvent that is also water-miscible such as THF, it is possible to mix otherwise insoluble hydrophobic polymers (or other hydrophobic molecules such as small-molecule fluorescent dyes) into a poor, aqueous solvent. Adding the dissolved polymer into a poor solvent drop-wise results in substantially increased aggregation of the polymer. Indeed, slow mixing of a polymer solution into a poor solvent is a commonly utilized method of polymer purification.[99] This can be confirmed with our polymer samples, as vacuum filtration of a solution in which dissolved polymer

is added drop-wise to rapidly mixing water results in the loss of >80% the polymer during the subsequent filtration step as confirmed by UV-Vis. Alternatively, fast injection of the precursor THF solution into rapidly mixing water results in local polymer chain collapse as a result of hydrophobic interactions, polymer-water interfacial tension, and surface free energy effects.[100] Under these conditions, chain collapse occurs at a faster rate that does not allow for flocculation to occur before a given sample of polymer collapses and is moved from its local environment into the bulk solution. Thus, formation of nanoparticles (i.e. nanoscale aggregates comprised of few polymer chains) is the kinetically favored product of rapidly mixing a dissolved polymer into a poor solvent. After nanoparticle formation occurs, the collapsed chain conformation is retained as the remaining THF is removed, resulting in an aqueous colloidal suspension of conjugated polymer nanoparticles. The size of the nanoparticles can be adjusted by increasing or decreasing the concentration of the precursor solution (e.g. increasing the precursor concentration yields a concomitant increase in nanoparticle size).[101] Typical particle sizes range from 4-30 nm, which is verified by atomic force microscope (AFM) image analysis.[42,97,102]

The process by which THF was removed from the samples has been refined from our previous partial vacuum evaporation procedure. THF was removed by placing the nanoparticle samples in a vacuum oven at room temperature under nitrogen flow for 8-10 hours in order to remove enough THF to prevent bumping during the subsequent partial vacuum evaporation step. Nitrogen flow was ceased and samples were evaporated under vacuum for 6-7 hours at a temperature of ~40 °C to remove most of the remaining THF.

The total volume of liquid was reduced by ~60% during the evaporation process, which was confirmed to be sufficient by an iterated Raoult's Law calculation, the results of which yield that <1% THF exists at ~40% volume loss. No residual THF odor was detected in the samples. Additionally, further evaporation yielded no further change in the fluorescence spectrum or quantum yield. The samples were subsequently vacuum filtered through a glass fiber prefilter and a 0.1 μm PVDF membrane filter in order to remove larger aggregates. The resulting suspensions are clear (not turbid) and stable, showing no signs of aggregation for months.

2.3 Characterization Methods

Several techniques are employed in order to characterize our nanoparticle samples. These include atomic force microscopy (AFM), UV-Vis spectroscopy, steady-state fluorescence spectroscopy, and fluorescence quantum yield measurement.

2.3.1 Atomic Force Microscopy (AFM)

AFM is a subtype of scanning probe microscopy, in which the surface topography of a sample is analyzed using a sharp probe tip affixed to a reflective cantilever spring. In all modes of AFM imaging, the tip is raster-scanned across a sample that is either immobilized or patterned onto a substrate. A laser is reflected off of the back of the cantilever and onto a detector (e.g. a quadrant photodiode). The laser signal is then monitored in order to track changes in the cantilever as the tip interacts with the sample. The typical properties that are tracked are either cantilever deflection, or the amplitude or

frequency of near-resonant cantilever vibrations, depending on the mode of operation, discussed in detail below. The image is produced line-by-line by translating the changes in probe height into a topographic image of the sample.[103-105]

Depending on the properties of sample to be studied, different operating modes may be chosen. The simplest mode of AFM operation is contact mode (sometimes referred to as static AFM).[105] In contact mode, the sample is brought into direct contact with the tip, which is affixed to a cantilever with a low spring constant (0.1-5 N/m, typ.), causing deflection of the cantilever. As the tip is scanned across a sample, the cantilever deflection (and thus the force on the tip) is kept constant by raising or lowering the tip in response to changes in surface topography. Contact mode is best suited for harder samples, where the interatomic spring constants (~10 N/m) are greater than the spring constant of the cantilever material, thus preventing deformation of the sample by the AFM. Typical contact mode (repulsive) forces range from ~0.01 nN (requires solvent submerged samples) or ~1-100 nN (in air).[104] An inherent difficulty with contact mode AFM imaging arises from capillary forces due to liquid layers adhered to the surface of a sample under ambient conditions. This leads to substantial attractive forces (~100 nN) on the probe that lead to the probe suddenly jumping into contact with the sample through the liquid layer, or "snapping-in," which can damage samples in some cases.[105]

Non-contact mode is one of two dynamic AFM modes designed to circumvent cantilever adhesion, as well as the difficulties related to soft samples. In this mode, a stiff cantilever (20-100 N/m) is vibrated at or close to the resonant frequency of the cantilever material (70-200 kHz,), and at constant amplitude (~30 nm) by a piezoelectric element on

the AFM tip mount. As the cantilever is brought closer to the sample, attractive, long-range forces on the order of pN (e.g. Van der Waals forces) dampen the oscillation of the cantilever and cause a slight shift in the phase of the cantilever oscillations, which shifts the effective resonance frequency (thus, this mode of AFM is sometimes referred to as frequency modulation AFM). The tip-sample distance that yields this dampening and frequency shift is held constant (~5-10 nm) as the probe is rastered across the sample. This method is non-destructive, since the tip never makes contact with the sample. However, non-contact mode is still prone to "snap-in" if the response time of the z-height electronics is slow, which can reduce scan speeds and cause artifacts in topographic images if tip adhesion occurs.[106]

Intermittent contact (tapping or AC) mode AFM is another dynamic AFM mode, which shares similar probe stiffness and oscillation frequency characteristics to non-contact AFM. The key differences of tapping mode AFM are as follows. Once the probe is moved close enough to the sample in order to make periodic contacts, the cantilever oscillations are dampened. The amount of oscillation dampening is maintained at a set-point value, which is related to the amount of tip-sample contact force (lower set-points correspond to greater vibration dampening, and hence, higher contact force). Thus, rather than controlling z-height by maintaining a resonance frequency shift, the vibration amplitude of the cantilever is monitored and the z-height is adjusted to maintain the dampened amplitude (as such, this mode is sometimes referred to as amplitude modulation AFM). Another key difference in tapping mode operation is that the cantilever is vibrated at a higher oscillation amplitude (~100 nm, typ.), which allows the

probe to overcome adhesion forces, electrostatic forces, and friction between the tip and sample.[107] In addition, tip-sample contact forces in tapping mode AFM can be as low as 0.1 nN in air, which is greatly reduced as compared to contact mode under ambient conditions, making this method preferable for soft samples that are easily deformed or damaged by contact mode operation, or for weakly bound samples that would be easily swept off of the substrate by lateral forces in contact mode.[107,108]

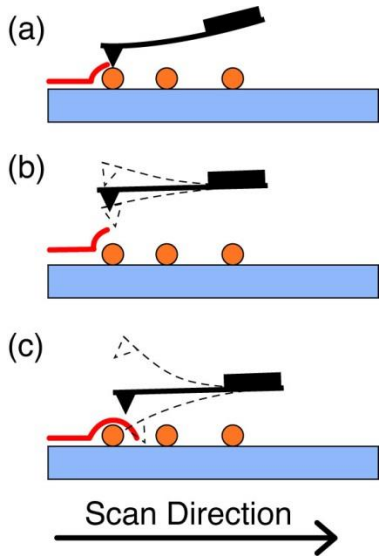

Fig. 2.1. Simplified illustration of a line scan using the various modes of AFM imaging, including (a) contact mode, (b) non-contact mode, and (c) intermittent contact mode.

Nanoparticle size distributions are determined with an Ambios Q250 multimode AFM in tapping mode. AFM samples were prepared by a dip-casting procedure. First, a cleaned, dry glass coverslip was amine-functionalized with 70 µL of freshly prepared 5×10^{-4} M APS in anhydrous ethanol. The solution was left on the coverslip for 3 minutes, followed by rinsing the coverslip with deionized water, and blowing it dry with nitrogen. An aliquot of the nanoparticle suspension was diluted by 30-40 times in a small beaker, and the coverslip was submerged into the diluted suspension with the functionalized side up for 40 minutes. The coverslip was then carefully removed from the solution and allowed to dry completely in a vacuum oven. To prepare the sample for AFM use, the coverslip was fixed to a glass slide with thin strips of tape. Particle sizes are determined by analyzing the peak z-heights of each viable particle in the image (i.e. ignoring aggregated particle clusters) and constructing a histogram to determine the mean and standard deviation of the particle sizes. Each scan was performed on a 2 µm by 2 µm scan region at a scan rate of 0.5 Hz (lines/s), with scan resolution of 500 lines per image.

There are several factors that impact the quality of an AFM image, including tip wear or breakage, as well as improper tuning of the PID (Proportional, Integral, and Differential) feedback loop. It is not possible to extract accurate particle size information from the diameters of the particles in the x-y plane due to tip convolution effects between the sample surface and the tip, which distort the image in the x-y plane (convolution is discussed in detail in section 2.4.2). The sharper the tip is, the smaller this effect is. As the tip wears and becomes blunted, this convolution effect is exacerbated, making the particles appear larger in the x-y plane. If foreign matter (e.g. dust, dirt) is stuck to the tip,

or the tip is broken as a result of crashing the tip into the sample substrate, this can yield false duplicate particles in the image (for every particle in the image). Improper setting of the PID feedback loop can result in cantilever hysteresis, in which the change in z-height needed to restore the cantilever oscillations to the set point value is overshot (or undershot) compared to the actual change required to restore the oscillations to the set point value. This translates into improper z-height values, and the potential to have the probe tip either scratch the sample or crash into the sample or substrate, damaging the probe tip.

Sample standards are utilized to validate lateral and vertical resolution of the AFM. The standards are either gratings with known height and spacing, or particles of known diameter. Lateral resolution is limited by the sharpness of the AFM tip since the observed image in AFM is the convolution of the tip with the sample. The probes used with our AFM (NSC16) have a tip width of 8 nm, as supplied by the manufacturer. Vertical resolution (often referred to as "Z noise") is determined by oscillating the cantilever with the x-y scanning electronics disabled and the tip engaged with a sample, then determining the standard deviation of the cantilever oscillations. The RMS noise of the AFM in the z-direction was measured using the aforementioned process, yielding a vertical resolution of 1.76 angstroms. Proper adjustment of the vibration isolation platform, and reduction of air currents and acoustic noise is required to maintain RMS noise below acceptable levels.

2.3.2 UV-Vis/Absorption and Fluorescence Spectroscopy

UV-Vis absorption spectra were collected on a Shimadzu UV2101PC scanning spectrophotometer using 1 cm quartz cuvettes. The absorption spectra were used to determine the nanoparticle concentration and peak absorption wavelength corresponding to the HOMO-LUMO electronic transition. For fluorescence measurements, concentrated nanoparticle samples (peak absorbance between 0.2–0.4) were diluted to yield a peak absorbance of ~0.1 for collection of fluorescence spectra or fluorescence lifetime measurement. Extinction coefficients for each polymer in THF were calculated by rearranging Beer's Law to give $\varepsilon = A/lc$, where ε is the extinction coefficient of the polymer at a given wavelength, A is the absorbance of the sample, l is the sample path length (typically 1 cm) and c is the molar concentration of polymer. To calculate the nanoparticle extinction coefficient, the number of polymer molecules per nanoparticle N_{np} is determined from the mean nanoparticle volume (determined from the mean radius from AFM measurements) and the polymer molecular weight, using the assumption that the polymer density is ~1 g/cm^3. This is then multiplied by the extinction coefficient for the polymer in THF yielding $\varepsilon_{np} = N_{np}\varepsilon$. Samples were diluted to an absorbance of ~0.05 for fluorescence quantum yield measurement. Steady-state fluorescence spectra were collected using a commercial fluorescence spectrometer (Quantamaster, Photon Technology International, Inc.) with 1 cm cuvettes. Samples were diluted to an absorbance of ~0.1 AU or less at the relevant excitation wavelengths. To avoid saturation of the photomultiplier tube (PMT) detector, all slit widths were kept at 0.50 mm. Multiplying the slit width by the reciprocal linear dispersion of the system (4 nm/mm for a 1200 grooves/mm grating) yields a wavelength resolution of 2 nm. The acquisition time

was set to 1 s/nm to overcome noise in the spectra evident at lower acquisition times. The signal-to-noise (SNR) ratio for this instrument under the aforementioned conditions was measured to be ~10,000:1 using methods described by the manufacturer.

It is important to ensure sufficient dilution of fluorescent samples in order to avoid the inner filter effect, in which a photon emitted by one molecule is reabsorbed or scattered by another molecule in close proximity. An important note about the inner filter effect is that it is not limited by sample concentration alone in CPNs. Particle size must also be considered in this case, since it is possible to prepare nanoparticles with diameters that exceed the optical penetration depth of the material. The optical penetration depth (or optical skin depth) of a material can be determined by $l_s = \alpha(\lambda)^{-1} = d/A(\lambda)$, where $\alpha(\lambda)$ is the absorption coefficient of the material at wavelength λ, $A(\lambda)$ is the absorbance at wavelength λ, and d is the thickness of the material. Optical penetration depths range from tens of nanometers to several microns, depending on the material. Typical values for conjugated polymers range from ~40 nm to ~400 nm.[109-111] Since CPNs are comprised of multiple closely-spaced chromophores, it is possible for a photon to be emitted from a chromophore on one end of a large particle, transmit through the particle, and be reabsorbed by another chromophore at the opposite end. This is one of the reasons why vacuum filtration is used to remove larger aggregates from the nanoparticle suspensions prior to measuring their fluorescence.

2.3.3 Fluorescence Quantum Yield

Fluorescence (or photoluminescence) quantum yield is a measure of the fraction of photon absorption events that result in emission of a fluorophore (expressed as a ratio between 0 and 1 or as a percentage). Fluorescence quantum yield measurement provides a quantitative comparison of the quantum efficiency of fluorescence between fluorophores. In terms of rates, the fluorescence quantum yield is given by $\Phi = k_r/(k_r + k_{nr})$. Where Φ is the fluorescence quantum yield, k_r is the radiative rate and k_{nr} is the non-radiative rate (k_{nr} encompasses all other processes that do not contribute to the fluorescence emission, e.g. non-radiative decay by internal conversion, energy transfer pathways, inter-system crossing to form triplet states, polaron formation, etc.).

The fluorescence (photoluminescence) quantum yield (QY or PLQY) of the CPN samples was determined in several steps. First, an appropriate standard fluorophore must be selected with an absorption and emission maximum similar to the conjugated polymers under study. In this work, the standard fluorophores used were fluorescein dissolved in 0.01 M sodium hydroxide (note: it is important to check the pH of the solution to ensure it is above 10 to ensure that only the fluorescein dianion exists in solution,[112] since NaOH and solutions thereof tend to absorb ambient CO_2), and Lucifer Yellow CH dissolved in water (LY). A common absorption wavelength was selected between the sample and standard (473 nm for fluorescein, 450 nm for LY), and solutions were prepared at an absorbance of ~0.05 AU at the common absorption wavelength. Emission spectra were collected at the common excitation wavelength, and the fluorescence quantum yield is calculated by the expression

$$\Phi_{F,x} = \frac{A_s}{A_x}\frac{I_x}{I_s}\left(\frac{n_x}{n_s}\right)^2 \Phi_{F,s}\,, \tag{2.1}$$

where, $\Phi_{F,s}$ is the fluorescence quantum yield of the standards (0.92 for fluorescein in 0.01 M NaOH and 0.21 for LY),[113,114] $\Phi_{F,x}$ is the fluorescence quantum yield of the sample, *A* is the absorbance, *I* is the integrated fluorescence intensity, and *n* is the refractive index of the solvent. It is important to note that a solvent blank must be measured for both absorbance and fluorescence measurements in order to properly apply baseline correction to the spectra when calculating the fluorescence quantum yield.

2.4 Time-Resolved Fluorescence Spectroscopy

Time-resolved fluorescence spectroscopy provides a window into many physical processes that are not readily apparent from steady-state fluorescence measurements alone. Measurement of the mean fluorescence lifetime of an ensemble of fluorophores gives the average amount of time that a given fluorophore spends in its excited electronic state following photon absorption, which can be used as a means to determine how various physical processes affect the excited state. The fluorescence lifetime is related to the rate of depopulation of the excited state (k_f) by $k_f = k_r + k_{nr} = \tau^{-1}$, where τ is the fluorescence lifetime. When both lifetime and fluorescence quantum yield are known, it is possible to separate out the radiative and non-radiative rates. For complex systems in which two or more species interact, lifetime measurement elucidates how intermolecular interactions (e.g. intermolecular collisions, FRET, charge transfer, etc.) affect the excited state of a fluorophore. For example, if fluorescence quenching is observed in the steady-

state measurements, lifetime measurements will indicate whether the observed quenching is static or dynamic, which provides insight into the physical processes that cause fluorescence quenching. Static quenching does not affect the fluorescence lifetime because this type of quenching is often the result of formation of a ground state non-fluorescent complex with another molecule. Photon absorption by the complex results in no emission events from the complexed fluorophores, thus reducing the fluorescence intensity of the ensemble, but not the lifetime, since the excited states of unbound fluorophores remain unchanged. Dynamic quenching typically reduces the lifetime of the quenched fluorophore, since dynamic quenching only occurs when the fluorophore is already in the excited state (e.g., quenching by molecular oxygen, FRET), thus reducing the mean lifetime of the quenched fluorophores by depopulating the longer-lived excited state. One means of describing fluorescence quenching is via the Stern-Volmer equation, given by:

$$F_0/F = 1 + K_{SV}[Q], \tag{2.2}$$

where F_0 is the initial fluorescence intensity in the absence of quenchers, F is the fluorescence intensity in the presence of quenchers, K_{SV} is the Stern-Volmer quenching constant, and $[Q]$ is the concentration of the quenching species. K_{SV} takes on different definitions, depending on the type of quenching in the system. The following derivation of Equation 2.2 is originally for a simple collisional quenching process; however, other quenching mechanisms such as FRET are observed to follow Stern-Volmer-type quenching. For dynamic quenching, K_{SV} is derived using the rate equations describing emission with and without quenching at steady state,

$$\frac{d[F]^*}{dt} = k_{abs} - \left(k_f + k_q[Q]\right)[F]^* = 0, \tag{2.3}$$

and

$$\frac{d[F]^*}{dt} = k_{abs} - k_f[F]_0^* = 0, \tag{2.4}$$

where the asterisk on $[F]$ is used to denote an excited fluorophore, and k_q is the quenching rate constant. Division of 2.3 by 2.4 yields

$$\frac{F_0}{F} = \frac{k_f + k_q[Q]}{k_f} = 1 + k_q\tau_0[Q] = 1 + K_{SV}[Q]. \tag{2.5}$$

Thus, for dynamic quenching, $F_0/F = \tau_0/\tau$, where τ_0 and τ correspond to the unquenched and quenched fluorescence lifetimes, respectively. For static quenching, K_{SV} is related to the concentrations of complexed fluorophore $[F-Q]$, non-complexed fluorophore $[F]$ (with initial concentration $[F]_0$) and quencher by

$$K_{SV} = \frac{[F-Q]}{[F][Q]} = \frac{[F]_0}{[F][Q]} - \frac{1}{[Q]}, \tag{2.6}$$

which is rearranged to give Eq. 2.2. If quenching is described by a combination of static and dynamic quenching, then plotting F_0/F vs. $[Q]$ will yield positive deviations from the linear Stern-Volmer relations given above. Instead, F_0/F vs. $[Q]$ is accurately described by multiplying the individual Stern-Volmer equations corresponding to static and dynamic quenching.[47] In addition, high energy transfer rates (large k_q) can result in positive deviations from Eq. 2.6 despite resulting solely from dynamic quenching (e.g., in blended CPNs that can have multiple quenchers doped within the nanoparticle at high doping levels), which requires alternative methods to describe quenching (e.g. Poisson statistical distribution of quenchers in CPNs, discussed in Chapter 3).[102]

2.4.1 Overview of Time-Resolved Fluorescence Instrumentation

There are various types of time-resolved fluorescence setups that vary in their complexity, cost, and effective time resolution. Lifetime methods with slower time resolution (e.g. using pulsed LEDs/lamps, with temporal width of a few ns, coupled with less sophisticated electronics) are less expensive and less complex than many setups with time resolution below 1 ns or faster, and are useful when the dynamics to be measured are slow (e.g. triplet dynamics, dynamics of conventional fluorescent dyes). The methods that afford the best time resolution of time-resolved fluorescence spectroscopy (sub-picosecond time resolution) typically utilize amplified ultrafast lasers at lower repetition rates (kHz repetition rates) as excitation sources (making these methods the most expensive). In the aforementioned systems, emission is detected via non-linear optical processes using intense laser pulses to create an optical gate (e.g., via Kerr gating, or by frequency mixing of the fundamental laser pulse with the sample emission in a non-linear crystal medium as in fluorescence upconversion),[115,116] or by monitoring changes in absorbance of a sample after excitation using a pump-probe type method (as in transient absorption spectroscopy).[117] The intensity decay is then constructed point-by-point by delaying the fundamental pulse by some known amount using an optical delay line (i.e., a pair of mirrored surfaces on a translation stage), and the changes in intensity of a given non-linear phenomenon (e.g. intensity of a sum-frequency signal vs. delay time) are measured to construct the decay trace. The time resolution of these setups is determined by the pulse width of the fundamental laser (typically a few hundred femtoseconds). In addition to measuring lifetimes of emissive states, methods such as transient absorption

are also useful for probing dark states that do not contribute to an emission signal, but possess transient spectroscopic signatures in the absorption spectrum (e.g. measuring the lifetimes of charge-transfer states).[118]

One of the more common methods of time-resolved fluorescence spectroscopy that balances cost, complexity, acquisition time and effective time resolution is Time-Correlated Single Photon Counting (TCSPC) spectroscopy. The mechanism of operation is described as follows. A pulsed light source is utilized as an excitation source. The temporal width of the excitation pulse depends on the source used and the dynamics to be measured (Pulsed LEDs or lasers such as N2 lasers have ns pulsewidths, dye lasers have pulsewidths down to a few ps, and ultrafast Ti:Sapphire lasers offer fs pulsewidths). The pulses are split, where one pulse is used to excite the sample, resulting in fluorescence photons that are incident on a single-photon counting detector (e.g. an avalanche photodiode or APD) and the other pulse travels to another fast detector (e.g. a PIN diode). The relative timing of the pulses is determined by specialized electronics. Here we describe one approach based on fast NIM (Nuclear Instrument Module) electronics originally developed for use in particle physics and in neutron and gamma detectors. Both detector signals are used generate timing pulses in a timing discriminator, such as a threshold discriminator (TD), or a constant-fraction discriminator (CFD). A threshold discriminator outputs a timing pulse whenever the input voltage from a pulse crosses a certain threshold voltage. A disadvantage of this type of discriminator is that timing pulses are output at different times for pulses with varying amplitudes but equivalent arrival times, thus increasing the timing uncertainty. This timing uncertainty is remedied

using a constant fraction discriminator. CFDs operate by splitting the voltage signal by a constant fraction, inverting, and delaying the split voltage signal by some constant amount of time, then recombining the signal. The time at which the voltage crosses zero is used to generate an output pulse. CFDs greatly reduce timing uncertainty due to differences in input signal amplitudes. The timing pulses from the PIN and APD are then sent to a time-to-amplitude converter (TAC), where the time between the arrival of the two pulses is measured by an analog linear voltage ramp that starts when one timing pulse (from the PIN) arrives and stops when the other timing pulse (from the APD) arrives. The analog signal from the TAC is passed to an analog-to-digital converter (ADC), where the analog voltage is converted into a bin number and stored in the memory of a multi-channel analyzer (MCA). Many photon arrival times are measured, and a histogram of photon arrival times is constructed, resulting in a fluorescence intensity decay trace convolved with the instrument response function (IRF). Fitting procedures (discussed in detail in section 2.4.3) are then employed to separate the intensity decay signal from the IRF signal and determine the time constants from the intensity decay. The specific components of our TCSPC setup and experimental details are discussed in the next section.

There are several types of single-photon detectors, such as photomultiplier tubes (PMTs), of which there are dynode chain PMTs (which convert photons into electron current via the photoelectric effect, multiplied many times over as photoelectrons bounce off of a chain of dynodes) and micro-channel plate PMTs (containing many narrow channels lined with dynode material which multiply photoelectrons as they bounce off of

the walls of the channels in transit down the channel), or diode detectors such as single-photon avalanche photodiodes (SPADs or APDs, where electron current results from an avalanche of electrons following photon absorption. The avalanche is generated by impact ionization with semiconductor atoms in a reverse biased P-N junction). The key difference between each detector is in the minimum temporal resolution each type affords. APDs and MCP-PMTs afford the best time resolution at tens of picoseconds, whereas dynode chain PMTs typically afford time resolution from hundreds of picoseconds to ~1 ns.[47]

When polarizers are incorporated into a time-resolved fluorescence setup, then it becomes possible to measure the fluorescence anisotropy decay of the system, which is a measurement of the depolarization of fluorescence after being excited by a linearly polarized source. Fluorescence anisotropy can decay by either by rotation or other mechanisms (such as energy transfer), and measuring the anisotropy decay quantifies the rates of these depolarization processes. If depolarization is due to energy transfer mechanisms, it is possible to probe phenomena such as incoherent energy transfer (using either ultrafast or slower methods). When fluorescence anisotropy decay methods are taken in conjunction with fluorescence lifetime measurements, it is possible to determine the average number of energy transfer events occurring within the excited state lifetime (as discussed previously in Chapter 1). Thus, time-resolved spectroscopy can be a very versatile tool for exploring the photophysics of a fluorescent system.[47]

2.4.2. TCSPC Setup and Experiment

Picosecond fluorescence lifetimes were measured in air and under nitrogen using a home-built setup for time-correlated single photon counting (TCSPC) spectroscopy operating in either forward or reverse mode. Frequency doubled pulses (420 nm) from a passively (Kerr lens) mode-locked Ti:Sapphire laser (Coherent Mira 900, 840 nm pulses, ~150 fs pulsewidth, 76 MHz rep. rate) were used as the excitation source for the nanoparticle samples. The non-linear medium used for second harmonic generation (SHG/frequency doubling) was a β-barium borate crystal (BBO, Type I, 100 μm thick, AR-coated, SHG range 760-840 nm). Fluorescence was collected perpendicular to the excitation source and passed through a 460 nm long pass filter, and a calcite Glan-Taylor linear polarizer (Thorlabs, GT10-A) oriented at magic angle (55°) to the vertically polarized excitation pulses. For (unpolarized) TCSPC measurement, the polarizer is oriented at 55° (magic angle) since the intensity decay collected at this orientation corresponds to the sum of the fluorescence intensity in the x, y, and z planes, given by $S(t) = I_{\parallel}(t) + 2I_{\perp}(t)$, as previously discussed in Chapter 1.[95] One-inch diameter, plano-convex lenses were utilized throughout the setup to focus or collimate light as necessary (75 mm focal length lens to focus on APD and 50 mm focal length lenses elsewhere, c.f. Fig 2.2). For the experiments in Chapter 3, the output of a fast PIN diode (Thorlabs, DET210) was used as the start timing pulse for a time-to-amplitude converter (TAC, Canberra Model 2145), and the output of a single photon avalanche photodiode (APD, id Quantique, id100-50) was used as the stop timing pulse. For the experiments in Chapter 4, the detector outputs are switched, in a standard reverse-mode configuration.[119] The excitation power was attenuated (between ~300 μW and 1 mW, typ.) to maintain a count

rate of ~400 kHz as measured at the APD (to ensure that the probability of two fluorescence photons arriving from one laser pulse is under 10%). The analog TAC output was digitized using a 13-bit multi-channel analyzer (FastComTec, MCA-3A). Before and after each measurement an instrument response function (IRF) was measured using scattered excitation light from a dilute suspension of polystyrene microspheres. The width of the IRF was determined to be ~70 ps (fwhm). Typical peak signal-to-noise ratios (SNR) for each run (limited to ~10 minutes per run, to minimize the effect of timing drift) were between 200:1-500:1 in reverse mode, and 50:1-100:1 in forward mode. The dwell time per MCA bin was determined by measuring an IRF sample and varying the delay times on the TAC until the 20 ns sample window contained two IRF peaks. The bin spacing between the IRF peaks was measured, and then used in conjunction with the measured repetition rate of the Ti:sapphire laser (a 76 MHz repetition rate corresponds to ~13 ns between laser pulses) to determine a dwell time of 2.6333 ps/bin.

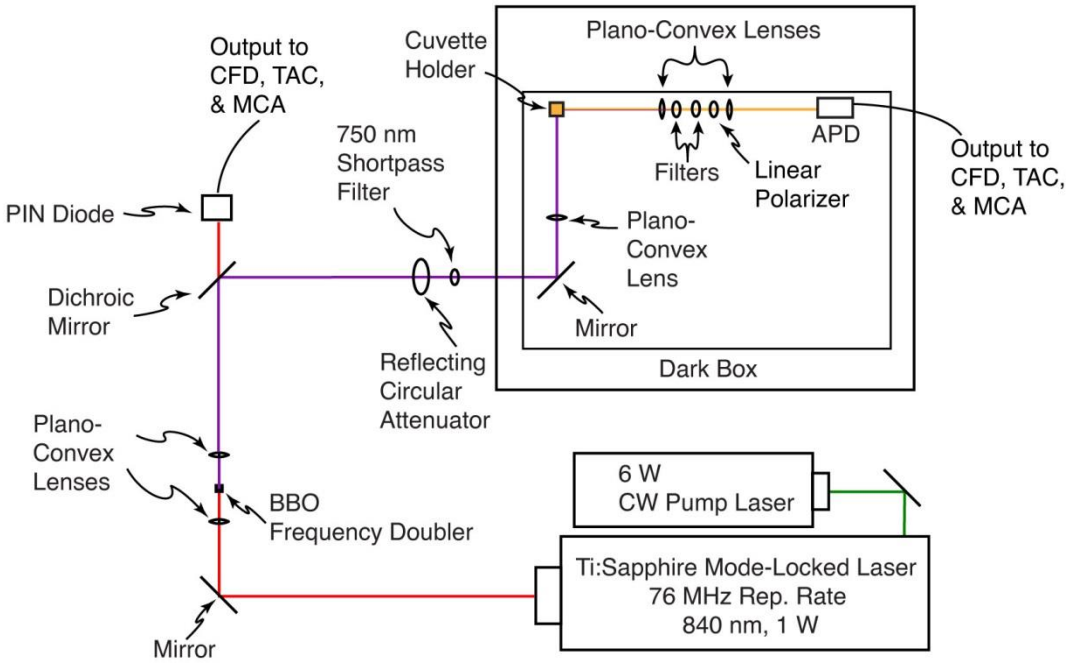

Fig. 2.2. Time-Correlated Single Photon Counting and Fluorescence Anisotropy Decay setup.

Due to the random nature of photon arrival, the SNR is determined from the Poisson probability distribution function (PDF), given by

$$f(n;N) = \frac{N^n \exp(-N)}{n!}, \tag{2.7}$$

which gives the probability of recording n counts in a measurement of finite duration, with the mean of the distribution given by N. In the limit of an infinite number of measurements, the width of the distribution, given by σ_n is proportional to the mean of the distribution as

$$\sigma_n = \sqrt{N}. \tag{2.8}$$

Given the average signal (average number of photon counts) N and given that the noise is approximated by Equation 2.8, the signal-to-noise ratio is given by:

$$SNR \approx \frac{N}{\sigma_n} \approx \frac{N}{\sqrt{N}} \approx \sqrt{N} \tag{2.9}$$

(e.g. 10,000 photon counts at the peak results in a SNR of 100:1).

2.4.3 TCSPC Fitting Procedure

As mentioned in the previous section, the sample trace obtained by TCSPC $S(t)$ is a convolution of an instrument response function $IRF(t)$ with the true fluorescence intensity decay of the sample $F(t)$ (c.f. Fig 2.3). It will be shown below that convolution in the time domain is essentially a time-shifted overlap calculation between two functions. If one function has broader features compared to the second (e.g., if $IRF(t)$ has large temporal width compared to the temporal features of $F(t)$), the narrower features of the second function are consequently broadened in the convolution of the two (this is

sometimes termed "smearing"). Typically, one function is given by a signal or stream of data (Fig 2.3b, in TCSPC this is the fluorescence decay), and the other function is a peaked function that drops to zero on either side of the peak (Fig 2.3a, in TCSPC, this is given by the instrument response function of the detector). This is expressed generally by:

$$S(t) = IRF(t) \otimes F(t). \tag{2.10}$$

The convolution is calculated by shifting one function in time and multiplying the two functions for each shift in time. For continuous functions, the convolution is given by:

$$IRF(t) \otimes F(t) = \int_{-\infty}^{\infty} IRF(\tau) F(t-\tau) d\tau \,, \tag{2.11}$$

and the integral in Eq. 2.11 becomes a finite summation over the duration of the IRF for discrete functions. Another way to express Eq. 2.10 is in terms of the Fourier Transforms of $IRF(t)$ and $F(t)$:

$$FFT[IRF(t) \otimes F(t)] = IRF(\omega) F(\omega), \tag{2.12}$$

where ω is used to denote the frequency domain following Fourier Transformation. Thus, the convolution of two time domain functions is computed by multiplication of the respective Fourier Transforms. For discrete functions, this is calculated using Fast Fourier Transform (FFT) methods in order to compute the convolution efficiently. Thus, the convolution is calculated by computing the FFT of both $IRF(t)$ and $F(t)$ to give $IRF(\omega)$ and $F(\omega)$, multiplying them, and then computing the inverse FFT of the resulting product to return the convolution in the time domain (c.f. fig 2.3c).[120]

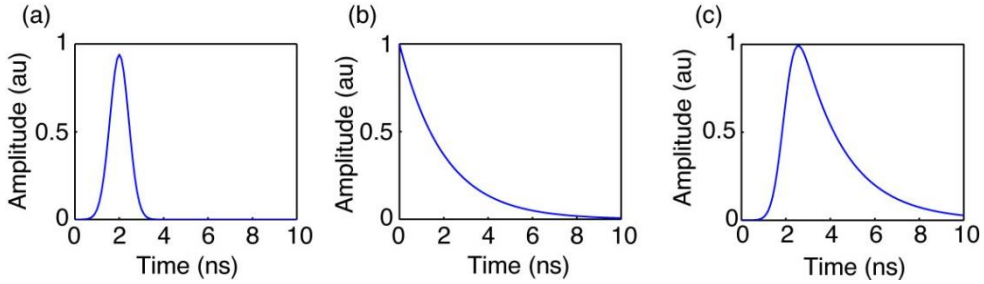

Fig. 2.3. Example of discrete convolution in which (a) a Gaussian instrument response function with 1 ns fwhm is convolved with (b) a single exponential decay with $\tau = 2$ ns to produce (c) the convolution of (a) and (b). The result depicted in (c) exemplifies the shape of an intensity decay trace measured using TCSPC.

By measuring both $S(t)$ and $IRF(t)$, we have all of the information we need to determine $F(t)$. This method of fitting works by convolving the measured IRF with a trial decay function, typically one of various exponential decay functions in this case, of the basic form $F_{trial}(t) = A_0 \exp(-t/\tau)$, where A_0 is the amplitude of the function at time t_0, and τ is the time constant (for a single exponential decay). Thus, 2.10 becomes

$$S_{sim}(t) = IRF(t) \otimes F_{trial}(t), \tag{2.13}$$

where $S_{sim}(t)$ is the simulated decay trace. $S_{sim}(t)$ is then compared to $S(t)$, and the quality of fit is assessed by calculating the sum of the squared residuals, given by:

$$SSR(t) = \sum_{i=1}^{n} (S(t_i) - S_{sim}(t_i))^2. \tag{2.14}$$

The parameters in $F_{trial}(t)$ are varied by random number generation between preset lower and upper bounds (the parameters are A_0, t_0, and τ for a single exponential, given above), and if the trial parameters yield a better fit (lower sum of squared residuals), the parameters are saved before moving onto the next calculation. This is repeated for thousands of iterations until the best guess of fit parameters to $F(t)$ is found. The aforementioned random number minimization is used in conjunction with linear least-squares fitting in order to fit the linear coefficients (e.g., A_0). After the minimization is complete, the residuals are assessed for any systematic deviations (e.g., the best fit between $S_{sim}(t)$ and $S(t)$ will yield a flat residuals trace). This method of fitting analysis affords time resolution below the fwhm of the measured IRF, with a typical lower limit in determining accurate time constants as short as ~10-20% of the IRF width (e.g. 7-14 ps for a 70 ps fwhm IRF).[121,122] The main reason for this limitation is due to drift in the TCSPC timing electronics (i.e., shifting of the IRF), which occurs on the time scale of a

few picoseconds. As such, time constants of less than about 10-20% the width of the IRF are regarded as suspect, either indicating a poor-quality data set, poor choice of fitting function, or an experimental issue such as leakage of excitation light into the detector, excess laser noise, cabling issues, improper discriminator settings, etc.

While other fitting methods exist that would successfully minimize a single-exponential decay function such as downhill simplex or Newton-Raphson minimization methods,[120] CPN intensity decay kinetics are typically described by more complex exponential functions, such as weighted sums of exponential decays (bi-exponential or multiexponential functions), the Kolrausch-Williams-Watts (KWW or stretched exponential) function, given by

$$F(t) = A_0 \exp(-(t/\tau)^{\beta}), \tag{2.15}$$

(where β is a number typically between ~0.2 and 1, where β = 1 yields a single exponential decay),[123] or a weighted sum of a KWW function with an exponential decay (in the case of fluorescence anisotropy decay analysis, given in Chapter 4). Difficulties arise when fitting complex exponential decays using methods such as downhill simplex due to local minima encountered when minimizing Eq. 2.13, which necessitates an exhaustive, random search across the parameter space to ensure that the global minimum of Eq. 2.13 is found.

2.4.4 Validation of the TCSPC Instrument

There are several sources of artifacts in TCSPC, including afterpulsing in detectors, stray reflections in the apparatus, improper triggering (e.g., triggering on a ring

instead of on the principal pulse), and signal reflections and nonlinearities in the timing and readout electronics. As such, precautions must be taken to ensure that data being collected in these experiments is of the highest possible quality. The instrument was carefully aligned, and baffles were employed to minimize stray light. Discriminator levels were adjusted to minimize the width of the instrument response function and minimize ringing. Proper impedance matching was employed. While there is a slight ring apparent in results obtained for samples with lifetimes greater than ~2 ns (c.f. Fig 3 in Chapter 3), we have validated the accuracy of the instrument using several standard dyes, including fluorescein in 0.01 M NaOH (τ = 4.1 ns),[112] coumarin 6 in ethanol (τ = 2.5 ns),[124] and perylene red in THF (τ = 5.6 ns).[125] All lifetimes measured were within 10% of the literature values, indicating that the ringing, while visible, has a negligible effect on the lifetime results obtained.

2.5 Picosecond Fluorescence Anisotropy Decay (FAD)

Fluorescence anisotropy decay (FAD) measurements were performed using the aforementioned TCSPC setup, with the addition of a calcite Glan-Taylor linear polarizer (Thorlabs GT-10A) placed after the filter set, and before the focusing lens. For fluorescence anisotropy decay measurement, intensity decays and IRFs were collected at all three polarizer orientations. Unlike TCSPC, the excitation power is attenuated once and then held constant in the FAD experiment (rather than variably attenuated for each sample) in order to avoid systematic deviations in the anisotropy signal due to inconsistent excitation power. The excitation power is selected so that the collected

emission at each polarizer orientation yields a count rate between 200 kHz and 800 KHz as measured on the APD. Typically, the strongest emission is collected when the emission polarizer is parallel to the excitation. The FAD least-squares fitting analysis is similar to the iterative convolution fitting procedure outlined in Section 2.4.3, with adaptations from a procedure given by Fleming, et al.[95] Further detail will be given in Chapter 4.

CHAPTER THREE

MEASUREMENT OF EXCITON TRANSPORT IN DYE-DOPED AND BLENDED CONJUGATED POLYMER NANOPARTICLES

3.1 Introduction

In recent years, there has been a great deal of interest in conjugated polymers, largely due to their application as the active materials in flexible, low-cost, highly efficient photovoltaic[1] and light-emitting devices.[2] Conjugated polymer nanoparticles (CPNs) are of interest for use in biological imaging, given their high fluorescence brightness, extraordinary two-photon fluorescence cross-sections, and excellent photostability.[17,73,101,126-129] It is increasingly clear that further development of applications requires additional understanding of the complex photophysics and photochemistry of conjugated polymers, as well as their dependence on polymer structure and processing conditions. In organic semiconductors, the principal neutral electronic excitation of interest is typically the Frenkel-type singlet exciton.[130,131] Energy transfer between sites or chromophores occurs via multiple processes, including incoherent, diffusion-like processes,[8,132,133] dispersive transport,[32] and in some cases, via ultrafast, long range coherent transport.[30] In the exciton diffusion picture, each polymer chain is

considered to consist of several more or less independent chromophores or exciton sites, and excitations transfer from one site to other nearby sites via transition dipole-mediated Förster transfer.[134] Multiple excitation transfer events typically occur during the excited state lifetime, resulting in a random walk-like process characterized by a diffusion constant or length. A large exciton diffusion length is required for optimum photovoltaic device efficiency (for some device types), since excitons must travel to the heterojunction to undergo charge separation. While the exciton diffusion length in high purity, crystalline inorganic semiconductors can reach several microns,[86] it is typically much shorter for organic semiconductors. For example, measured exciton diffusion lengths for single crystals of anthracene range from ~30 nm to 60 nm,[87-89] and diffusion lengths of under 15 nm are typically reported for conjugated polymers.[13,90,91] Interacting chromophores can also give rise to aggregate species such as dimers, H- and J-aggregates, excimers, and exciplexes.[74,75] Energy transfer can also occur to these and other species such as excess charges (polarons),[7] defects introduced during polymer synthesis or processing,[36] or dopant species such as dyes and other polymers.[11,13] These processes can significantly reduce the observed exciton diffusion length. Various experimental methods have been developed for characterizing exciton diffusion, including photoluminescence quenching in layered structures,[8,94] confocal fluorescence microscopy,[135,136] near-field fluorescence microscopy,[3,56,137] time-resolved fluorescence of dye-doped films, crystals, or nanoparticles,[13,90,133,138] and single particle imaging.[139,64] Different assumptions are involved in the various methods, each contributing to different

types of systematic error or bias, leading to a wide range of reported exciton diffusion lengths, as discussed by Forrest *et al*.[92]

Here, we examine some processes relevant to the determination of exciton diffusion constants in dye-doped conjugated polymer nanoparticles by way of time-resolved fluorescence spectroscopy. In particular, we examine the effects of quenching by defects on the observed quenching efficiencies and excited state dynamics. While quenching by defects[36] and hole polarons[64] has been observed, quenching by defects is rarely quantified in studies of exciton transport dynamics in conjugated polymers, perhaps since it is preferable to minimize defects by employing proper technique. However, in some cases defects can be difficult to avoid entirely, or there may be quenching by intrinsic species such as aggregates, exciplexes, or photogenerated polarons. Furthermore, the combination of energy transfer and exciton diffusion can result in quenching radii as large as 10 nm.[140] Thus, even very low concentrations of defects or other quenching species could give rise to significant quenching. Additionally, quenching by hole polarons is significant at a polaron density of 5×10^{17} cm^{-3},[7,72] which is often exceeded in functioning devices. We observe complex fluorescence decay dynamics consistent with significant quenching by defects in undoped nanoparticles of MEH-PPV and PFBT. Therefore, we develop a modified approach to determining exciton diffusion parameters that explicitly includes quenching by defects. By fitting the quenching efficiencies and complex fluorescence decay kinetics to an exciton diffusion model that explicitly includes quenching by defects, we obtain a corrected exciton diffusion length for nanoparticles of the polymer PFBT. Our results indicate typical

analysis ignoring defects results in underestimation of L_D by roughly a factor of 2. Analysis of the distribution of lifetimes provided additional confirmation of quenching by defects: The fluorescence decays of doped and undoped particles were fit to a stretched exponential function, yielding a stretch parameter β, which typically varies between ~0.3, indicating a broad distribution of lifetimes, and ~1.0, indicating a very narrow distribution (a single lifetime). Fitting the dynamics of undoped particles yielded $\beta = 0.6$, consistent with significant quenching by defects. Analysis of the radiative and non-radiative rates was also consistent with quenching by defects. Our results indicate that quenching by defects can lead to significant underestimation of the exciton diffusion length, particularly for highly mobile excitons, which are highly susceptible to quenching, even at very low densities of quenching species or defects. The results are also promising for applications requiring highly mobile excitons, such as photovoltaic devices, since improvements in exciton diffusion length by a factor of 2 or more are expected if quenching by defects can be substantially reduced.

3.2 Doped Nanoparticle Preparation Details

Dye doped and blended conjugated polymer nanoparticles were prepared using the method described in Chapter 2.2. The specific details pertaining to the doping procedure are given as follows. Varying amounts of the dopant perylene red solution were mixed with the PFBT solution to produce solution mixtures with a concentration of 20 ppm PFBT and dopant/host fractions of 0 to 2 wt% perylene red. The mixtures were sonicated very briefly (3-5 s) to ensure homogeneity. For blended nanoparticles, varying

amounts of dopant polymer MEH-PPV solution were mixed with a solution of host polymer PFBT solution to produce mixture solutions with a total polymer concentration of 20 ppm and a ratio of MEH-PPV/PFBT ranging from 0% to 10 wt %. A 2 mL quantity of each solution mixture was added rapidly to 8 mL of deionized water under sonication for ~30 s at a sonication frequency of 40 kHz and room temperature.

3.3 Characterization Methods

Size distributions and morphologies of undoped and perylene red doped PFBT nanoparticles were determined by atomic force microscopy (AFM). Samples were prepared by functionalizing the surface of a freshly cleaned glass coverslip with 3-aminopropyl-trimethoxysilane in anhydrous ethanol, followed by dipping in a diluted nanoparticle suspension for 40 minutes, then removing the coverslip and allowing it to dry overnight in an enclosed environment. Surface topographies were measured on an Ambios Q250 multimode AFM in tapping mode. The mean diameter of the CPNs was measured at 8 ± 2 nm. All of the perylene red doped PFBT CPN samples showed no substantial changes in mean diameter, with a similar size distribution.

UV-Vis absorption spectra were collected on a Shimadzu UV2101PC scanning spectrophotometer using 1 cm quartz cuvettes. Fluorescence spectra were collected and fluorescence quantum yield was measured using a commercial fluorimeter (Quantamaster, Photon Technology International, Inc.) using 1 cm quartz cuvettes. The UV-Vis spectra showed no variations from the undoped spectrum over the range of doping, and the absorbance of perylene red was well below the limit of detection of the

instrument in the CPN suspensions. The fluorescence spectra of the CPN samples are given in Figure 3.3. The decreased lifetimes of the particles as compared to the polymer in good solvent are not likely to be due to J-aggregate formation, since little shift in the polymer absorption spectrum is observed upon nanoparticle formation (c.f. Fig. 3.1).

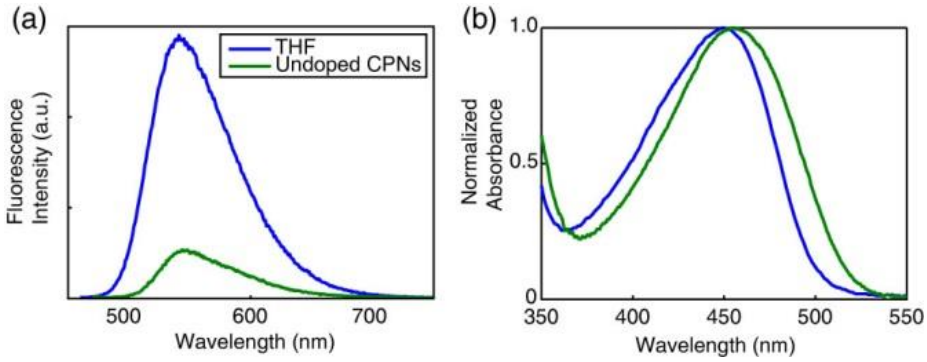

Fig. 3.1. (a) Fluorescence spectra and (b) normalized absorbance spectra of PFBT in THF (blue) and undoped PFBT CPNs (green).

The standard fluorescent dye fluorescein in 0.01 M sodium hydroxide was utilized to determine the fluorescence quantum yield of the PFBT CPN samples. 473 nm was selected as the excitation wavelength. The concentrations of the standard and nanoparticle suspensions were adjusted to yield an absorbance of ~0.05 at 473 nm. The absorbance, integrated fluorescence, and refractive indices of the sample and standard solutions were used in conjunction with the literature value of 0.92 for the quantum yield of fluorescein in 0.01 M sodium hydroxide to calculate the fluorescence quantum yield of the nanoparticle suspensions.[113] The results of the quantum yield measurements are given in Figure 3.3 (c.f. Section 3.4). A Förster radius of 3 nm for the PFBT/perylene red donor/acceptor pair was calculated utilizing the absorption spectrum of perylene red in THF and the emission spectrum of undoped PFBT CPNs using standard methods,[47] correcting for the polymer refractive index and assuming an orientation factor of $\kappa^2 = 2/3$, which is the standard result for dynamic reorientation of transition dipoles.

Fluorescence lifetimes were measured in air using the TCSPC method described in Chapter 2, with the instrument running in forward mode. Nanoparticle fluorescence was collected perpendicular to the excitation source after passing through a 460 nm long pass filter for the undoped nanoparticles. An additional 540 ±10 nm band pass filter was added for the doped samples in order to filter out the emission from perylene red. The excitation pulse was attenuated to maintain a valid start/stop event count rate of ~6 kHz. Several TCSPC kinetics traces were obtained for each sample. Data was acquired until roughly 10^3-10^4 photons had been collected. Typical signal-to-noise ratios were above 50:1 for the samples and 100:1 for the IRF.

3.4 Initial characterization of dye-doped PFBT CPNs.

Doping of conjugated polymer nanoparticles (CPNs) with dyes is being pursued as a strategy for improving their brightness and photostability while red-shifting their fluorescence, and as a way to investigate exciton diffusion in conjugated polymers. PFBT was selected as the host polymer owing to its excellent photostability and high fluorescence quantum yield, as well as its broad fluorescence spectrum, which facilitates energy transfer to dyes.[13] Perylene red was selected as the dye dopant for this system due to the excellent spectral overlap with the emission spectrum of PFBT and its high fluorescence quantum yield (0.96 in chloroform).[141,142] Perylene red-doped PFBT CPNs were prepared via a nano-precipitation method described previously.[97] Samples were filtered through a 0.1 μm membrane filter and characterized via UV-Vis and fluorescence spectroscopy. Size distributions were determined via particle height analysis of representative AFM images (c.f. Fig. 3.2). The AFM images are consistent with spherical nanoparticles, as is expected for glassy polymers in this size range, based on surface free energy considerations. Terentjev et al. previously reported spherical morphology for particles of PFBT roughly in this size range.[100]

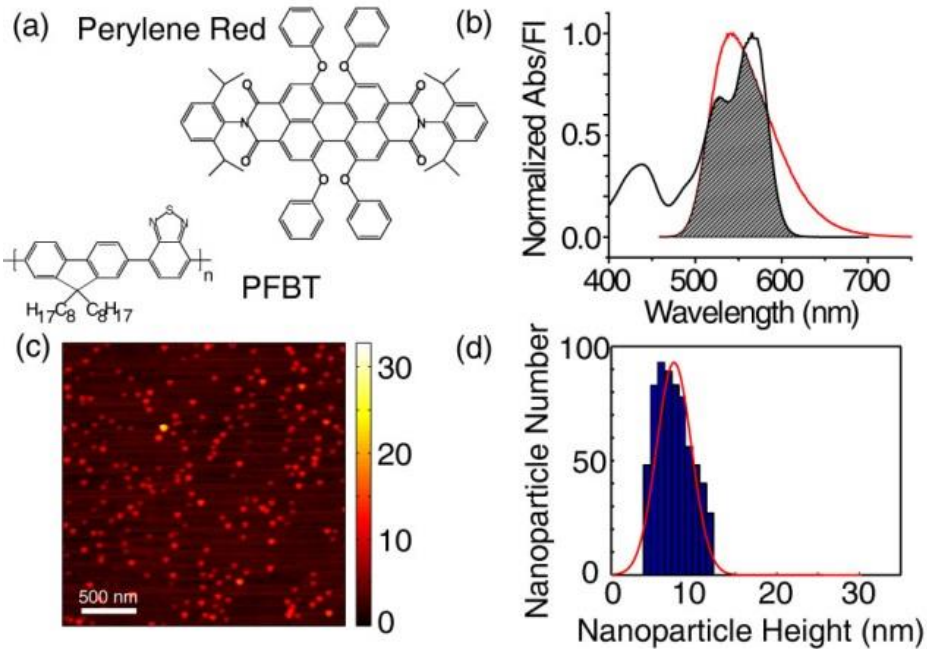

Fig. 3.2. (a) Structures of perylene red and PFBT. (b) Normalized perylene red absorbance (black line) and PFBT fluorescence (red line) in THF with spectral overlap region shaded. (c, d) Representative AFM image of undoped PFBT CPNs and particle size histogram.

Energy transfer efficiency as high as 86% was observed at 2% doping, where the energy transfer efficiency is given by $\eta_{ET} = 1 - F/F_0$, and F, F_0 are the host fluorescence intensity in the presence, absence of dopant, respectively (c.f. Fig 3.3). It was expected that most of the dye is incorporated into the nanoparticles owing to the hydrophobic character of the dye, based on previous results examining incorporation of dyes with similar solubility properties, using centrifugal concentration to examine dye incorporation and possible leaching.[13] Additionally, the lack of additional features in the UV-vis and fluorescence spectra that could be ascribed to free dye or dye aggregate in solution is evidence that the fraction of unincorporated dye is small (less than a few percent). Finally, the high energy transfer efficiency at low doping ratios provides additional confirmation that a high fraction of the dye molecules are incorporated in the nanoparticles. The intensity of acceptor emission in the doped samples increases as dopant is added up to 0.5% doping. Upon further doping, acceptor emission intensity decreases. We ascribe this to aggregation quenching of the acceptor as dye dimers form within the nanoparticle at higher doping levels. Aggregate formation could also explain the red shift of the acceptor emission observed at higher doping levels. Stern-Volmer analysis was performed using the quencher/donor molecular fraction $f = n_{dye}/n_{poly}$ as the unit of concentration, in order to obtain K_{SV} in terms of the number of polymer molecules quenched per perylene red molecule. The analysis yields a quenching constant of 37 per dye molecule, indicating that roughly 37 PFBT molecules are quenched per dye molecule. From this result, an effective dye quenching radius of 5.3 nm is obtained,

which is significantly larger than the calculated Förster radius, providing initial indication of exciton diffusion.

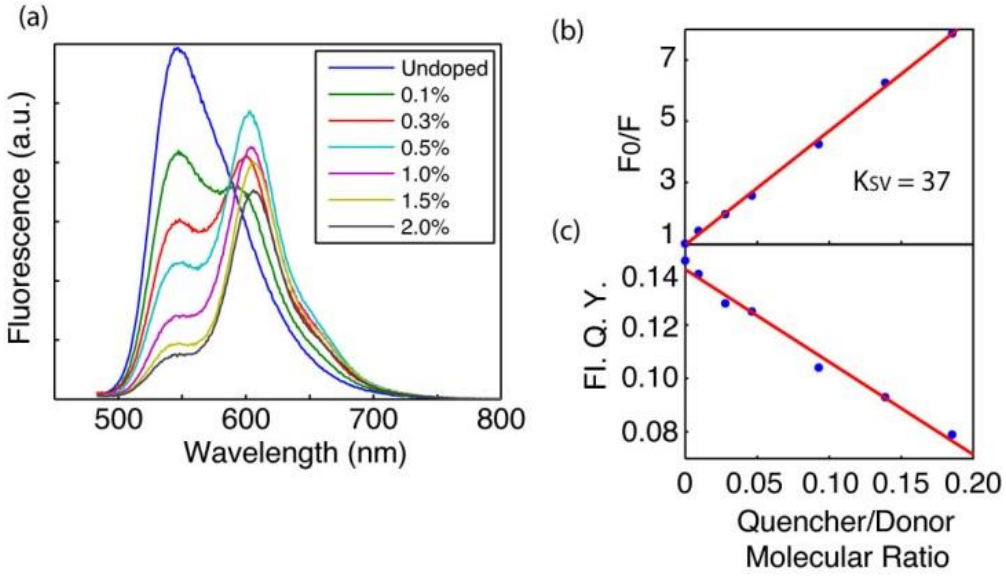

Fig. 3.3. (a) Fluorescence spectra of perylene red doped PFBT CPNs at various doping ratios. (b) Stern-Volmer quenching plot. (c) Total fluorescence quantum yield vs. quencher-donor molecular ratio.

The quantum yield of undoped PFBT CPNs was measured to be 0.14, consistent with prior measurements.[16,17,143] The total fluorescence quantum yield of the doped samples decreases monotonically with increasing dopant concentration, indicating that doping with this dye does not increase CPN brightness as initially hoped (c.f. Fig 3.3). However, at moderate doping levels (0.5%-1%), the decrease in fluorescence quantum yield is minimal, while the energy transfer efficiency is high, thus doping with perylene red can be used to red-shift the fluorescence while maintaining high levels of brightness. In microscopic imaging experiments, signal levels and contrast are affected by several phenomena and factors related to the spectroscopy of the dyes and the experimental setup.[12] A key issue is autofluorescence from the sample and from the various optical materials. Autofluorescence typically peaks a few nm to the red of the excitation wavelength, with a long red tail. Thus, for typical dyes with small Stokes shifts, selection of filters involves a compromise between efficient collection of the emission of interest and rejection of autofluorescence. The PFBT nanoparticles doped with perylene red exhibit a large red-shift in the emission, which is advantageous for efficient collection of fluorescence and rejection of autofluorescence.

The effect of quenching by molecular oxygen on the quantum yield of the undoped PFBT CPN samples was assessed by purging the sample with nitrogen in the dark for 45 minutes prior to measurement. The quantum yield in air was measured to be 0.097, and 0.100 in nitrogen. The differences in quantum yield for the sample in air compared to the data in Figure 3.3 are not statistically significant, indicating negligible fluorescence quenching by oxygen.

3.5 Picosecond time-resolved fluorescence spectroscopy

Time-correlated single photon counting (TCSPC) was employed to determine the lifetimes of the excited state in doped and undoped nanoparticles of PFBT, and for the polymer dissolved in THF. The decay trace was fit by a least-squares minimization procedure involving convolution of a trial decay function with the instrument response function. The trial functions are (single) exponential, bi-exponential, and the stretched exponential or Kohlrausch-Williams-Watts (KWW) function,

$$F(t) = A\exp(-(t/\tau)^{\beta}). \tag{3.1}$$

The stretch-parameter β acts as a measure of lifetime heterogeneity, ranging between ~0.3 and 1, where lower values indicate a broad distribution of lifetimes while β = 1 corresponds to a single lifetime.[123] The fluorescence decay of PFBT in THF was adequately fit by a single exponential, while the decays of undoped nanoparticles and lightly to moderately-doped particles (0.1%-1.0%) exhibited complex decay kinetics that fit well to both bi-exponential and stretched exponential (KWW) functions. While single exponential fits converged for all samples, bi-exponential and KWW fits did not converge for 1.5% and 2% doping due to low signal levels and short lifetimes relative to the width of the instrument response function. Results show a clear decreasing trend in lifetimes as the doping ratio is increased, with perhaps a slight decreasing trend in β (c.f. Fig 3.4), though it is not clear that the decrease is statistically significant. In any case, the β values indicate a broad distribution of exciton lifetimes for the nanoparticles, consistent with energy transfer in dense multichromophoric systems,[13] while the polymer in THF

yielded β values near unity, suggesting little energy transfer. Overall, the weighted average lifetimes and β values obtained from the fits are consistent with the physical picture of exciton diffusion and energy transfer, i.e., dynamic quenching due to energy transfer, which will be discussed in more detail below.

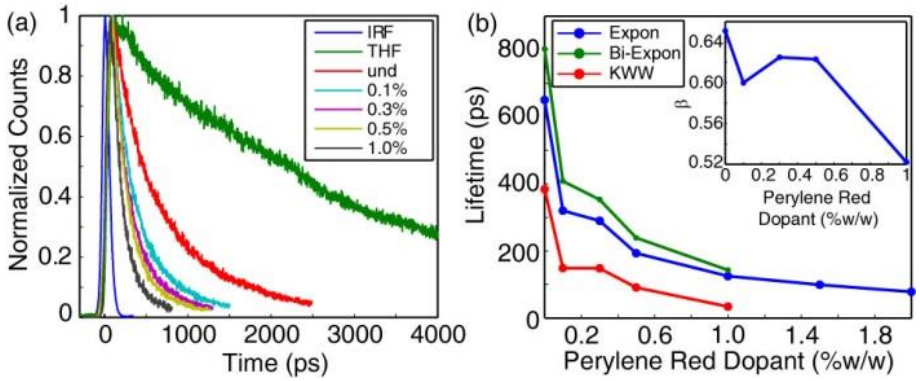

Fig. 3.4. (a) Normalized fluorescence lifetime decay traces for PFBT in THF and doped CPNs. (b) Single exponential (blue), bi-exponential weighted average (green), and KWW (red) lifetimes of perylene red doped CPNs. Inset: KWW heterogeneity parameter ß vs. perylene red dopant percent.

Fitting was performed using a set of custom MATLAB scripts. Briefly, the fitting procedure is as follows. The model function consisted of either a single exponential, a bi-exponential, or a KWW decay function. Conventional gradient-based nonlinear least squares minimization methods such as Levenberg-Marquardt often fail for multi-exponential fitting, so an alternative approach was employed. A random number generator was used to generate a series of guesses for the nonlinear parameters (including shifts in t_0, since small shifts in timing can occur due to drift) over a selected range. Then, for each set of nonlinear guess parameters, the trial fit function is convolved with the instrument response function and the linear parameters (i.e., the exponential amplitudes) are determined by linear least-squares. The sum of the square of the residuals (square error) for the set of parameters is calculated and compared to the minimum square error obtained thus far. If the new value is lower, then the parameters and the square error are saved. After several thousand iterations, the set of parameters corresponding to the minimum square error is taken as the set of best-fit parameters. The soundness of the fit is tested by additional sets of iterations with both wider and narrower ranges for the guesses, and by visual inspection of the residuals. Additionally, the range of data included in the fitting analysis, as well as the degree of downsampling of the data were varied, and the effect on the resulting fit parameters was evaluated. The fitting results for several TCSPC kinetics traces for each sample were used to determine the mean and standard deviation of the parameter values. Typical standard deviations of better than 10% were obtained for the lifetime values.

The effect of quenching by molecular oxygen on the lifetime of the nanoparticle samples was also assessed by comparing the lifetime results obtained for samples exposed to air with those obtained from nitrogen-purged samples. The bi-exponential weighted average lifetimes of the undoped PFBT CPNs were measured to be 780 ps in air and 850 ps in nitrogen. This difference is not statistically significant, and is in agreement with the quantum yield measurements indicating minimal quenching by oxygen.

In addition to the lifetimes of the host polymer PFBT, the lifetimes of the acceptor perylene red were measured. The lifetime of perylene red in THF was measured to be 5.4 ns, which is consistent with the literature value.[125] The moderate to heavily doped samples of PFBT nanoparticles were selected due to the relatively low contribution to the emission signal by PFBT as well as to assess the effect of the observed self-quenching of perylene red on its lifetime in the nanoparticles. The lifetime of perylene red doped within the nanoparticles was found to be reduced to 3.1 ns, and follows a decreasing trend as doping increases. The reduction in lifetime indicates dynamic self-quenching.

Perylene Red %(w/w)	τ_{exp} (ns)
THF	5.4
1.0%	3.1
1.5%	2.9
2.0%	2.6

Table 3.1. Fluorescence lifetimes of the energy acceptor fluorescent dye Perylene Red in THF and in dye-doped PFBT CPNs.

3.6 Modeling Exciton Diffusion and Energy Transfer in Dye-Doped CPNs

Exciton dynamics in doped conjugated polymers can be described as mobile excitons hopping from site to site in a random, diffusion-like process prior to decaying (both radiatively and non-radiatively) or undergoing energy transfer to a defect or dopant molecule.[144-146] In this picture, a key exciton transport parameter is the diffusion length, $L_D = \sqrt{2nD\tau}$, where n is the dimensionality, D is the (1D) diffusion constant, and τ is the exciton lifetime. We previously developed a numerical random walk approach to modeling the combined effects of exciton diffusion and energy transfer in CPNs, which yielded values for energy transfer efficiency that were in agreement with experimental results for dye-doped CPNs.[13] This approach was also applied to modeling fluctuations in the fluorescence centroid of a single CPN due to polaron motion.[64] Here, we have modified the previous simulation code to provide kinetics information for comparison to the time-resolved fluorescence results. We have also modified our approach to explicitly account for quenching by defects. Neither coherent transport nor dispersive transport are

explicitly included in the present approach.[30,32] The simulation algorithm is described as follows. The simulation code was written as a set of MATLAB scripts. Dopant dyes and/or defects are distributed randomly within the nanoparticle, represented by a sphere. While a sphere is assumed, similar results are obtained assuming a cubic particle.[64,139] Here we define "defects" as any of a number of quenching species such as polarons, aggregate species, conformational defects, oxidized defects and synthetic defects, which are not deliberately introduced into the system, in contrast to the dye molecules, which are deliberately added in controlled amounts. In these simulations, dopant dyes are essentially treated as points within a continuum. However, the model may be adjusted to correct for finite dye volume effects (e.g. by adjusting the Förster radius). It is expected that the addition of an exclusion volume would have a minimal impact on the quenching dynamics and on the quenching efficiency, since the volume of the dye is less than 2% of the nanoparticle volume. Similarly, the dye volume is smaller than the quenching volume by a factor of 20 or more. Finally, we note that in previous simulations,[13] we employed a discrete lattice model, and found that the quenching efficiency obtained was not sensitive to the lattice spacing, for lattice spacing of 0.1 to 0.4 nm, which is consistent with the reasoning above. An initial population of excitons is also distributed randomly within the sphere. For each time step Δt, each exciton is propagated by adding to its position along each axis a Gaussian-distributed random number scaled so that $\sigma^2=2D\Delta t$, where D is the (1D) diffusion constant and σ^2 is the variance of the random number distribution ($\mu = 0$). A time step Δt of 1 ps was employed, and time steps of 0.2 ps, 0.5 ps, 2 ps, and 5 ps were also tested, to help ensure that the simulation results were not significantly affected by

numerical rounding errors or using a step that is too large given the various rates and diffusion distances involved. At each step, the new positions are checked to ensure that the exciton remains within the sphere representing the particle, and the jump is reversed for excitons that are outside the sphere, thus ensuring that the excitons remain within the sphere. The energy transfer rate, for each exciton to each dopant or defect, is calculated based on the exciton-acceptor distances and the conventional Förster rate expression,

$$k_{et} = \tau^{-1} \sum_{acceptors} (R_0 / R)^6 . \tag{3.2}$$

The probability of decay or transfer for a given exciton during the time step Δt is calculated by the expression

$$p(\Delta t) = 1 - e^{-k\Delta t} \tag{3.3}$$

where k is given by either $k_d = k_r + k_{nr} = \tau^{-1}$, or k_{et}, and compared to a random number to determine the exciton fate for that time step. The running total of excitons that have decayed via energy transfer is updated (for later use in determining the quenching efficiency), and the exciton population is updated (for later use in constructing a simulated kinetics trace), for each time step. The simulation continues until nearly all of the exciton population has decayed. The simulations are performed for many initial random configurations of acceptors and excitons, and the exciton population kinetics and energy transfer efficiencies are calculated from the simulation results.

We explicitly include exciton quenching by defects (which can include aggregates, polarons, excimers, synthetic defects, oxidized defects, etc.) as a key feature in our approach to modeling exciton diffusion and energy transfer in the nanoparticles.

The explicit inclusion of quenching by defects is based on several observations. First, the fluorescence quantum yield and excited state lifetime of the nanoparticles is greatly reduced (Φ = 0.14, τ_{avg} = 800 ps) as compared to the polymer in a good solvent such as THF (Φ = 0.66, τ_{avg} = 3000 ps). The phenomenon of reduced lifetimes in the aggregated state is often observed in J-aggregates, and is typically described as due to coupling of the transition dipole moments that causes a large increase in the radiative rate.[82] However, strong J-aggregate-type coupling is not likely to be responsible for the decrease in lifetime in the present case, since little shift in the absorption spectrum is observed upon nanoparticle formation (c.f. Fig. 3.1), indicating weak coupling. Next, the radiative rates of the polymer dissolved in THF and the nanoparticles suspended in water were determined as follows. For the nanoparticles, a fluorescence quantum yield (c.f. Fig. S1) of Φ = 0.14 and weighted average excited state lifetime of τ_{avg} = 800 ps was determined, while for the polymer dissolved in THF, Φ = 0.66, τ_{avg} = 3000 ps was determined. From this information and the quantum yield expression,

$$\Phi = \frac{k_r}{k_r + k_{nr}}. \tag{3.4}$$

a radiative rate value for the nanoparticles of 1.8×10^8 s^{-1} was determined, while for the polymer in THF, a radiative rate of 2.2×10^8 s^{-1} was determined. This does not correspond to typical J-aggregate behavior. Rather, the radiative rate typically increases for J-aggregates as compared to the unaggregated dye. Finally, the heterogeneity of the excited state lifetime of the nanoparticle is increased (β = 0.65) as compared to the free polymer in solution (β = 1.0), consistent with quenching by energy transfer to some type of defect

species, which could include oxidized defects, synthetic defects, aggregate species, exciplexes, and/or hole polarons (cations). Evidence for the existence of photogenerated hole polarons in PFBT CPNs is given in previously published work.[64] Additional support for the hypothesis of dynamic quenching by defects is given by analysis of the excited state lifetime and quantum yield results, which are not consistent with static quenching. Finally, the defect-quenching hypothesis is also supported by the agreement between experimental results and the exciton diffusion-energy transfer simulations, discussed below.

In order to account for quenching by defects in the simulation, the defect density (expressed as dye equivalents per nanoparticle) has been added as a model parameter. Exciton diffusion simulations were carried out for a particle of radius 4 nm, to match the 8 nm diameter determined by AFM (c.f. Fig. 3.2), with the exciton diffusion length set at 12 nm, and the time step set to 1 ps. In order to simulate a given dye and/or defect density, first the Poisson distribution of dyes or defects per nanoparticle was calculated by $f(n;\lambda) = \frac{\lambda^n e^{-\lambda}}{n!}$, based on the average number of dyes or defects per nanoparticle, (e.g., if λ = 1.7 dyes per particle on average, the Poisson distribution is used to estimate what population fraction of particles has n = 0, 1, 2, or 3 dyes, and so on) and simulations were performed assuming various numbers of dyes per nanoparticle, determined from the weight ratios of perylene red dopant. Then the kinetics curves and energy transfer efficiencies were combined using Poisson statistics to produce a weighted average

kinetics curve and energy transfer efficiency for the dopant density of interest. Initially, a Förster radius of 3 nm was calculated by

$$R_0^6 = \frac{9000\ln(10)\kappa^2\Phi_{THF}}{128\pi^5 Nn^4}\int_0^\infty F_D(\lambda)\varepsilon_A(\lambda)\lambda^4 d\lambda\,, \qquad (3.5)$$

using the refractive index of PFBT at the peak emission wavelength (~1.9),[147] the spectra of perylene red $\varepsilon_A(\lambda)$ and PFBT in THF $F_D(\lambda)$, the quantum yield of PFBT in THF, and assuming a value of 2/3 for the orientation factor κ^2.[47] However, while the match to experimental lifetimes and ß values improved, the simulation results did not match experimental quenching efficiencies well. It is likely that local ordering of the polymer could result in a somewhat larger value of the orientation factor, or that other physical processes such as coherent transport could lead to a larger quenching radius.[30,32] Thus, simulations were carried out using an increased R_0 of 4 nm. This improved the agreement with experimental quenching efficiencies. It is assumed that a combination of exciton diffusion and energy transfer in the aggregated state of the polymer are the principal causes of defect quenching in the nanoparticles. The single exponential decay kinetics and high quantum yield exhibited by the polymer in good solvent, assumed to be due to the open conformation of the polymer, as well as the reduction in quantum yield and complex decay kinetics exhibited in the aggregated state of the polymer supports this notion. In order to quantify the defect density per nanoparticle, the fluorescence quantum yields of PFBT in THF and undoped CPNs were utilized to first estimate the defect quenching efficiency $\eta_d = 1-(\Phi_{THF}/\Phi_{CPN})$ which yields a quenching efficiency of ~0.79. Exciton diffusion and energy transfer simulations were performed using the same

model parameters as were used to model the dye-doped CPNs, varying the defect density until good agreement with the quenching efficiency, lifetime and ß of undoped CPNs was obtained, yielding a defect density of 2.3 defects per nanoparticle or $8.6x10^{18}$ defects per cubic centimeter of polymer.

The defect density was estimated by comparison of simulation results to experimental results as follows. It was assumed that quenching by defects occurs primarily via a combination of exciton diffusion and energy transfer, and thus quenching is greatly reduced for the polymer in good solvent, since exciton diffusion is essentially eliminated and energy transfer is greatly reduced when the polymer adopts an open conformation (due to the increased inter-chromophore distance), while the polymer in the collapsed, aggregated state possesses a relatively higher chromophore density, favoring both energy transfer and exciton diffusion. Indeed, prior work shows that even a single defect or dopant per CPN can result in substantial quenching.[13,64] The assumption of relatively little quenching for the polymer in an open, unaggregated conformation is supported by the much higher fluorescence quantum yield and single-exponential decay kinetics observed for the polymer dissolved in THF (decay kinetics are typically complex when energy transfer over a range of distances occurs). Thus a comparison between the fluorescence quantum yield and kinetics for the polymer dissolved in good solvent versus for the polymer in the nanoparticle state yields information about the extent of quenching in the nanoparticle. In order to quantify the defect density per nanoparticle, the fluorescence quantum yields of PFBT in THF and undoped CPNs were utilized to first estimate the defect quenching efficiency $\eta_d = 1-(\Phi_{THF}/\Phi_{CPN})$ which yields a quenching

efficiency of ~0.79. To estimate the defect density, we performed exciton diffusion and energy transfer simulations as described above, using the lifetime of the polymer in good solvent and assuming the same Förster radius as the dye and the same L_D parameter used to model the dye-doped CPNs. The defect density was varied until good agreement with the experimental average lifetime, β parameter, and fluorescence quantum yield of the undoped CPNs was obtained. The defect density corresponding to the best fit for the undoped nanoparticles varied depending on the L_D parameter, but for $L_D = 12$, (the global best-fit value, see below) an effective defect density of 2.3 dye equivalents per 8 nm dia. nanoparticle, or 8.6×10^{18} defects per cubic centimeter of polymer was obtained.

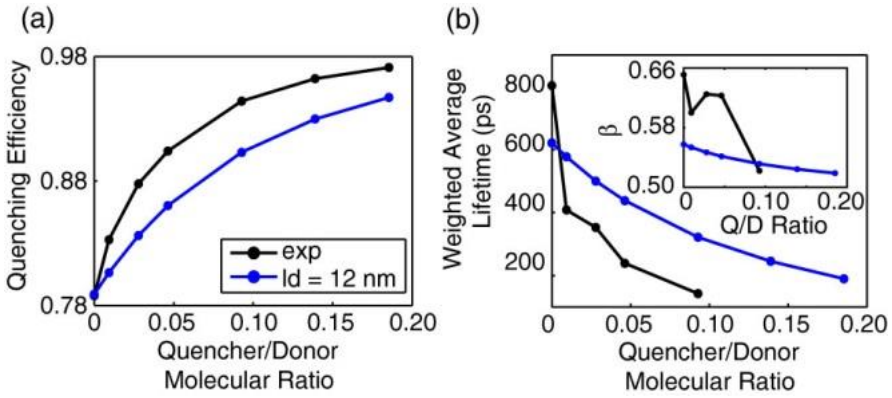

Fig. 3.5. Comparison of simulated (blue) and experimental (black) (a) quenching efficiency, (b) average lifetime, and KWW stretch parameter *ß* (inset) vs. quencher/donor molecular ratio.

To further test the model and assumptions, and to obtain the exciton diffusion length, simulations were also performed including doping with the perylene red dye, varying the exciton diffusion length to provide the best match to experimental quenching efficiencies and exciton decay kinetics. Based on the weight fraction of the dye, the average number of dyes per nanoparticle was calculated, and this was added to the number of defects determined previously. The quenching efficiencies and fluorescence decays obtained from the simulation are compared to experimental results in Fig. 3.5, for L_D = 12 nm, with the density of dye represented as a ratio of the number of dyes to the number of polymer molecules (given the molecular weights of the polymer and dye, a molecular ratio of 0.10 corresponds to a weight fraction of 1.0% or a dye density of $6x10^{18}$ dyes per cubic centimeter of polymer). By utilizing the lifetime and quenching efficiency results for the nanoparticles at various doping levels as well as for the polymer in good solvent, we are able to probe the relative contributions of exciton diffusion, energy transfer, and quenching by defects on the exciton diffusion length. Simulations neglecting quenching by defects and Poisson statistics yield a good fit to experimental quenching efficiency; however, the fits to experimental lifetimes and β are poor (c.f. Fig 3.6). By accounting for quenching by defects and Poisson statistics in the model, there is a trade-off in that the fit to experimental quenching efficiency is somewhat poorer, but the match to the lifetimes and ß is greatly improved. Nevertheless, the simulation results obtained including the Poisson distribution for defects and dyes fit reasonably well to all of the experimental results. The obtained exciton diffusion length of 12 nm is similar to that obtained for polyfluorene films by a different method.[90]

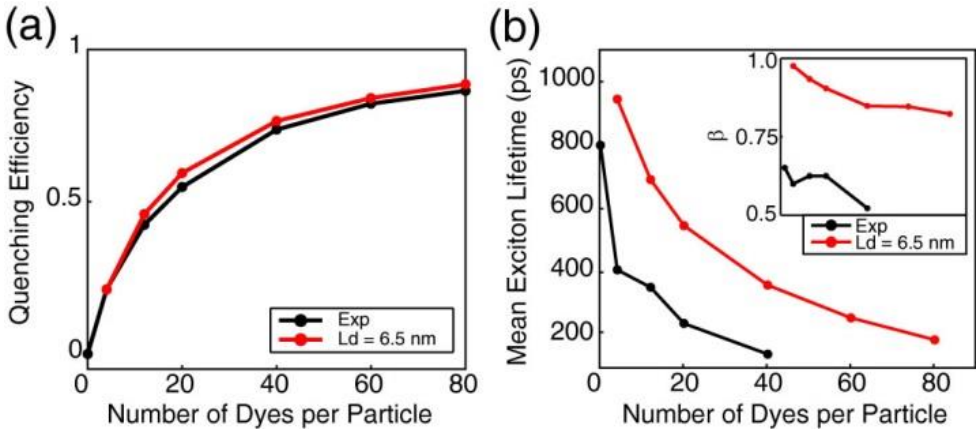

Fig. 3.6. Exciton diffusion simulation results ignoring quenching by defects and Poisson statistics. (a) Simulated (red) and experimental (black) quenching efficiency, (b) mean exciton lifetimes, and ß (inset) as a function of dyes per nanoparticle for a particle radius of 12 nm.

The Stern-Volmer analysis yields a quenching radius of 5.3 nm for perylene red--significantly higher than the Förster radius R_0, even if we make favorable assumptions regarding orientation, clearly indicating that exciton diffusion contributes significantly to the quenching efficiency of the dye. However, analysis of the quenching efficiencies alone does not clearly indicate the relative contributions of L_D and R_0: Results of exciton diffusion simulations (c.f. Fig 3.7) indicate that an increase in *either* L_D or R_0 (or both) results in an increase in quenching efficiency. While there is no simple, exact analytical formula relating L_D and R_0 to the β parameter, we found that β increases monotonically with increasing L_D, (i.e., increasing L_D results in a decrease in the amount of heterogeneity in energy transfer rates) while β decreases as R_0 increases. By including analysis of the β parameter, as well as quenching by defects, we obtained a significantly larger value for the Förster radius than that obtained using the typical assumption of $\kappa^2 = 2/3$, suggesting that this assumption may not be accurate for this system.[13] These results strongly suggest that a combined approach of measuring exciton decay kinetics, quenching efficiency, and modeling (in which quenching by defects is explicitly included) is necessary in order to disentangle the combined effects of exciton diffusion and energy transfer on exciton quenching efficiencies and dynamics.

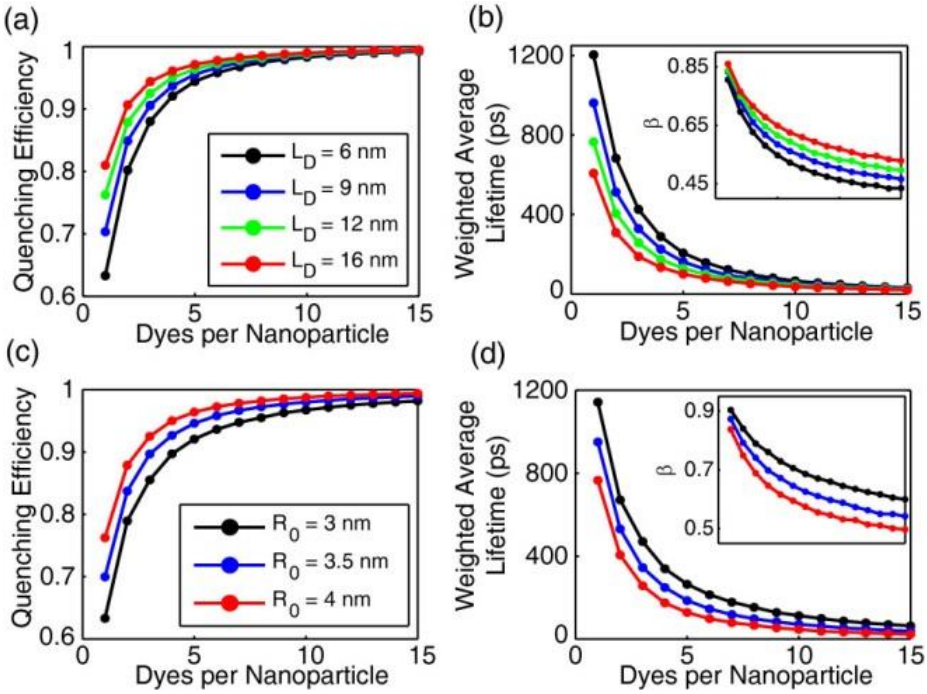

Fig. 3.7. Initial exciton diffusion simulations for a 4 nm particle radius. (a, b) Quenching efficiency, bi-exponential weighted average lifetime, and β (inset) vs. dyes per nanoparticle for L_D = 6 nm (black), 9 nm (blue), 12 nm (green), and 16 nm (red). (c, d) Quenching efficiency and bi-exponential weighted average lifetime, and ß (inset) vs. dyes per nanoparticle for R_0 = 3 nm (black), 3.5 nm (blue), and 4 nm (red).

Another important issue is the effect of quenching by defects on the determined exciton diffusion parameters, particularly the diffusion length and calculated R_0. By explicitly including quenching by defects in the simulation and analysis, we obtain an (intrinsic) exciton diffusion length (i.e., an exciton diffusion length for a hypothetical defect-free material). The intrinsic exciton diffusion length is 85% larger than the phenomenological diffusion length obtained from dye-quenching analysis without inclusion of defect quenching. This result has several implications. First, that for cases where conjugated polymers exhibit a large decrease in fluorescence quantum yield in the aggregated state (i.e., films and particles) relative to the polymer dissolved in a good solvent, this may indicate highly mobile excitons undergoing energy transfer to a small fraction of defects. Thus, somewhat paradoxically, a large value of D can result in a small observed value for the diffusion length, *which in many such cases is determined largely by the density of quenching defects rather than by the diffusion constant*. Second, the approach and results presented here suggest a general method for determining both the defect density and the effect of quenching by defects on the measured exciton diffusion length. Third, the low defect densities we obtained (much lower than 1 defect per polymer chain) and large exciton diffusion lengths determined in the absence of quenching lend qualitative support to the extraordinarily large exciton diffusion lengths reported in the single molecule studies of Barbara et al.[139] Additionally, the significantly larger exciton diffusion length obtained from the lifetime analysis is promising for applications requiring large exciton diffusion lengths, such as photovoltaic devices. Finally, while the nature of quenching defects varies from polymer to polymer, in the

case of some PPV derivatives as well as polyfluorene derivatives, quenching defects appear to be partially oxidized polymer, or hole polarons.[36,143] In the case of hole polarons, quenching by defects can sometimes be suppressed by addition of electron-donor species.[143] Thus the addition of such species could be helpful for applications requiring larger exciton diffusion lengths.

3.7 Concluding Remarks on Dye-Doped CPNs

PFBT CPNs doped with perylene red dye were found to exhibit efficient energy transfer from the polymer host to the dye. The excited state dynamics of the dye doped CPNs were studied by steady state and time-resolved fluorescence methods. The spectra are red-shifted significantly with only minor losses in fluorescence quantum yield, indicating that these nanoparticles provide bright, red emission, which is useful for some imaging and tracking applications. The lifetime of the donor exciton is reduced and the width of the distribution of exciton lifetimes was found to increase as the dopant concentration increases, as determined by time-resolved fluorescence. We interpret the kinetics results and the results of simulations as indicating substantial quenching by defects, which is amplified by exciton diffusion. The simulation parameters were adjusted until a reasonably good fit was obtained to the experimental results, including the quenching efficiency results, the average lifetimes, and the KWW stretch parameter. Based on the fitting results, an exciton diffusion length of 12 nm for PFBT CPNs was obtained, corresponding to a diffusion constant of 8.0×10^{-9} m^2 s^{-1}. The results provide some indication that quenching by defects or other quencher species is a significant but

often overlooked issue in aggregated conjugated polymers, and the approach described here--combining steady-state and time-resolved spectra of the dissolved polymer and doped nanoparticles--is proposed as a more or less general method for quantifying both exciton transport and exciton quenching by defects in conjugated polymer materials. Additionally, our analysis suggests that for some conventional approaches to determining exciton diffusion lengths, the result may be largely determined by the defect density.

3.8 PFBT/MEH-PPV Blended CPNs

There have been extensive investigations of exciton dynamics in conjugated polymer systems, including thin films,[148-150] solutions,[151,152] in a matrix,[153,154] and nanoparticles.[155] Since the structure of polymer blends (bulk heterojunctions) used in photovoltaic devices is often complex, it is desirable to gain a more complete understanding of the electronic and photophysical processes in blended conjugated polymers in order to optimize the device characteristics, as well as how such processes can be modulated through their dependence on structure and processing conditions. It has been proposed to study photophysical processes in blended conjugated polymers in the nanoparticle phase, as an alternative to thin films,[156,157] since more control of various aspects of structure and interactions can be obtained by controlling particle size, and since single nanoparticle experiments can provide a unique window into nanoscale heterogeneity effects and processes such as polaron motion.[158] Furthermore, CPNs have attracted much attention in a variety of applications, such as particle tracking,[159]

sensing,[160-162] and cellular imaging,[14,163] because of their small particle size, high fluorescent brightness and excellent photostability.[164]

Previously,[165] we found that blended PFBT/MEH-PPV CPNs exhibit unusual optical properties. In addition to the expected highly red-shifted emission due to energy transfer, we found anomalous saturation behavior characterized by an extraordinarily low excitation saturation intensity and high saturated brightness, a rare combination of properties that is optimal for saturation-based imaging methods.[166] Additionally, bulk and single nanoparticle spectroscopic experiments indicate that the blended CPNs exhibit photoswitching, which could be useful for localization-based microscopy.[167] The experimental steady-state and time-resolved spectroscopy results are given elsewhere.[102] The experimental decay kinetics and quenching efficiency results are analyzed here by comparing to a multiple energy transfer model in order to examine the physical picture of processes occurring in blended CPNs and in an attempt to obtain a clearer picture of the impact and relative importance of multiple energy transfer (energy transfer between donor chromophores) occurring within the donor (host) polymer, energy transfer between donor and acceptor, acceptor conformational effects (e.g., degree of phase separation), acceptor polydispersity, and particle size. Our analysis indicates that multiple energy transfer between donor chromophores greatly increases the effective quenching volume of the acceptor. Additionally, the high energy transfer efficiencies are consistent with a more or less open conformation of the acceptor chain, rather than a compact, phase segregated structure. The polydispersity of the acceptor polymer is found to play a role in the high degree of heterogeneity of energy transfer rates. In addition to providing results

that could be useful for tailoring the properties of CPNs for imaging applications, these results could help provide insight into the factors affecting energy transport processes in devices containing conjugated polymer blends, such as in bulk heterojunction photovoltaic devices.

3.9 Modeling Exciton Transport in Blended CPNs

We have adapted the model detailed in Section 3.6 to simulate exciton diffusion in blended conjugated polymer nanoparticles. We included defect quenching by representing defects as nonfluorescent energy acceptors with a Förster radius of 4 nm, adjusting the level of defects until the kinetics and fluorescence quantum yield were in approximate agreement with experimental results for undoped PFBT CPNs, using the approach discussed above. Since the number of defects per CPN is likely to follow a Poisson distribution, the defect density was estimated by comparison of model calculations to the CPN fluorescence quantum yield and fluorescence decay kinetics as follows. First, the initial exciton diffusion simulation is performed by varying the dye (quencher) number per particle with lifetime of PFBT in THF (3400 ps), particle radius r = 11 nm (from AFM results), exciton diffusion length L_D = 12 nm, Förster radius R_0 = 4 nm. The quenching efficiency and exciton decay kinetics for various numbers of dyes per particle are obtained from exciton diffusion simulations described above. The simulated quenching efficiency versus number of dyes per particle is shown in Figure 3.8(a). Second, the population of nanoparticles is described by an average defect density parameter (average number of defects per particle), with the fraction of particles

containing a given number of defects given by the Poisson distribution. From the distribution weights and the simulation results, a weighted average quenching efficiency is obtained, and similarly, population-averaged decay kinetics traces are obtained and fit to a bi-exponential and KWW functions to obtain the average lifetime and β parameter. The average defect density is varied until a good agreement with experimental data is obtained, yielding an average defect density of 20 dye equivalents per 22 nm diameter particle. At this average defect density, the simulated result for PFBT particle is η_d = 0.79, τ_{avg} = 750 ps, and β = 0.75. The quenching efficiency and averaged lifetime are consistent with the experimental data (η_d = 0.80, τ_{avg} = 770 ps). The slightly lower experimental KWW stretch parameter β (0.64) for the experimental data as compared to the simulated result (0.75) perhaps indicates an additional process or effect leading to broadening of the lifetime distribution.

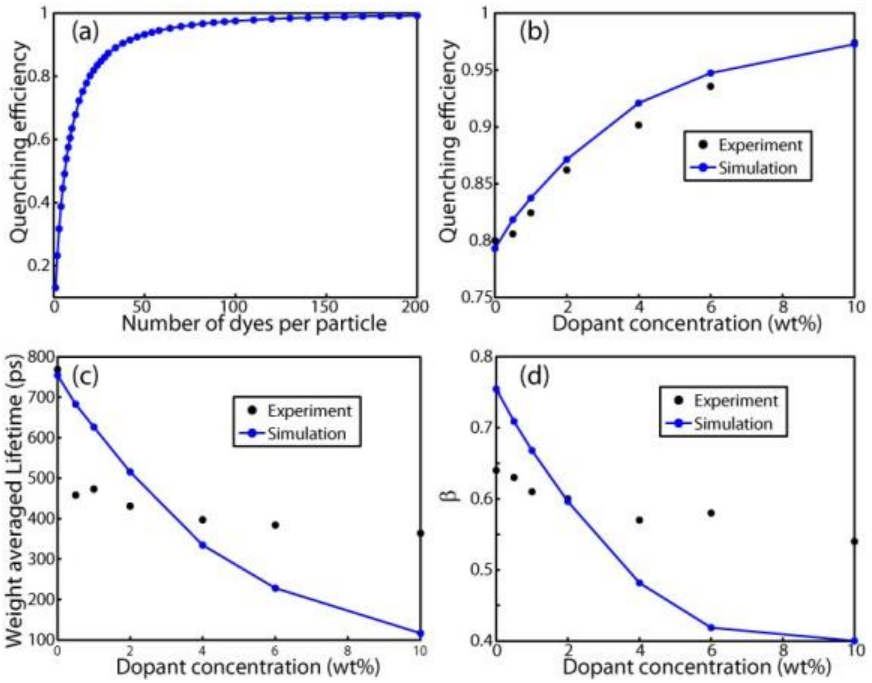

Figure 3.8. (a) Quenching efficiency of initial exciton diffusion simulations; (b, c, d) Comparison of simulated (blue dot with line) and experimental (black dot) data: (b) quenching efficiency, (c) average lifetime, and (d) KWW stretch parameter β, vs. dopant concentration (wt%).

The quenching efficiency values of the blended CPNs given in Figure 3.8(b) are given by equation, $\eta = \eta_d + (1 - \eta_d)(1 - F/F_0)$, where F_0 and F represent the nanoparticle fluorescence intensities of unblended and blended CPNs, respectively. The calculation of quenching efficiency of the polymer is obtained from the exciton diffusion and energy transfer results (Figure 3(a)) as follows. As stated above, the high quenching efficiency of MEH-PPV indicates that the molecule likely exhibits an open or extended conformation. Since the conformation or conformational distribution is not known, and for the sake of computational simplicity, we represent the extended MEH-PPV chain as isolated chromophores randomly distributed throughout the particle. This is a gross simplification that is likely to overestimate quenching efficiency, since a more realistic beads-on-a-string picture would result in correlation between chromophore positions (i.e., there will typically be 1-2 chromophores within ~1 nm of a given chromophore), resulting in overlap of quenching volumes, likely resulting in a reduced quenching efficiency. On the other hand, assuming a random distribution of chromophores places some in closer proximity than would a space-filling bead model, so there could be some cancellation of errors.

A likely more significant issue is the polydispersity of the acceptor polymer. Here we discuss how acceptor polydispersity is included in the model. Gel permeation chromatography (GPC) yields Mn = 47400, Mw = 206000, and a polydispersity index (PDI) of 4.3. For modeling purposes, we represent the polymer weight distribution as a mixture of four different polymer components with molecular weights of 3900, 10400,

104000, and 312000, and number (molecule) fractions for each component of 0.47, 0.26, 0.17 and 0.1. The molecular weight distribution of the mixture is Mn = 53400, Mw = 217000, and PDI = 4.1, close to the GPC results. The distribution of the various molecular weight polymer chains in the particles is calculated using the Poisson distribution (i.e., it is assumed that the dopant polymer chains are randomly distributed among particles) based on the weight fraction of MEH-PPV (per nanoparticle) and the population fractions for each molecular weight, using the expression $N_i = M_{NP} f_d f_i / M_i$, where N_i is the number of chains of a given component i, M_{NP} is the mass of nanoparticle, f_d is the doping fraction, f_i is the molecule fraction of component i, and M_i is the mass of component i. For a given nanoparticle containing a number of polymer chains of various molecular weights, the number of MEH-PPV chromophores is calculated based on the following reasoning. An MEH-PPV chromophore is composed of 4~8 repeat units.[168-170] If we assume that 5 repeat units is one chromophore (~1300 Daltons), then a straightforward calculation (based on the peak extinction coefficient MEH-PPV polymer mentioned earlier) yields a peak extinction coefficient per chromophore of ~4×10^5 M^{-1} cm^{-1}. We treat the chromophore size as an adjustable simulation parameter, and used a value of 5 monomer units per chromophore in the simulations. For the sake of reducing calculation complexity, we assume that each chromophore is roughly equivalent to one perylene red molecule, which in terms of the simulation means that each chromophore is represented as a point acceptor with a Förster radius of 4 nm, which is the same as the Förster radius used to represent the defects. Thus the total number of energy acceptors in

a nanoparticle is given as the sum of the number of defects and the number of MEH-PPV chromophores.

A statistical sample of CPNs, representing the distribution of defects and polymer chains is generated, and for each CPN, the total number of acceptors is calculated using the method described above. From the distribution, the population average quenching efficiencies and kinetics are calculated. The simulated population-averaged kinetics trace is fit to bi-exponential and KWW functions to obtain weighted average lifetimes, and KWW stretch parameter β, for each blending ratio, which are given in Figure 3.8(b-d). The agreement between the simulated quenching efficiency and the experimental results is good, while the lifetime and β simulated results agree reasonably well with the experimental results for much of the range of doping levels, with systematic deviations at the lower and higher doping levels. While the cause of the deviation cannot be determined conclusively, the somewhat poor agreement is not surprising given the number of simplifications and assumptions in the model. Even for the simpler case of dye-doped PFBT CPNs, the fit of lifetime and β was not particularly good.[42] Possible causes or explanations are discussed below.

First, for the case of higher doping concentration, the short lifetime and small β represent an experimental difficulty since there are likely some significant short lifetime components in the decay trace that are not resolved with the TCSPC apparatus. For example, at 10% MEH-PPV doping, there is a significant ~3 ps lifetime component when fitting the first few points of simulated population kinetics to a single exponential decay function. This short-lived component is well below the ~80 ps experimental resolution.

Short-lived components also contribute few photons to the kinetics trace, which can make them difficult to measure. Also complicating the determination of short-lived components is the fact that a small amount of scattered laser light or autofluorescence can overlap with the kinetic trace at early times.

Additional effects and processes that we have not included in the model could also affect the overall energy transfer rate and the width of the distribution of rates, such as heterogeneous or dispersive exciton transport caused by energetic heterogeneity[171] and particle-to-particle variations arising from the particle size distribution. Additionally, the acceptor chain conformation is not included in the current model. Furthermore, the current model is essentially a continuum model, and it is likely that a more granular model that explicitly includes individual donor and acceptor chromophores would yield a smaller distribution of donor-acceptor distances and thus a smaller distribution of energy transfer rates, which could improve agreement between the model and experiment. It is also possible that adjacent PFBT and MEH-PPV chromophores could result in mostly static quenching of the PFBT chromophore, which could explain the fact that the measured lifetimes appear to be less sensitive to doping concentration than predicted by the model, which assumes mostly dynamic quenching. Further development of the model for blended conjugated polymer nanoparticle is planned, including treating the polymer chain as dye/beads-on-a-string, and replacing the continuum approach with one that includes discrete donor and acceptor chromophores. Additional experiments using dopant polymers with a lower polydispersity index are planned and could also serve as a useful

test of model assumptions and the effect of polydispersity on the distribution of energy transfer rates.

3.10 Conclusions Regarding Blended CPN Dynamics

Additional insight into the nature of energy transfer processes in blended conjugated polymers was obtained from picosecond fluorescence lifetime measurements and comparison to a multiple energy transfer model. Donor exciton lifetime reduction and lifetime distribution broadening with increase of doping were determined by picosecond fluorescence lifetime measurement, indicating a broad range of energy transfer rates. Agreement between experiment and model results for quenching efficiency is very good, and the differences between the simulated lifetime and β value and the time-resolved experimental data can be explained by some of the assumptions of the model (including the assumption that dynamic quenching predominates) and the limitations of the measurement. Our results indicate that both exciton diffusion and polydispersity of acceptor are the major factors in determining the quenching efficiency and energy transfer rates in blended conjugated polymer systems. These results help provide the basis for additional studies aimed at understanding the unusual fluorescence properties of PFBT/MEH-PPV nanoparticles including anomalous saturation behavior and photoswitching. Additionally, the results shed light on the complex exciton diffusion and energy transfer processes occurring in devices that include blended polymers, such as bulk heterojunction photovoltaic devices. Furthermore, the results indicate that quenching by defects (likely polarons) could limit performance of electro-optic devices, and that

blending can, in some cases, improve performance, by providing a competitive energy transfer pathway. The results also clearly show that the conformation (e.g., extended/solvated versus collapsed chains forming nanoparticles) has a profound effect on key optical properties such as fluorescence quantum yield, likely due to increased energy transfer and exciton diffusion in the collapsed, nanoparticle conformation. The effect of the host polymer on polaron stability is also a likely factor. Finally, the results indicate the importance of measuring rates in complex systems using time-resolved methods, rather than adducing rates from steady-state measurements. For a simple system characterized by a single (dynamic) quenching rate constant k_q, the quenching efficiency is given by a simple expression such as $Q = k_q/k_{tot}$, which can be rearranged to yield the rate constant, whereas for a complex system involving multiple rates and possibly static quenching, the relationship is complex, requiring a more direct measure of the rates involved. Indeed, while the (steady-state) quenching efficiencies are reproduced quite well by the model, the distribution of energy transfer rates obtained from the model are not in agreement with the time-resolved results, clearly indicating of the importance of time-resolved measurements in this case.

CHAPTER FOUR

EFFECT OF SWELLING ON MULTIPLE ENERGY TRANSFER IN CONJUGATED POLYMER NANOPARTICLES

4.1 Introduction

Conjugated polymers (CPs) are a versatile class of semiconducting luminescent materials, used as active materials in organic photovoltaics and light-emitting diodes.[1,2,58] Conjugated polymer nanoparticles (CPNs) are well-suited to a variety of fluorescence-based imaging and sensing applications, exhibiting extraordinary figures of merit, including exceptional brightness and photostability.[17,165] Furthermore, highly efficient energy transfer to dyes or other polymers incorporated in the particle or to dyes covalently linked to the surface can provide red-shifted emission and sensors.[11,42,161,165] To tune CPN properties for various applications, we seek to better understand the species and processes that dictate their properties, and how they are modulated by polymer conformation and processing conditions.[172,173] The complex, nanoscale, multichromophoric nature of CPNs can give rise to a number of transient and persistent species interacting with the excited state including H- or J-aggregates, excimers, and exciplexes.[76,77,174] Furthermore, chemical defects, excess charges (i.e. hole polarons), and incorporated dyes can have significant effects on fluorescence properties.[13,36,64,71,90] In addition, energy transfer between like conjugated polymer chromophores (i.e., exciton diffusion) can result in a cascade of multiple energy transfer events, greatly amplifying

the effects of these species.[20,30,175] Recently, we showed that multiple energy transfer in CPNs gives rise to characteristic complex fluorescence kinetics.[42]

Here, we investigate the effects of solvent-induced swelling on the excited state dynamics in CPNs, using steady-state and time-resolved fluorescence spectroscopy to develop and test a multiple energy transfer model and thus gain a clearer picture of the interplay of the various species and processes that determine the optical properties and excited state dynamics of CPNs. We previously employed a similar approach to determine the length scale of exciton diffusion in dye-doped CPNs.[42] Particle swelling increases the inter-chromophore distance, causing a reduction in the rate of multiple energy transfer and thus a reduction in the quenching efficiency and an increase in the excited state lifetime. By fitting parameters of a multiple energy transfer model to picosecond fluorescence anisotropy decay results, we obtain an approximate picture of the characteristic length scale and time scale of energy transfer between pairs of like chromophores (homo-transfer) as well as how the energy transfer cascade is modulated by swelling. The agreement with model predictions over a broad range of swelling supports the proposed multiple energy transfer picture. The comparison of results from two different polymers suggests that higher rates of homo-transfer, which is sometimes desired (e.g., to improve exciton transport in photovoltaics, or for some sensor schemes) comes at the price of reduced fluorescence quantum yield due to increased quenching by defects, either due to the formation of additional aggregate species for systems with higher chromophore densities, or due to an increase in the energy transfer cascade to pre-existing defects. Our results point to the latter mechanism as the more likely or dominant

mechanism causing the large reduction in fluorescence quantum yield often observed for some conjugated polymer films and particles as compared to the free polymer in solution. On the basis of this picture, we suggest that in some cases, the optical properties CP films and particles can be improved by interfering with the multiple energy transfer cascade, either by competitive energy transfer or by increasing interchromophore spacing.

4.2 Additional Method Details

4.2.1 Nanoparticle Preparation

In addition to the CPN preparation and THF removal details given in Chapter 2.2, we validated the THF removal process further by assessing the batch-to-batch reproducibility of the fluorescence spectra, and fluorescence quantum yield of the aqueous nanoparticle samples. Four batches of nanoparticles were prepared using each polymer. The nanoparticle fluorescence spectra were identical in shape and peak emission wavelength for both polymers. The fluorescence quantum yield varied between 4%-6% for PFBT CPNs, and remained constant at ~1% for MEH-PPV CPNs. The aqueous samples were vacuum filtered through a glass fiber prefilter to remove larger aggregates and a 0.1 μm PVDF membrane filter (Millipore). The fraction of polymer lost in the filtration process was typically ~10%, as measured by UV-vis. The resulting suspensions are clear (not turbid) and stable for months with no visible signs of aggregation.

4.2.2 Swelling Procedure

In addition to nanoparticles in water and polymer in THF, swelled nanoparticle samples were prepared by diluting an aliquot of concentrated nanoparticle suspension with the appropriate volume of water, followed by slowly adding THF to produce 3 mL of suspensions with volume ratios of THF/water between 0.2 and 0.95. Each sample was gently agitated to ensure solution homogeneity. The sample absorbance was kept at or under ~0.05 (~0.02 for 95% THF). Samples were capped and the headspace purged with nitrogen in order to limit quenching and photobleaching by O_2 (purging was limited to ~2 minutes, in order to limit loss of THF).

4.2.3 Picosecond TCSPC and Fluorescence Anisotropy Decay

Picosecond fluorescence lifetimes and fluorescence anisotropy decay (FAD) were measured under nitrogen using a home-built setup for time-correlated single photon counting (TCSPC) spectroscopy operating in reverse mode. Frequency doubled pulses (420 nm) from a passively mode-locked Ti:Sapphire laser (Coherent Mira 900, 840 nm pulses, ~150 fs pulsewidth) were used as the excitation source for the nanoparticle samples. Fluorescence was collected perpendicular to the excitation source and passed through a 460 nm long pass filter, and a calcite Glan-Taylor polarizer (Thorlabs, GT10-A) oriented either parallel (0°), perpendicular (90°), or at magic angle (55°) with respect to the vertically polarized excitation. All three polarization angles were utilized for anisotropy decay measurements, and magic angle polarizer orientation was adopted for excited state population decay measurements. The output of a single photon avalanche photodiode (APD, id Quantique, id100-50) was used as the start timing pulse for a time-

to-amplitude converter (TAC, Canberra Model 2145), and the output of a fast PIN diode (Thorlabs, DET210) was used as the stop pulse, in a standard reverse-mode configuration.[95,119] The excitation power was attenuated (between ~300 μW and 1 mW, typ.) to maintain a count rate of ~400 kHz as measured at the APD. The analog TAC output was digitized using a multi-channel analyzer (FastComTec, MCA-3A). Before and after each measurement an instrument response function (IRF) was measured using scattered excitation light from a dilute suspension of polystyrene microspheres. The width of the IRF was determined to be ~70 ps (fwhm). Typical peak signal-to-noise ratios (SNR) for each run were between 200:1 (80%-100% THF samples) and 500:1 (IRF and low-mid % THF samples). The reported information was collated from a total of two samples per concentration of THF, and 3-5 runs per sample. Intensity decays were collected for 5-20 minutes each to obtain the above mentioned SNR values, depending on the lifetime of the sample.

4.3 Characterization of PFBT and MEH-PPV CPNs

PFBT and MEH-PPV nanoparticles were prepared via a nano-precipitation method described previously.[97] The chemical structures of PFBT and MEH-PPV are given in Fig. 1. Nanoparticle size distributions were determined via particle height analysis of several AFM images, and each histogram was constructed using >100 particles (c.f. Fig. 4.1). The mean particle sizes were 14 ± 6 nm for PFBT CPNs and 9 ± 5 nm for MEH-PPV CPNs, which are consistent with previous measurements.[165]

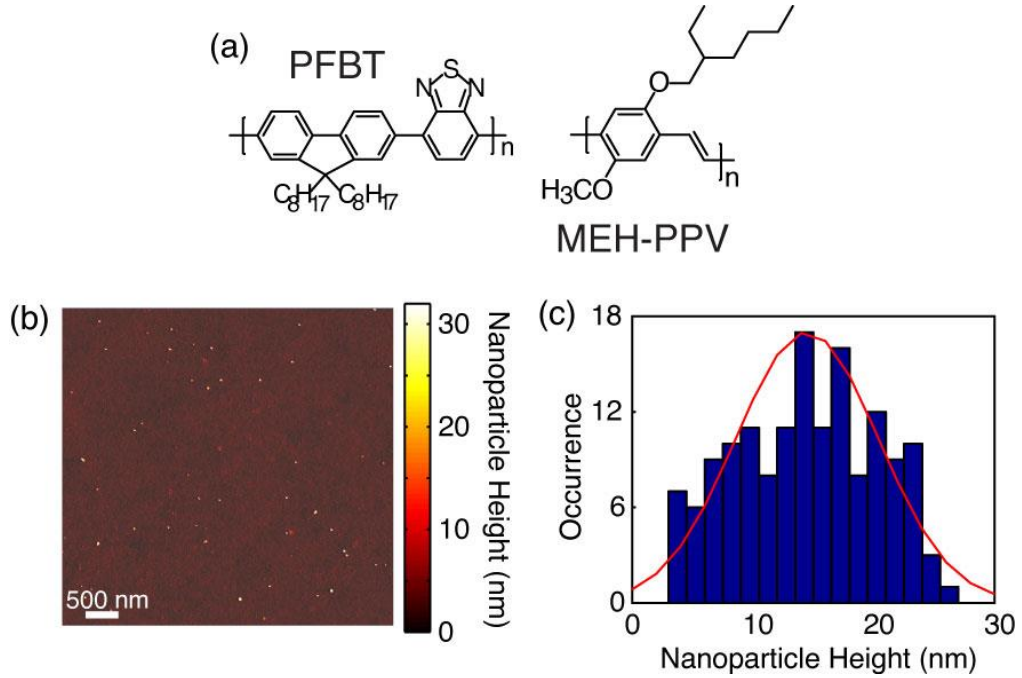

Fig. 4.1. (a) Chemical structures of PFBT and MEH-PPV. (b, c) Representative AFM image of PFBT CPNs with particle height histogram.

4.4 Effect of Solvent Composition on UV-vis and Fluorescence

The UV-Vis and fluorescence spectra of PFBT and MEH-PPV as a function of solvent composition are given in Figs. 4.2 and 4.3. The absorption spectra of PFBT maintain a similar shape with increasing THF, with a ~5 nm total blue shift, and slight broadening of the sample spectrum in 100% THF. The emission spectra show a monotonic increase in fluorescence intensity with increasing THF, and the spectra also exhibit a blue shift ~5 nm with increasing THF. The absorption spectra of MEH-PPV maintain a similar shape as THF concentration is increased, though the 95%-100% THF spectra are narrower than the spectra of the other samples. The absorption peak of MEH-PPV red shifts a total of ~15 nm from 0%-80% THF, and then blue shifts ~7 nm for the 95%-100% THF samples. The emission peak blue shifts a total of ~40 nm as THF composition is increased, and it appears that from ~40% THF to 80% THF there are possibly two phases present in solution based on the increase in intensity of the ~560 nm shoulder on the spectrum, and the reduction in intensity of the ~600 nm shoulder of the spectrum, which correspond to isolated polymer chains and aggregate species, respectively as % THF increases. An approximate isosbestic point can be seen at ~580 nm over the concentration range of ~60%-80% THF.

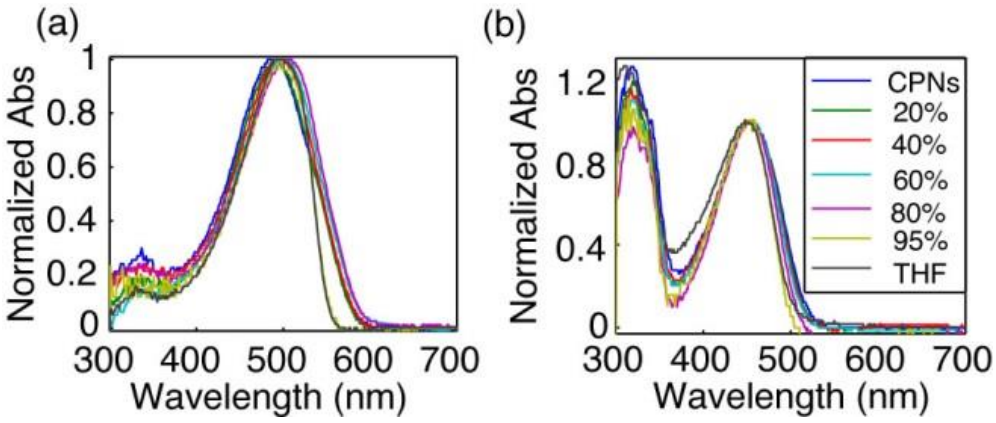

Fig. 4.2. Normalized absorption spectra of (a) MEH-PPV and (b) PFBT at varying volume % THF.

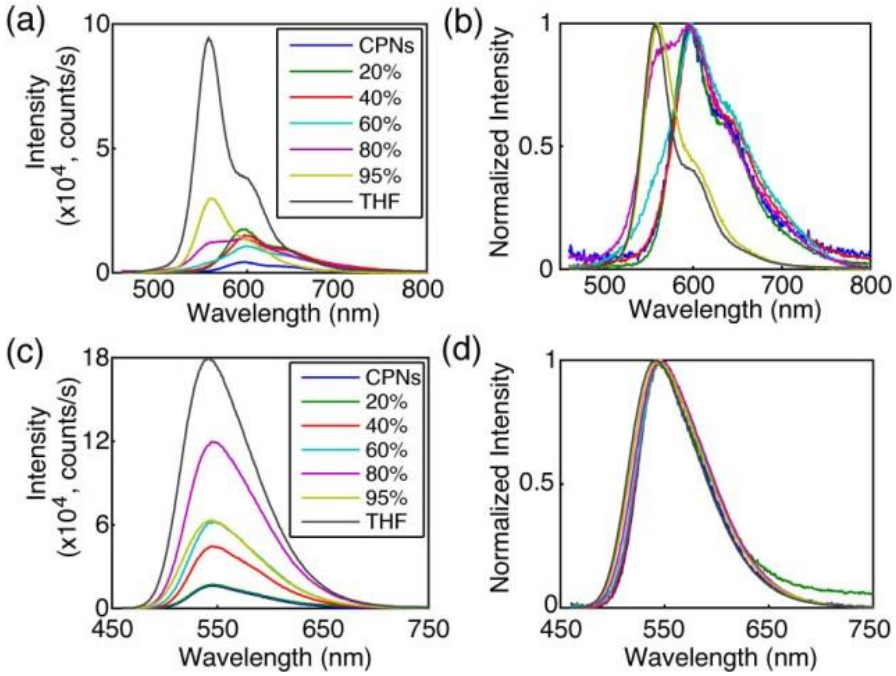

Fig. 4.3. (a, c) Absolute and (b, d) normalized emission spectra of MEH-PPV (top) and PFBT (bottom) at varying volume % THF.

The fluorescence quantum yields (Φ) are given in Fig. 4.4. The quantum yield of PFBT increases monotonically with increasing THF. However, MEH-PPV shows an initial intensity increase from 0%-20% THF, followed by the quantum yield staying relatively consistent from 20% to 80% THF, then increasing at higher % THF. The ~12% difference in quantum yield between the CPN samples in 95% THF and the dissolved polymers in THF is likely a statistical anomaly due to the uncertainty in the absorbance. While the fluorescence quantum yield remains relatively constant for MEH-PPV from 20% to 80% THF, the relative contribution of the ~600 nm shoulder decreases steadily with increasing THF concentration, likely indicating that this feature is associated with aggregate species.

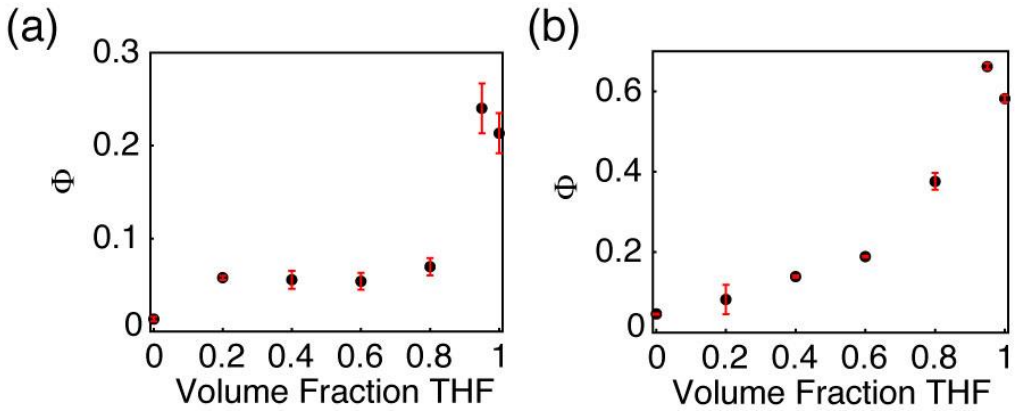

Fig. 4.4. Fluorescence quantum yield vs. THF volume fraction for (a) MEH-PPV and (b) PFBT.

One possible interpretation of the results outlined in Figs. 4.3 and 4.4 is that the coupling between transition dipoles is somewhat stronger for MEH-PPV as compared to PFBT. This is supported by the steady-state spectra, which exhibit a pronounced red-shift (in both absorption and emission) for MEH-PPV, while PFBT exhibits much smaller shifts. The lesser red shift in the absorption spectra of MEH-PPV as compared to the emission can be explained by a small fraction of highly red-shifted J-aggregate species. This is consistent with the two-state picture of Barbara, et al., used to discuss the bimodal emission properties in single molecule spectra of both PFBT and MEH-PPV. In this picture, there is a minority aggregate state that exhibits weak, red-shifted emission, and acts as an energy acceptor to the other (unaggregated) chromophores.[153,176-179] In the case of swelling, it is likely that swelling either disrupts aggregate formation, or that it reduces the rate of energy transfer to aggregate species, or both.

4.5 Picosecond Time-Resolved Fluorescence Spectroscopy

TCSPC obtained at magic angle to the excitation source was employed to measure the excited state decay kinetics of both CPN systems over the range of solvent composition. The trial functions employed during iterative convolution fitting analysis were single exponential, bi-exponential, and the Kolrausch-Williams-Watts (KWW) function or stretched exponential, given by $I(t) = A\exp(-(t/\tau)^{\beta})$, where β is the stretch parameter. Values for β are typically between ~0.3 and 1, where lower values correspond to a broader distribution of lifetimes, and $\beta = 1$ corresponds to a single exponential lifetime.[123] The fits to all three trial functions converged for all samples. With exception

of PFBT in THF, which was fit best by a single exponential, the remaining intensity decays fit poorly to a single exponential, with the residuals showing systematic deviation consistent with bi-exponential or multi-exponential dynamics. The representative intensity decays for each sample, along with the respective time constants and β versus THF volume fraction are given in Fig. 4.5. The lifetimes for both systems follow a monotonically increasing trend as THF concentration increases. The lifetimes of the CPN samples in water are shorter than previously reported (~270 ps versus ~700 ps previously for PFBT), which can be ascribed to a more complete THF removal. This explanation is also consistent with the reduced quantum yield (Φ = 0.04 versus Φ = 0.14 previously for PFBT CPNs).[42] β increases for both systems as the fraction of THF increases, beginning at ~0.3 for MEH-PPV in water and increasing monotonically to ~0.8 for MEH-PPV in THF, indicating an overall decrease in lifetime heterogeneity, though even in good solvent there is some heterogeneity. Similarly, β for PFBT increases monotonically from ~0.6 for CPNs in water to unity in THF. A substantial decrease in β is observed for PFBT from ~0.7 at 60% THF to ~0.3 at 80% THF, and is indicative of a dramatic increase in the width of the distribution of exciton lifetimes. This deviation from the trend of increasing β as % THF increases is hypothesized to be due to the presence of two distinct emitting populations with substantially different lifetimes at moderately high % THF, discussed further below. The overall trend of increasing β for both polymers is assumed to result from increases in equilibrium chromophore spacing as THF concentration increases, leading to the reduction of the rates of multiple energy transfer to quenchers. This picture is supported by prior results of dye-doped CPNs, where a reduction in β was

observed as additional quenchers (dyes) were introduced.[42] The results of the bi-exponential least-squares fitting analysis are discussed in greater detail below.

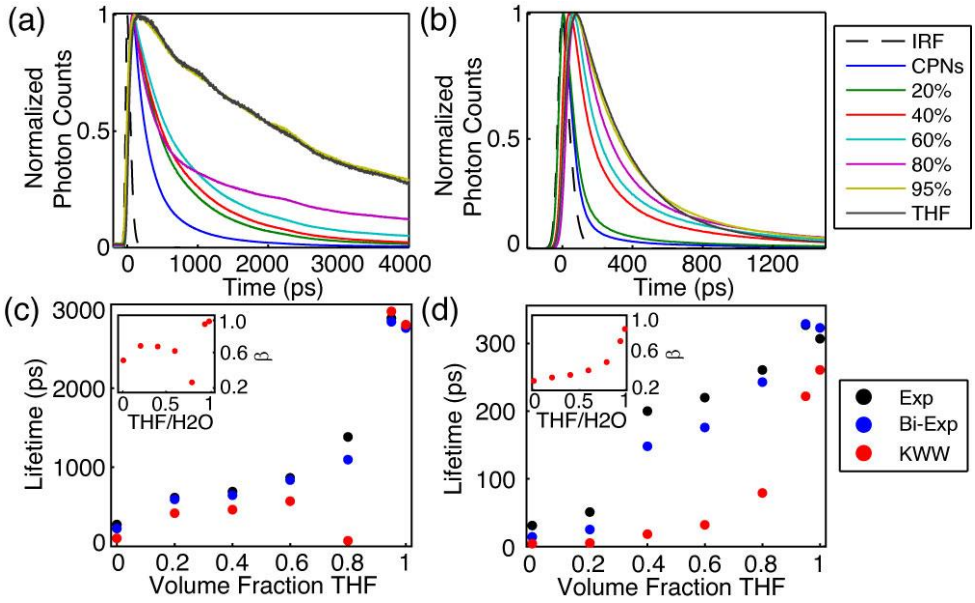

Fig. 4.5. (a, b) Normalized fluorescence intensity decays, and (c, d) lifetimes resulting from single exponential, bi-exponential weighted average, and KWW trial functions with stretch parameter β (insets) versus THF volume fraction for PFBT and MEH-PPV, respectively.

Volume Fraction THF	MEH-PPV				PFBT			
	A_1	τ_1 (ps)	A_2	τ_2 (ps)	A_1	τ_1 (ps)	A_2	τ_2 (ps)
0	0.96	9	0.04	150	0.59	88	0.41	420
0.20	0.93	14	0.07	180	0.51	260	0.49	940
0.40	0.73	56	0.27	400	0.51	280	0.49	1000
0.60	0.75	74	0.25	480	0.55	360	0.45	1400
0.80	0.75	120	0.25	620	0.65	230	0.35	2700
0.95	0.80	220	0.20	760	0.02	230	0.98	2900
1	0.95	270	0.05	1300	0.01	270	0.99	2800

Table 4.1. Summary of results of bi-exponential least-squares fitting to time-resolved fluorescence of MEH-PPV and PFBT CPNs, including weighted amplitudes (A_1, A_2) and individual exponential time constants (τ_1, τ_2).

A summary of the bi-exponential least-squares fitting results is given in Table 4.1. For MEH-PPV, the larger time constant increases monotonically with increasing THF fraction, and the weighted amplitudes do not change appreciably except for MEH-PPV in 100% THF where lifetime is characterized almost entirely by the short time constant. In contrast, the time constants remain approximately the same for PFBT between 80-100%, and the weighted amplitude corresponding to the long time constant increases from 80-100% THF. Thus, the picosecond kinetics results perhaps suggest a two state-like equilibrium, in which swelled nanoparticles and isolated polymer chains coexist in varying ratios, within a limited range of THF concentrations. This hypothesis is further

supported by the anomalously low β observed for PFBT in 80% THF and is discussed in more detail below.

Given the red-shifting of fluorescence emission in CPNs, it is assumed that chain collapse into nanoparticles leads to the formation of J-aggregate species. J-aggregation is typically accompanied by an increase in radiative rate due to an increase in the net transition dipole moment.[75,77] With this in mind, the radiative rate of a given polymer or CPN sample was calculated using the fluorescence quantum yield and fluorescence lifetime by $k_r = \Phi / \tau_{\exp}$. While the uncertainty was too high to observe a clear trend, the radiative rate varied over a factor of ~2 for PFBT (~1.2×10^8 s^{-1} to 2.5×10^8 s^{-1}) and a factor of ~4 (~3.0×10^8 s^{-1} to 1.2×10^9 s^{-1}) for MEH-PPV over the range of THF concentration, indicating that transition dipole coupling between like chromophores in the nanoparticle phase is possibly stronger in MEH-PPV as compared to PFBT.

4.6 Lattice Swelling Model

In a dense, multichromophoric system, (incoherent) exciton transport can be described as a series of energy transfer steps to roughly equivalent neighboring chromophores, terminated by a quencher (e.g. a nonfluorescent chemical defect or red-shifted, weakly fluorescent aggregate), or radiative or non-radiative relaxation to the ground electronic state. The rate of multiple energy transfer depends on the interchromophore spacing, which in the present case is determined by the amount of swelling in the CPNs (i.e. by the solvent composition). Forster's model for exciton diffusion[44] predicts that the exciton diffusion (i.e., multiple energy transfer) rate is

increased at high chromophore densities, which in the present case corresponds to low concentrations of the swelling solvent. Furthermore, in the presence of quencher species, increased exciton mobility should result in a higher quenching rate, and increased chromophore density often leads to interchain interactions that give rise to the aforementioned aggregate species. Taken together, these phenomena result in increased quenching and faster decay kinetics in aqueous CPN suspensions compared to the polymers in good solvent. To test this picture, we have employed a discrete lattice approach using a numerical random walk algorithm in order to model the effect of solvent-induced swelling on exciton quenching and decay kinetics. Similar approaches were previously utilized to model exciton diffusion and energy transfer in dye-doped nanoparticles on a discrete cubic lattice, and to model fluorescence centroid fluctuations due to polaron motion on single CPNs. [13,64] Here, we represent the particle as a cubic lattice. Each lattice point represents one chromophore, with chromophore spacing determined using the chromophore number density $C_{np} = N_{chrom}/V_{np}$, where N_{chrom} is the approximate number of chromophores per nanoparticle, and V_{np} is the particle volume. We can then determine the chromophore spacing as $\Delta x_{np} = C_{np}^{-1/3} = (V_{np}/N_{chrom})^{1/3}$. Each chromophore is assumed to consist of two monomer units, resulting in a chromophore density (for a 10 nm dia. spherical particle) of C_{np} = 1.47 chromophores/nm^3 with chromophore spacing of 0.9 nm for MEH-PPV CPNs, and C_{np} = 0.61 chromophores/nm^3 with chromophore spacing of 1.2 nm for PFBT CPNs. This is in the range typically employed for modeling exciton diffusion behavior.[180] Excitons undergo energy transfer between nearest neighbor chromophores (i.e., neighboring lattice sites), and the energy

transfer rate is set to reproduce the observed exciton diffusion length from previous work of L_D = 12 nm, which is assumed for both polymers.[42] The multiple energy transfer probability for a random walk in the absence of swelling is given by $p_{et} = 2D\Delta t / \Delta x_{np}^2$, where Δt is the time step, and D is the exciton diffusion constant given by $D = L_D^2 / 6\tau_0$, where τ_0 is the lifetime of the polymer in the absence of quenchers. We assume that the quenchers are of the "defect" variety, and do not arise from interchain interactions, thus the average number of defects per nanoparticle is taken as a constant. In neglecting the formation of interchain aggregate species as solvent quality decreases, we avoid the problems that arise from attempting to model interchain interactions in this rather complex system. Additionally, we are testing (to some degree) whether aggregate formation is required in order to explain the results, or if the results can solely be explained by changes in the rate of energy homotransfer due to swelling.

At the time of this writing, detailed information about conjugated polymer nanoparticle swelling in THF/water mixtures was not available, though results are expected as part of an ongoing collaboration. As a temporary substitute, in order to obtain only a qualitative prediction of the effect of swelling on energy homotransfer, we assume that the swelling is similar to that of polystyrene (PS) particles, which are soluble in many of the same solvents as PFBT and MEH-PPV. As such, increases in the lattice spacing were estimated using particle sizing results obtained by Carson, et al. via optical microscopy on PS beads swelled with THF.[181] A swelling factor, which accounts for increases in nanoparticle size as THF concentration increases, is determined by the ratio

of swelled and initial chromophore number densities by $f = C_s / C_{np} = V_{np} / V_s$, where C_s is the chromophore density of a swelled nanoparticle, V_{np} is the nanoparticle volume in water and V_s is the swelled nanoparticle volume. This ratio varies between 0 and 1 where f = 1 corresponds to a close-packed nanoparticle or film, and 0 represents "infinite" swelling. With the assumption that swelling decreases chromophore density (increases chromophore spacing), the swelled chromophore spacing is defined as $\Delta x_s / \Delta x_{np} = f^{-1/3}$. The model quenching efficiency and β are relatively insensitive to the initial chromophore spacing (tested using 0.8 nm and 1.5 nm lattice spacing, holding all other parameters constant), provided the homotransfer rate is adjusted to give the same exciton diffusion length, in agreement with previous results.[42] The model exciton lifetime is somewhat more sensitive to changes in lattice spacing, yielding a 20% difference in lifetime (however, assuming the homotransfer rate is scaled to reproduce L_D regardless of initial chromophore spacing, an increase in lattice spacing leads to a reduction in k_{et}, which would account for the greater differences in the model lifetime results).

The exciton diffusion theory originally developed by Förster gives a differing definition for the diffusion constant than the one defined above, given instead in terms of the chromophore density, where D is proportional to $C^{4/3}$.[44,180] Taking into account that the swelling factor f is derived from the ratio of chromophore densities, the multiple energy transfer probability p_{et} was reduced by an adjusted swelling factor of $f^{4/3} = (C_s / C_{np})^{4/3}$. Multiplying this factor by the initial energy transfer probability gives $p'_{et} = p_{et}(\Delta x_{np} / \Delta x_s)^4$. The time step size was adjusted so that prior to increasing the

interchromophore spacing, the energy transfer probability was between 1-5% per time step (though, the results are not appreciably affected by differences in time step for Δt between 1-10 ps). An integer number of quenchers are placed randomly on the lattice, each with a Förster-type quenching radius of 4 nm, similar to that of a perylene red dye molecule.[42] The mean number of quenchers per nanoparticle was treated as a fit parameter by adding quenchers until the simulated exciton lifetime approximately reproduces the lifetime of CPNs in water, similar to the approach taken previously for estimating the effect of quenching defects in dye-doped CPNs.[42] The grid spacing of the lattice was calculated for a 10x10x10 nm cubic particle, with the number of grid points given by $N_{grid} = C_{np} d_{np}^3 \approx (d_{np} / \Delta x_{np})^3$, where d_{np} is the particle diameter, resulting in 1331 grid points for MEH-PPV and 512 grid points for PFBT, in the absence of swelling. The fit procedure yielded 10 quenchers (in terms of dye equivalents) on average per NP. The greater number of quenchers per CPN than those previously reported for dye-doped PFBT CPNs (2.2 per CPN) can be ascribed to several differences, including the use of a discrete lattice model with fixed step sizes as opposed to a continuum model with random step sizes, and that a larger particle was assumed in this model. In addition, the Poisson distribution of quenchers has not been accounted for this model, which results in somewhat higher values for β (i.e., less lifetime heterogeneity) than previously reported. We neglected to include the effect of Poisson statistics on the system due to the quality of fit of the model results to the experimental results in its absence (discussed below). We have discussed the Poisson distribution of quenchers in detail in our previous work on dye-doped PFBT CPNs.[42]

At low to moderate THF concentrations, the model results match well to experimental intensity decay kinetics and quenching efficiency, the latter given by $\eta_{\exp} = 1 - (\Phi_s / \Phi_{poly})$, where Φ_s and Φ_{poly} are the fluorescence quantum yields of the sample and the polymer in THF, respectively. The simulated quenching efficiency matches the experiment well up to 60% THF for PFBT, and up to 80% THF for MEH-PPV (c.f. Fig. 4.6). The time constants obtained from the simulated intensity decays match experimental TCSPC fitting results well up to 20% THF for MEH-PPV and up to 80% THF for PFBT. With exception of CPNs in 80% THF, β is reproduced relatively well for PFBT. However, β is not reproduced very well for MEH-PPV, except for MEH-PPV in THF (c.f. Fig. 4.7). The observed divergence between simulation and experiment outside of the aforementioned solvent compositions corresponds to the regions of moderate THF composition, where it is speculated that the polymer is in dynamic equilibrium between an aggregate and free polymer state, particularly between 40%-80% THF for MEH-PPV and 80% THF for PFBT. The poor agreement with experimental β values for MEH-PPV is hypothesized to be due to the exclusion of correlated chromophore orientations and the Poisson distribution of quenchers in this model. Additionally, emission from a longer-lived aggregate state with charge transfer character or a partially oxidized species could be contributing to the complexity of the fluorescence decay.[76,182-184]

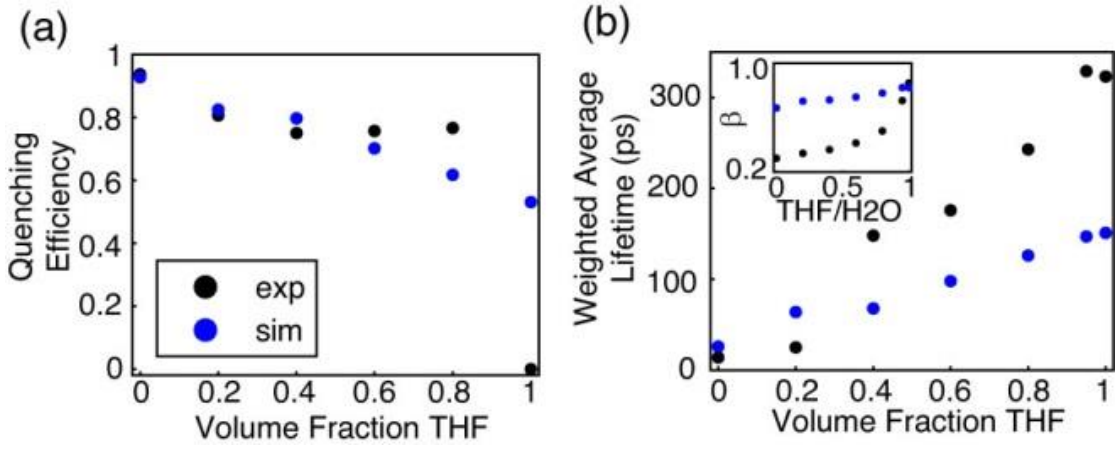

Fig. 4.6. Comparison of simulated (blue) and experimental (black) (a) quenching efficiency, (b) average lifetime, and (inset) KWW stretch parameter *ß* versus THF volume fraction for MEH-PPV.

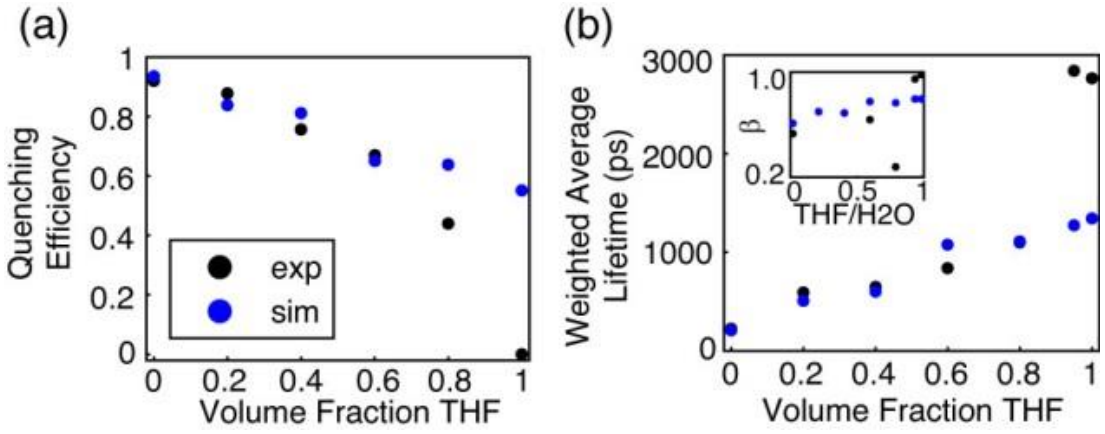

Fig. 4.7. Comparison of simulated (blue) and experimental (black) (a) quenching efficiency, (b) average lifetime, and (inset) KWW stretch parameter β versus THF volume fraction for PFBT.

In this and previous work, it has been hypothesized that the reduced quantum yield, reduced fluorescence lifetime, and heterogeneous dynamics of CPNs relative to polymer in good solvent arises from quenching by chemical defects and/or hole polarons (which may result from oxidation or photogeneration).[42] With the assumption that multiple energy transfer is a FRET-mediated process, it follows that the energy transfer efficiency to defect sites would depend upon the number of nearest neighbor chromophores, which is related to the (effective) dimensionality of the system. As an alternate perspective to the above lattice model calculations, the effect of dimensionality on quenching efficiency was investigated (using the PFBT parameters), by determining how quenching efficiency differs in isolated, one-dimensional chains of chromophores versus a 3D spherical particle.

The information for a spherical particle is taken from the above experimental and simulated data for PFBT, in which the particle is assumed to be 10 nm in diameter, with quenching efficiency ~92%. The quenching radius R_q is taken from the simulations at 4 nm. For the one dimensional case, an ensemble of linear chains is assumed, and the approximate integer number of chains per CPN (N_{chain}) is calculated from the relevant information for a spherical particle. The contour length of each chain is given by $L_{chain} = L_c N_c$, where L_c is the 1D length of one chromophore (assuming C-C bond lengths similar to benzene, yields ~2.5 nm/chromophore), and N_c is the number of chromophores per chain. A number of Poisson distributed quenchers N_q are assumed whose quenching radii do not overlap. The total quenched contour length is calculated by

$$L_q = \sum_{n=0}^{N_q} 2nR_q N_n \,, \tag{4.1}$$

where the index n corresponds to the number of quenchers, and N_n is the number of chains in the ensemble containing n quenchers, and the quenching efficiency η is calculated by

$$\eta = L_q / N_{chain} L_{chain}. \tag{4.2}$$

Equation 2 results in ~11% quenching efficiency for a one dimensional ensemble of PFBT chains, which supports the notion that even with the same quantity of quenchers in the system, quenching is greatly suppressed as the nanoparticle dissociates into free chains in solution. This also supports one assumption of our quenching picture for CPNs: that quenching by defects is greatly reduced in isolated, extended chains due to a drastic reduction in the rate of multiple energy transfer, which stems largely from the reduced number of nearest neighbor chromophores available for energy transfer in the 1D case, compared to the 3D case (two neighbors in 1D, versus six neighbors in 3D). This is reflected in the model results, as Förster exciton diffusion theory predicts the reduction of the energy homotransfer rate by an order of magnitude at the highest concentrations of swelling solvent. However, as is shown by the divergence of the model quenching efficiency and decay kinetics to the experimental results at high swelling solvent ratios, even an order of magnitude reduction in the rate of energy transfer is insufficient to accurately model the reduction in quenching efficiency and fluorescence decay rates for high THF ratios. Our proposed picture is further supported by previous modeling of linear polyenes by Beljonne et al., which shows that interchain exciton coupling weakens

with increasing intermolecular separation, and as the chain length becomes larger than the intermolecular separation. In addition, it was shown that the magnitude of the intrachain transition dipole is increased with increasing chain length.[185] Thus, as a particle swells and collapsed chains unfold, the excitonic coupling to interchain nearest neighbors is decreased, disfavoring 2D or 3D exciton transport, and the coupling to intrachain nearest neighbors increases, which favors 1D exciton transport.

Throughout these experiments, there have been several results which suggest that solvent-induced swelling can result in a two-state system at moderate THF concentrations. Bi-exponential lifetime analysis results for both polymers at moderate THF concentrations yield short time constants similar to the CPNs in water, and long time constants similar to the free polymer in THF. These time constants hold fixed for PFBT from 80% to 95% THF, only shifting in the weighted amplitudes of each (c.f. Table 1). The model results also significantly deviate from what is observed experimentally in the region of THF concentration where these phenomena are observed, which suggests that the lattice swelling picture alone is insufficient to describe the physics of the CPNs for moderate to high THF compositions, and it is likely that incorporating nanoparticle dissociation would result in better agreement. Additionally, the observed quenching of the polymer fluorescence in the aqueous solution can be ascribed to an increased rate of homotransfer from a majority of highly fluorescent, higher energy chromophores to a weakly fluorescent, red-shifted minority of aggregates that act as energy acceptors for both PFBT and MEH-PPV.[177-179] Additionally, steady-state fluorescence results show the red-shifted spectral signatures of the nanoparticle

phase in addition to the free (unassociated) polymer spectrum in moderately swelled MEH-PPV samples (Given the large molecular weight of MEH-PPV used, there are several possible dynamic equilibria that might exist at moderate THF ratios, such as dynamic intrachain aggregation and separation in a single unassociated chain, and/or dynamic re-association of an unassociated chain with a swelled nanoparticle). While it is beyond the scope of this article to determine whether the system is indeed in a two-phase system, for now, it can only be speculated that perhaps the system exists as both isolated polymer chains and swelled nanoparticles coexisting in equilibrium, only within a fairly narrow range of THF concentrations.

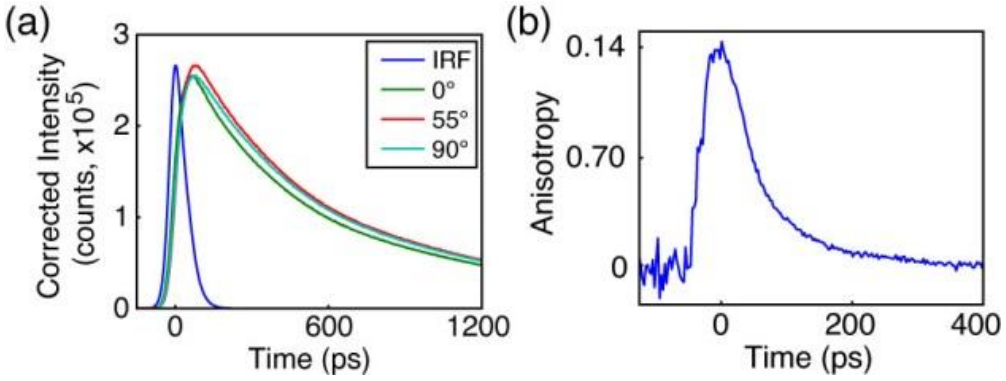

Fig. 4.8. Anisotropy data for PFBT in 40% THF. (a) Intensity decays collected at 0° (green), 55° (red), and 90° (cyan) polarizer orientations with sample IRF (blue). (b) Anisotropy decay $R(t)$ constructed from intensity data in (a).

4.7 Picosecond Fluorescence Anisotropy Decay (FAD)

Time-resolved anisotropy measurements provide a means to probe energy homo-transfer rates in CPNs, given the assumption that each energy transfer event prior to radiative decay slightly alters the polarization state of the exciton, leading to depolarization of the observed fluorescence photons. Fluorescence intensity decays collected at 0°, 90°, and 55° polarizer orientations relative to the vertically polarized excitation pulse were obtained via TCSPC (c.f. Fig. 4.8a). The resulting intensity decays were utilized to construct time-resolved anisotropy decays by the relation $R(t) = D(t)/S(t)$, where $D(t) = I_0(t) - GI_{90}(t)$, $S(t) = I_0(t) + 2GI_{90}(t) \approx 3I_{55}(t)$. The process by which the anisotropy data is calculated from the fluorescence intensity decays at each polarizer orientation was adapted from a method by Fleming et al. and is described below.[95] First, $S(t)$ is determined from fitting the 55° data. The trial functions are single exponential for fluorescein in water and PFBT in THF, and KWW for all other samples. The parameters yielded from these fits ($\tau_{\exp}^{55}$, or τ_{KWW}^{55}, β) are then held constant and used as the first term of the trial decay for the 0° and 90° data. The second term in the trial decay function for the parallel (or perpendicular) data is given by a single exponential, so that the total trial decay function for a given sample is either a bi-exponential or a summed KWW and exponential decay of the form

$$I_0(t) = A_{KWW}^0 \exp(-(t/\tau_{KWW}^{55})^{\beta}) + A_{\exp}^0 \exp(-t/\tau_{\exp}^0), \qquad (4.3)$$

where the superscripts indicate polarizer orientations and the subscripts indicate the decay function (with analogous results for the 90° polarizer orientation). To account for

differences in signal-to-noise ratio between runs, an amplitude correction factor is calculated by

$$A_{\exp}^{0*} = \left(A_{KWW}^{55} / A_{KWW}^{0}\right) A_{\exp}^{0}, \tag{4.4}$$

where the asterisk indicates the corrected amplitude, A_{KWW}^{55} is taken from the 55° fit results, and A_{KWW}^{0} and $A_{\exp}^{0}$ are taken from Equation 4.3. The correlation time τ_c is determined from a weighted average of the individual exponential time constants obtained from the corresponding fits to the intensity decays at 0° and 90° polarizer orientations by

$$\tau_c = \frac{|A_{\exp}^{0*}|}{|A_{\exp}^{0*}| + |A_{\exp}^{90*}|}\tau_{\exp}^{0} + \frac{|A_{\exp}^{90*}|}{|A_{\exp}^{0*}| + |A_{\exp}^{90*}|}\tau_{\exp}^{90}. \tag{4.5}$$

To calculate the anisotropy decay, the 55° terms drop out in the numerator due to the subtraction of $I_0(t)$ and $I_{90}(t)$, yielding

$$r(t) = \frac{I_0(t) - I_{90}(t)}{3I_{55}(t)} = \frac{(A_{\exp}^{0*} - A_{\exp}^{90*})\exp(-t/\tau_c)}{3A_{KWW}^{55}\exp(-(t/\tau_{KWW}^{55})^{\beta})}. \tag{4.6}$$

Evaluating Equation 4.6 at $t = 0$ yields the limiting anisotropy r_0,

$$r(t=0) = r_0 = \frac{A_{\exp}^{0*} - A_{\exp}^{90*}}{3A_{KWW}^{55}}. \tag{4.7}$$

Due to the short lifetime and rapid anisotropy decay for MEH-PPV, only MEH-PPV in solution yielded a complete set of intensity decays usable for fitting analysis (r_0 = 0.07 τ_c = 290 ps). The correlation time calculated from the fitting analysis does approximately match typical correlation times reported previously for MEH-PPV in

solution.[174,186] The representative intensity decays and constructed anisotropy decay $R(t)$ for moderately swelled PFBT CPNs (40% THF) are given in Fig. 8. For 40%, 60%, 95% and 100% THF, the r_0 values calculated from the fitting analysis procedure are 0.18, 0.08, 0.07 and 0.09, and the phenomenological correlation times, are 21 ps, 450 ps, 910 ps, and 920 ps, respectively. Convolution fitting (using the constructed anisotropy decay and IRF at magic angle) of the anisotropy decay in Fig 8b to a single exponential yields an r_0 of 0.14 and τ_c of 60 ps, which are reasonably close to the fitting analysis results above. The differences in r_0 and τ_c resulting from convolution fitting of $R(t)$ arise from the fact that the anisotropy decay in the absence of convolution distortion is not determined accurately by convolution fitting of $R(t)$, unless τ_c is much greater than the duration of the IRF.[95] The increasing correlation times indicate that the anisotropy decays at a reduced rate with increasing % THF. The reduced rate of anisotropy decay with increased swelling is expected due to a reduced rate of multiple energy transfer resulting from increases in equilibrium interchromophore distance. The low (~2x to ~50x lower than the theoretical maximum of 0.4) values of r_0 obtained from fitting analysis for both polymers suggest that either the absorption and emission transition dipoles are not parallel to one another, or that the time window we are able to observe is after some depolarization has already occurred. For CPNs, the correlation time constants obtained with Eq. 3 are hypothesized to represent the depolarization time due to multiple energy transfer exclusively (i.e., particle rotation in solvent can be safely ignored), providing a convenient means to probe the rate of exciton transport at each solvent composition. For PFBT CPNs in 40% THF (given that a more significant anisotropy decay is observed for

this sample), τ_c from the fitting analysis is 21 ps, which corresponds to a multiple energy transfer rate constant k_{et} of 4.8×10^{10} s^{-1}. Compared to the free PFBT polymer in THF, with τ_c ~900 ps, this corresponds to k_{et} = 1.1×10^{9} s^{-1}, which suggests that multiple energy transfer between equivalent chromophores is faster in the partially swelled particle state.

Given that the model kinetics match experimental decay kinetics well at low THF concentrations, the approximate k_{et} for CPNs in water was calculated from the model energy transfer probabilities by $p_{et} = 1-\exp(-k_{et}\Delta t)$. The results of these calculations yield model rate constants of 2.0×10^{11} s^{-1} for MEH-PPV CPNs and 1.1×10^{10} s^{-1} for PFBT CPNs. The experimental k_{et} values for the polymers in good solvent were 3.4×10^{9} s^{-1} for MEH-PPV and 1.1×10^{9} s^{-1} for PFBT. This indicates that the energy transfer rate to six nearest neighbors (for the nanoparticles) is between ~10x and ~60x faster than the energy transfer rate to two nearest neighbors (for a linear polymer chain in solution).

Upon examination of the experimental and model energy transfer kinetics for both polymers, it can be inferred that differences in multiple energy transfer rates have a significant impact on the related physical observables (fluorescence lifetime, fluorescence quantum yield, etc.) that impact device and imaging applications for a given polymer. The steady-state spectra for both polymers suggest that perhaps there is greater transition dipole coupling in MEH-PPV, implying that excitons are delocalized to a greater extent in MEH-PPV compared to PFBT, which provides a partial explanation for the increased rates of exciton transport seen in the model and FAD results for MEH-PPV. Given that the model results yield approximately the same number of quenchers per unit volume for

both polymers, it follows that if exciton transport is faster, then excitons would be more efficiently funneled to defect sites, which would help to explain the reduced fluorescence lifetime and quantum yield in MEH-PPV compared to PFBT. Therefore, it follows that polymers with higher exciton mobility would be well-suited for devices requiring fast transport (e.g. bulk heterojunction photovoltaics, since excitons would be more efficiently funneled to the heterojunction to undergo charge transfer). Following the hypothesis that higher transport rates increase quenching by defects, increased mobility would also suggest more efficient FRET to dopants, which might increase the overall luminescence yield in MEH-PPV CPNs for imaging applications (despite PFBT CPNs having intrinsically higher quantum yield, which would make PFBT ideal for applications requiring higher fluorescence quantum yield, such as OLED device applications or fluorescence imaging applications).

Additionally, we seek to address the question of whether "interchain aggregates" are required to explain the differences between the optical properties of CP in solution versus in films and particles. While in some cases, there is some evidence for possible interchain aggregate species (for example, the highly red-shifted emission of MEH-PPV films and particles), the decay kinetics of the fluorescent excited state as well as the FAD results of CPNs with varying degrees of swelling are roughly consistent with model results that do not include formation of weakly-fluorescent aggregates. This model is based on a picture in which the number of quenching defects in a particle is not dependent on the degree of swelling (e.g., oxidized defects), and that the effective number of chromophores quenched per defect increases as the chromophore density

increases, due to the highly sensitive dependence of exciton diffusion length on interchromophore spacing. While this work does not rule out any increased quenching effect due to interchain aggregate species, it does lend some support to an alternative mechanism that could explain the differences between the spectroscopic properties of conjugated polymers in solution as compared to films or particles.

4.8 Conclusion

Steady-state and time-resolved fluorescence spectroscopic methods, in conjunction with a discrete lattice model were utilized to assess how decreasing chromophore density (resulting from solvent-induced swelling) alters the steady-state spectra, exciton decay rates, and multiple energy transfer rates in PFBT and MEH-PPV CPNs. For both polymers, the fluorescence quantum yield and lifetime increases with increasing THF concentration, reproducing the results for the free polymer at 95% THF, indicating that fluorescence quenching in CPNs is completely reversible through swelling. Analysis of the exciton decay kinetics for both polymers in addition to the fluorescence spectra of MEH-PPV indicates a possible dynamic equilibrium between aggregated and unassociated polymer at moderate THF ratios. A multiple energy transfer model incorporating quenching by defects yielded good agreement with experimental quenching efficiency and TCSPC results at low to moderate THF concentrations, which confirms the physical picture of reduced energy transfer to oxidized defects (ignoring interchain aggregation) with decreases in chromophore density. The model results yielded energy transfer rate constants over an order of magnitude higher for PFBT and

MEH-PPV CPNs compared to the experimental values of k_{et} obtained via FAD for the corresponding polymers in THF, which explains the increased defect quenching for closely-packed chromophores. Calculations assessing how the dimensionality of energy transport affects exciton quenching by defects yield nearly an order of magnitude difference in quenching, indicating that quenching by oxidized defects is greatly suppressed in an ensemble of linear 1D chains compared to a 3D nanoparticle, which is supported by the adapted Förster theory in our model. The increased multiple energy transfer rate in MEH-PPV compared to PFBT elucidates an apparent tradeoff between exciton mobility and luminescence yield, which may be exploited for device and imaging applications. The results are consistent with an effective chromophore diameter of ~1 nm and an energy transfer time of ~5 ps to ~90 ps between neighboring close-packed chromophores.

CHAPTER FIVE

CONCLUSIONS AND FUTURE DIRECTIONS

5.1 A Systematic Investigation of Exciton Transport in CPNs

Throughout the experiments detailed in this dissertation, it has been our aim to systematically address several relevant questions regarding exciton transport in dense, nanoscale, multichromophoric systems such as CPNs. Given that defects are often unavoidable in aggregated polymer systems, it has been valuable to understand the role of defects and their effect on determining the exciton diffusion length for a given polymer. This was addressed by dye-doping and polymer blending to deliberately introduce quenchers into CPNs with known amounts of defect quenching. This strategy elucidated how ignoring defect quenchers can result in substantial underestimation of the exciton diffusion length in the absence of quenchers. For both doped systems, Monte Carlo simulations of exciton transport and energy transfer to a Possion distributed ensemble of defects and dopants were utilized to model the observed exciton decay kinetics from experimental fluorescence lifetime measurements, which in turn, led to the determination of the exciton diffusion length for PFBT in the absence of defects. In addition, modeling of polymer blended CPNs aided in determining that a dopant polymer is more likely to be in an open conformation when doped in an aggregate nanoparticle (rather than a more compact conformation) due to the high energy transfer efficiency from PFBT to the dopant polymer MEH-PPV. After determining the typical length scale of exciton transport in CPNs, the next problem was to determine how exciton transport rates are

affected by changes in interchromophore spacing, and to additionally determine how the effective dimensionality of exciton transport in CPNs affects defect quenching. This was accomplished using solvent-induced swelling methods. In addition to fluorescence lifetime measurements, fluorescence anisotropy decay measurements allowed for the calculation of exciton transport rates (for moderate to high THF concentrations). Additionally, a discrete lattice model that included changes in lattice spacing (i.e., interchromophore spacing) was utilized to model the effect of swelling on exciton transport rates and to determine effective chromophore size in PFBT and MEH-PPV CPNs (~1 nm), with good agreement between experimental and model results at low-to-moderate THF concentrations. It is clear by the results of this work that an apparent compromise between fluorescence quantum yield and the rate of exciton transport exists, which can be taken advantage of in different ways depending on the desired applications for a given conjugated polymer system.

5.2 Determination of the Intrinsic Exciton Diffusion Length in PFBT

A novel approach was proposed for determining exciton transport parameters in conjugated polymers. Exciton dynamics of conjugated polymer nanoparticles doped with dyes were investigated by time-resolved fluorescence spectroscopy. Highly efficient energy transfer from the polymer PFBT to the dye perylene red was evident in the fluorescence spectra and excited state kinetics. Exciton transport parameters were obtained by fitting to a model that included the effects of Poisson statistics, nanoparticle size, exciton diffusion, energy transfer, and quenching by defects. The results indicate

substantial quenching by defects, owing primarily to exciton diffusion, which can greatly increase the effective quenching volume of defects. Stern-Volmer quenching analysis of dye-doped CPNs yields a quenching constant of 37 per dye molecule, which corresponds to a perylene red quenching radius of 5.3 nm. The substantially higher quenching radius obtained from Stern-Volmer analysis as compared to the calculated quenching radius of 3 nm for the PFBT/perylene red pair supports the notion of exciton diffusion contributing to the observed quenching efficiency. We estimated the amount of quenching by defects, and included quenching by defects in our model and analysis, yielding an estimated exciton diffusion length of 12 nm and diffusion constant of 8.0×10^{-9} m^2 s^{-1} for nanoparticles of PFBT. The results indicate that quenching by defects can lead to substantial error in determined exciton transport parameters (i.e., underestimation of L_D by a factor of ~2), unless quenching by defects is properly taken into account in the analysis. The larger exciton diffusion length determined from the above analysis is promising for device applications requiring large exciton diffusion lengths, such as organic photovoltaic devices. Given that the analysis above results in an exciton diffusion length for a hypothetical defect-free material, for the aforementioned applications, strategies would need to be employed to reduce the contribution of defects to exciton transport (e.g. swelling methods to break up aggregate defects, or doping with reducing agents to minimize hole polaron quenchers). Additionally, the above analysis provides a general means for determining the defect density and exciton diffusion length (as well as the effect of defect quenchers on the measured L_D) for materials that exhibit substantial fluorescence quenching in the aggregated state.

5.3 Investigating Exciton Transport Rates in CPNs Through Swelling

Many key processes in conjugated polymers are strongly influenced by multiple energy transfer (i.e., exciton diffusion). We investigated the effect of solvent-induced swelling on the kinetics of multiple energy transfer in nanoparticles of the conjugated polymers PFBT and MEH-PPV. Multiple incoherent energy transfer events between equivalent chromophores results in loss of fluorescence polarization, which can be observed in the fluorescence anisotropy decay kinetics. Additionally, multiple energy transfer affects the rate of quenching by defects. We found that the rate of energy transfer between like chromophores is highly sensitive to solvent effects, occurring at a rate of 1.1×10^9 s^{-1} for PFBT dissolved in THF, and 3.3×10^9 s^{-1} for MEH-PPV dissolved in THF. In both moderately swelled and aqueous nanoparticle suspsensions of PFBT and MEH-PPV, the rate of energy transfer is increased by a factor of 10-60 (with the highest energy transfer rates corresponding to MEH-PPV CPNs). A discrete cubic lattice model incorporating distance-dependent multiple energy transfer and quenching by defects was employed to elucidate the relationships between solvent-induced swelling, fluorescence quantum yield, and decay kinetics. The simulation results show good agreement with experimental results at low to moderate THF concentrations. The results support quenching by defects or polarons, amplified by multiple energy transfer, as a likely explanation for the typically low fluorescence quantum yield of conjugated polymer particles as compared to the free polymer in solution as well as similar effects observed in thin films. In addition, the effect of dimensionality on fluorescence quenching by

defects was determined by comparing a 3D spherical particle to an ensemble of 1D linear polymer chains with equivalent amounts of chromophores and defects. It was calculated that defect quenching is substantially reduced by ~80% in the 1D ensemble compared to a 3D particle, indicating that interchain exciton transport (or intrachain transport in folded chains) contributes substantially to quenching by defects.

5.4 Future Prospects

There are several directions that have already been pursued or are currently being pursued to study CPNs further. It is beneficial to understand the details of charge-transfer complex formation, recombination, and transport in CPNs (i.e., polaron formation and polaron diffusion). Single molecule microscopy has been done previously to examine charge carrier transport in CPNs, but was restricted in the observable time scale (50 frames/s).[64,73] The previous results suggested that polaron dynamics were occurring at rates below the time resolution of the instrument. Work is currently being pursued to examine polaron transport on the sub-millisecond time scale, in an effort to better understand the rates of charge-transfer complex formation and recombination in CPNs, which are crucial to effective device performance.

Additionally, we may examine the effect of chain length on exciton dynamics and transport rates by investigating nanoscale oligomer aggregates via steady-state and time resolved spectroscopic methods. Some work has already been done on oligophenylene-vinylene (OPV) and oligothiophene (OT) nano-aggregates by Spano, which suggests somewhat different excitonic behavior in the aggregated state. In particular, conjugated

oligomer aggregates seem to blue-shift (i.e., form H-aggregates) as opposed to the common red-shifting (J-aggregation) seen in conjugated polymer aggregates.[187] However, it is also possible to form oligomer aggregates which display J-aggregate characteristics, [188] which would make oligomer nanoparticles of other monomer structures (e.g. oligofluorenes or oligo-FBTs) worth studying. For example, it could be of interest to determine at which chain length J-aggregation dominates over H-aggregation (and/or if mixed aggregation is observed). Another useful aspect to H-aggregation is that lifetimes are usually longer, which could lead to longer exciton transport due to the extended lifetime of the H-aggregate state, which could be probed using methods we have already employed using CPN samples.

REFERENCES

(1) Dennler, G., and Sariciftci, N. S. Flexible Conjugated Polymer-Based Plastic Solar Cells: From Basics to Applications. *Proc. IEEE* **2005**, *93*, 1429-1439.

(2) Yim, K. H., Zheng, Z., Liang, Z., Friend, R. H., Huck, W. T. S., and Kim, J. S. Efficient Conjugated-Polymer Optoelectronic Devices Fabricated by Thin-Film Transfer-Printing Technique. *Adv. Funct. Mater.* **2008**, *18*, 1012-1019.

(3) McNeill, J. D.; O'Connor, D. B.; Barbara, P. F. Imaging Organic Device Function with Near-Field Scanning Optical Microscopy. *J. Chem. Phys.* **2000**, *112*, 7811-7821.

(4) Rothe, C.; King, S. M.; Monkman, A. P. Direct measurement of the singlet generation yield in polymer light-emitting diodes. *Phys. Rev. Lett.* **2006**, *97*.

(5) Greenham, N. C.; Samuel, I. D. W.; Hayes, G. R.; Phillips, R. T.; Kessener, Y. A. R. R.; Moratti, S. C.; Holmes, A. B.; Friend, R. H. Measurement of Absolute Photoluminescence Quantum Efficiencies in Conjugated Polymers *Chem. Phys. Lett.* **1995**, *241*, 89-96.

(6) Pei, Q.; Yang, Y. Efficient Photoluminescence and Electroluminescence from a Soluble Polyfluorene. *J. Am. Chem. Soc.* **1996**, *118*, 7416-7417.

(7) McNeill, J. D.; Barbara, P. F. NSOM Investigation of Carrier Generation, Recombination, and Drift in a Conjugated Polymer. *J. Phys. Chem. B.* **2002**, *106*, 4632-4639.

(8) Lunt, R. R., Giebink, N. C., Belak, A. A., Benzinger, J. B., and Forrest, S. R. Exciton Diffusion Lengths of Organic Semiconductor Thin Films Measured by Spectrally Resolved Photoluminescence Quenching. *J. Appl. Phys.* **2009**, *105*, 053711-053717.

(9) Heeger, A. J. Nobel Lecture: Semiconducting and Metallic Polymers: the Fourth Generation of Polymeric Materials. *Rev. Mod. Phys.* **2001**, *73*, 681-700.

(10) Meier, H.; Stalmach, U.; Kolshorn, H. Effective Conjugation Length and UV/vis Spectra of Oligomers. *Acta Polym.* **1997**, *48*, 379-384.

(11) Wu, C. F., Peng, H., Jiang, Y. and McNeill, J. Energy Transfer Mediated Fluorescence from Blended Conjugated Polymer Nanoparticles. *J. Phys. Chem. B.* **2006**, *110*, 14148-14154.

(12) Ntziachristos, V. Fluorescence Molecular Imaging. *Annu. Rev. Biomed. Eng.* **2006**, *8*, 1-33.

(13) Wu, C. F., Zheng, Y. L., Szymanski, C., and McNeill, J. Energy Transfer in a Nanoscale Multichromophoric System: Fluorescent Dye-Doped Conjugated Polymer Nanoparticles. *J. Phys. Chem. C* **2008**, *112*, 1772-1781.

(14) Wu, C. F.; Schneider, T.; Zeigler, M.; Yu, J. B.; Schiro, P. G.; Burnham, D. R.; McNeill, J. D.; Chiu, D. T. Bioconjugation of Ultrabright Semiconducting Polymer Dots for Specific Cellular Targeting. *J. Am. Chem. Soc.* **2010**, *132*, 15410-15417.

(15) Wu, C. F.; Szymanski, C.; McNeill, J. Preparation and encapsulation of highly fluorescent conjugated polymer nanoparticles. *Langmuir* **2006**, *22*, 2956-2960.

(16) Tian, Z., Yu, J., Wu, C. F., Szymanski, C. and McNeill, J. Amplified Energy Transfer in Conjugated Polymer Nanoparticle Tags and Sensors. *Nanoscale* **2010**, *2*, 1999-2011.

(17) Wu, C. F.; Bull, B.; Szymanski, C.; Christensen, K.; McNeill, J. Multicolor Conjugated Polymer Dots for Biological Fluorescence Imaging. *ACS Nano* **2008**, *2*, 2415-2423.

(18) Johansson, L. B. Å.; Langhals, H. Spectroscopic Studies of Fluorescent Perylene Dyes. *Spectrochimica Acta Part A* **1991**, *47*, 857-861.

(19) Frenkel, J. On the Transformation of Light into Heat in Solids. II. *Phys. Rev.* **1931**, *37*, 1276-1294.

(20) Kasha, M. Energy Transfer Mechanisms and the Molecular Exciton Model for Molecular Aggregates. *Rad. Res.* **1963**, *20*, 55-70.

(21) Silinsh, E. A.; Capek, V. *Organic Molecular Crystals: Interaction, Localization, and Transport Phenomena*; First ed.; American Institute of Physics, 1997.

(22) Pope, M.; Swenberg, C. E. *Electronic Processes in Organic Crystals and Polymers*; Second ed.; Oxford University Press, 1999.

(23) Atkins, P.; Friedman, R. *Molecular Quantum Mechanics*; Fourth ed.; Oxford University Press: New York, 2005.

(24) Davydov, A. S. Theory of Absorption Spectra of Molecular Crystals: Translated and reprinted from Zh. Eksp. Teor. Fiz. 18, No. 2, pp. 210–218 (1948). *Ukr. J. Phys.* **2008**, *53*, 65-70.

(25) Dicke, R. H. Coherence in Spontaneous Radiation Processes. *Phys. Rev.* **1954**, *93*, 99-110.

(26) Spano, F. C. The Spectral Signatures of Frenkel Polarons in H- and J-Aggregates. *Acc. Chem. Res.* **2009**, *43*, 429-439.

(27) Potma, E. O.; Wiersma, D. A. Exciton Superradiance in Aggregates: The Effect of Disorder, Higher Order Exciton-Phonon Coupling and Dimensionality. *J. Chem. Phys.* **1998**, *108*, 4894-4903.

(28) Frolov, S. V.; Gellermann, W.; Ozaki, M.; Yoshino, K.; Vardeny, Z. V. Cooperative Emission in p-Conjugated Polymer Thin Films. *Phys. Rev. Lett.* **1997**, *78*, 729-732.

(29) Doan, V.; Tran, V.; Schwartz, B. J. Ultrafast Intensity-Dependent Stimulated Emission in Conjugated Polymers: The Mechanism for Line-Narrowing. *Chem. Phys. Lett.* **1998**, *288*, 576-584.

(30) Scholes, G. D., and Rumbles, G. Excitons in Nanoscale Systems. *Nat. Mat.* **2006**, *5*, 683-696.

(31) Köhler, A.; Bässler, H. What Controls Triplet Exciton Transfer in Organic Semiconductors? *J. Mater. Chem.* **2011**, *21*.

(32) Athanasopoulos, S.; Hoffman, S. T.; Bässler, H.; Köhler, A.; Beljonne, D. To Hop or Not to Hop? Understanding the Temperature Dependence of Spectral Diffusion in Organic Semiconductors. *J. Phys. Chem. Lett.* **2013**, *4*, 1694-1700.

(33) Meskers, S. C. J.; Hübner, J.; Oestreich, M.; Bässler, H. Dispersive Relaxation Dynamics of Photoexcitations in a Polyfluorene Film Involving Energy Transfer: Experiment and Monte Carlo Simulations. *J. Phys. Chem. B.* **2001**, *105*, 9139-9149.

(34) Lim, S. H.; Bjorklund, T. G.; Spano, F. C.; Bardeen, C. J. Exciton Delocalization and Superradiance in Tetracene Thin Films and Nanoaggregates. *Phys. Rev. Lett.* **2004**, *92*, 1074021-1174024.

(35) Roden, J.; Eisfeld, A.; Wolff, W.; Strunz, W. T. Influence of Complex Exciton-Phonon Coupling on Optical Absorption and Energy Transfer of Quantum Aggregates. *Phys. Rev. Lett.* **2009**, *103*, 0583011-0583014.

(36) Hintschich, S. I.; Rothe, C.; Sinha, S.; Monkman, A. P.; de Freitas, P. S.; Scherf, U. Population and Decay of Keto States in Conjugated Polymers. *J. Chem. Phys.* **2003**, *119*, 12017-12022.

(37) Dias, F. B.; Knaapila, M.; Monkman, A. P. Fast and Slow Time Regimes of Fluorescence Quenching in Conjugated Polyfluorene-Fluorenone Random Copolymers: The Role of Exciton Hopping and Dexter Transfer along the Polymer Backbone. *Macromolecules* **2006**, *39*, 1598-1606.

(38) Colaneri, N. F.; Bradley, D. D. C.; Friend, R. H.; Burn, P. L.; Holmes, A. B.; Spangler, C. W. Photoexcited States in Poly(p-phenylene vinylene): Comparison with trans, trans-Distyrylbenzene, a Model Oligomer. *Phys. Rev. B* **1990**, *42*, 11670-11681.

(39) Ikeyama, T.; Azumi, T. Phosphorescence of the trans-Stilbene Single Crystal. *J. Phys. Chem.* **1985**, *89*, 5332-5333.

(40) Shuai, Z.; Beljonne, D.; Silbey, R. J.; Brédas, J. L. Singlet and Triplet Exciton Formation Rates in Conjugated Polymer Light-Emitting Diodes. *Phys. Rev. Lett.* **2000**, *84*, 131-134.

(41) Wilson, J. S.; Dhoot, A. S.; Seeley, A. J. A. B.; Khan, M. S.; Köhler, A.; Friend, R. H. Spin-Dependent Exciton Formation in p-Conjugated Compounds. *Nature (London)* **2001**, *413*, 828-831.

(42) Groff, L. C.; Wang, X. L.; McNeill, J. D. Measurement of Exciton Transport in Conjugated Polymer Nanoparticles. *J. Phys. Chem. C* **2013**, *117*, 25748-25755.

(43) Irkhin, P.; Biaggio, I. Direct Imaging of Anisotropic Exciton Diffusion and Triplet Diffusion Length in Rubrene Single Crystals. *Phys. Rev. Lett.* **2011**, *107*, 0174021-0174024.

(44) Förster, T. Intermolecular Energy Migration and Fluorescence. *Ann. Phys.* **1948**, *437*, 55-75.

(45) Stryer, L.; Haugland, R. P. Energy Transfer - a Spectroscopic Ruler. *Proc. Natl. Acad. Sci. USA* **1967**, *58*, 719-&.

(46) Stryer, L. Fluorescence Energy-Transfer as a Spectroscopic Ruler. *Annu. Rev. Biochem.* **1978**, *47*, 819-846.

(47) Lakowicz, J. R. *Principles of Fluorescence Spectroscopy*; Third ed.; Springer Science+Business Media, LLC: New York, 2006.

(48) Dexter, D. L. A Theory of Sensitized Luminescence in Solids. *J. Chem. Phys.* **1952**, *21*, 836-850.

(49) Wiczk, W.; Eis, P. S.; Fishman, M. N.; Johnson, M. L.; Lakowicz, J. R. Distance Distributions Recovered from Steady-State Fluorescence Measurements on Thirteen Donor-Acceptor Pairs with Different Förster Distances. *J. Fluor.* **1991**, *1*, 273-286.

(50) Akrap, N.; Seidel, T.; Barisas, B. G. Förster Distances for Fluorescence Resonant Energy Transfer Between mCherry and Other Visible Fluorescent Proteins. *Anal. Biochem.* **2010**, *402*, 105-106.

(51) Loudon, R. *The Quantum Theory of Light*; Third ed.; Oxford University Press, 2000.

(52) Monguzzi, A.; Tubino, R.; Meinardi, F. Upconversion-induced delayed fluorescence in multicomponent organic systems: Role of Dexter energy transfer. *Phys. Rev. B* **2008**, *77*.

(53) Scholes, G. D.; Fleming, G. R. On the Mechanism of Light Harvesting in Photosynthetic Purple Bacteria: B800 to B850 Energy Transfer. *J. Phys. Chem. B.* **2000**, *104*, 1854-1868.

(54) Heeger, A. J. 25th Anniversary Article: Bulk Heterojunction Solar Cells: Understanding the Mechanism of Operation *Adv. Mater.* **2014**, *26*, 10-28.

(55) Günes, S.; Neugebauer, H.; Sariciftci, N. S. Conjugated Polymer-Based Organic Solar Cells. *Chem. Rev.* **2007**, *107*, 1324-1338.

(56) Adams, D. M.; Kerimo, J.; O'Connor, D. B.; Barbara, P. F. Spatial Imaging of Singlet Energy Migration in Perylene Bis(Phenethylimide) Thin Films. *J. Phys. Chem. A* **1999**, *103*, 10138-10143.

(57) Chuang, C.-H. M.; Brown, P. R.; Bulovic, V.; Bawendi, M. G. Improved Performance and Stability in Quantum Dot Solar Cells Through Band Alignment Engineering. *Nat. Mat.* **2014**, *13*, 796-801.

(58) Cao, Y.; Parker, I. D.; Yu, G.; Zhang, C.; Heeger, A. J. Improved Quantum Efficiency for Electroluminescence in Semiconducting Polymers. *Nature* **1999**, *397*.

(59) Shen, H.; Cao, W.; Shewmon, N. T.; Yang, C.; Li, L. S.; Xue, J. High-Efficiency, Low Turn-on Voltage Blue-Violet Quantum-Dot-Based Light-Emitting Diodes. *Nano Lett.* **2015**, *15*, 1211-1216.

(60) Meng, L.; Shang, Y.; Li, Q.; Li, Y.; Zhan, X.; Shuai, Z.; Kimber, R. G. E.; Walker, A. B. Dynamic Monte Carlo Simulation for Highly Efficient Polymer Blend Photovoltaics. *J. Phys. Chem. B.* **2010**, *114*, 36-41.

(61) Brabec, C. J.; Sariciftci, N. S.; Hummelen, J. C. Plastic Solar Cells. *Adv. Funct. Mater.* **2001**, *11*, 15-26.

(62) Bakalis, J.; Cook, A. R.; Asaoka, S.; Forster, M.; Scherf, U.; Miller, J. R. Polarons, Compressed Polarons, and Bipolarons in Conjugated Polymers. *J. Phys. Chem. C* **2014**, *118*, 114-125.

(63) Barbara, P. F.; Gesquiere, A. J.; Park, S. J.; Lee, Y. J. Single-Molecule Spectroscopy of Conjugated Polymers. *Acc. Chem. Res.* **2005**, *38*, 602-610.

(64) Yu, J., Wu, C. F., Tian, Z. and McNeill, J. Tracking of Single Charge Carriers in a Conjugated Polymer Nanoparticle. *Nano Lett.* **2012**, *12*, 1300-1306.

(65) Lin, H. Z.; Tabaei, S. R.; Thornsson, D.; Mirzov, O.; Larsson, P. O.; Scheblykin, I. G. Fluorescence Blinking, Exciton Dynamics, and Energy Transfer Domains in Single Conjugated Polymer Chains. *J. Am. Chem. Soc.* **2008**, *130*, 7042-7051.

(66) Tessler, N.; Harrison, N. T.; Friend, R. H. High Peak Brightness Polymer Light-Emitting Diodes. *Adv. Mater.* **1998**, *10*, 64-68.

(67) Lee, C. H.; Yu, G.; Moses, D.; Heeger, A. J. Picosecond Transient Photoconductivity in Poly(p-phenylenevinylene). *Phys. Rev. B* **1994**, *49*, 2396-2407.

(68) Blossey, D. F. Wannier Exciton in an Electric Field. II. Electroabsorption in Direct-Band-Gap Solids. *Phys. Rev. B* **1971**, *3*, 1382-1391.

(69) Barth, S.; Bässler, H. Intrinsic Photoconduction in PPV-Type Conjugated Polymers. *Phys. Rev. Lett.* **1997**, *79*, 4445-4448.

(70) McNeill, J. D.; O'Connor, D. B.; Adams, D. M.; Barbara, P. F.; Kämmer, S. B. Field-Induced Photoluminescence Modulation of MEH-PPV under Near-Field Optical Excitation. *J. Phys. Chem. B.* **2001**, *105*, 76-82.

(71) Yu, J.; Song, N. W.; McNeill, J. D.; Barbara, P. F. Efficient exciton quenching by hole polarons in the conjugated polymer MEH-PPV. *Isr. J. Chem.* **2004**, *44*, 127-132.

(72) Deussen, M.; Scheidler, M.; Bassler, H. Electric-Field-Induced Photoluminescence Quenching in Thin-Film Light-Emitting-Diodes Based on Poly(Phenyl-P-Phenylene Vinylene). *Synth. Met.* **1995**, *73*, 123-129.

(73) Yu, J., Wu, C. F., Sahu, S. P., Fernando, L. P., Szymanski, C., and McNeill, J. Nanoscale 3D Tracking with Conjugated Polymer Nanoparticles. *J. Am. Chem. Soc.* **2009**, *131*, 18410-18414.

(74) Hayer, A., Van Regemorter, T., Höfer, B., Mak, C. S. K., Beljonne, D., and Köhler, A. On the Formation Mechanism for Electrically Generated Exciplexes in a Carbazole-Pyridine Copolymer. *J. Polym. Sci. Part B: Polym. Phys.* **2012**, *50*, 361-369.

(75) Jelley, E. E. Molecular, Nematic and Crystal States of I: I-Diethyl--Cyanine Chloride. *Nature (London)* **1937**, *139*, 631-632.

(76) Jenekhe, S. A.; Osaheni, J. A. Excimers and Exciplexes of Conjugated Polymers. *Science* **1994**, *265*, 765-768.

(77) Wurthner, F.; Kaiser, T. E.; Saha-Moller, C. R. J-Aggregates: From Serendipitous Discovery to Supramolecular Engineering of Functional Dye Materials. *Angew. Chem. Int. Ed.* **2011**, *50*, 3376-3410.

(78) Clark, J.; Silva, C.; Friend, R. H.; Spano, F. C. Role of Intermolecular Coupling in the Photophysics of Disordered Organic Semiconductors: Aggregate Emission in Regioregular Polythiophene. *Phys. Rev. Lett.* **2007**, *98*, 206406-206401-206406-206404.

(79) Maiti, N. C.; Mazumdar, S.; Periasamy, N. J- and H-Aggregates of Porphyrin-Surfactant Complexes: Time-Resolved Fluorescence and Other Spectroscopic Studies. *J. Phys. Chem. B.* **1997**, *102*, 1528-1538.

(80) Chaudhuri, D.; Li, D.; Che, Y.; Shafran, E.; Gerton, J. M.; Zang, L.; Lupton, J. M. Enhancing Long-Range Exciton Guiding in Molecular Nanowires by H-Aggregation Lifetime Engineering. *Nano Lett.* **2011**, *11*, 488-492.

(81) Scheibe, G. Über die Veränderlichkeit der Absorptionsspektren in Lösungen und die Nebenvalenzen als ihre Ursache. *Angew. Chem.* **1937**, *50*, 212-219.

(82) Kometani, N.; Nakajima, H.; Asami, K.; Yonezawa, Y.; Kajimoto, O. Luminescence Properties of the Mixed J-Aggregate of Two Kinds of Cyanine Dyes in Layer-by-Layer Alternate Assemblies. *J. Phys. Chem. B.* **2000**, *104*, 9630-9637.

(83) Köhler, A.; Bässler, H. *Electronic Processes in Organic Semiconductors: An Introduction*; John Wiley & Sons 2015.

(84) Müllen, K.; Scherf, U. *Organic Light-Emitting Devices: Synthesis, Properties and Applications*; John Wiley & Sons, 2006.

(85) Ghoneim, N. Structure of Exciplexes: Solvent and Temperature Dependences of Charge Transfer Character. *Spectrochimica Acta Part A* **2001**, *57*, 483-489.

(86) Stokes, E. D.; Chu, T. L. Diffusion Lengths in Solar Cells from Short-Circuit Current Measurements. *Appl. Phys. Lett.* **1977**, *30*, 425-426.

(87) Donati, D.; Williams, J. O. Exciton Diffusion Lengths for Pure and Doped Anthracene Single-Crystals from Microscopic Measurements. *Mol. Cryst. Liq. Cryst.* **1978**, *44*, 23-32.

(88) Mulder, B. J. Anisotropy of Light Absorption and Exciton Diffusion in Anthracene Crystals Determined from Externally Sensitized Fluorescence. *Philips Res. Rep.* **1967**, *22*, 142-149.

(89) Simpson, O. Electronic Properties of Aromatic Hyrdocarbons. III. Diffusion of Excitons. *Proc. R. Soc. London* **1957**, *238*, 402-411.

(90) Lyons, B. P., and Monkman, A. P. The Role of Exciton Diffusion in Energy Transfer Between Polyfluorene and Tetraphenyl Porphyrin. *Phys. Rev. B* **2005**, *71*, 235201-235205.

(91) Tousek, J.; Touskova, J.; Remes, Z.; Kousal, J.; Gevorgyan, S. A.; Krebs, F. C. Exciton Diffusion Length in Some Thermocleavable Polythiophenes by the Surface Photovoltage Method. *Synth. Met.* **2012**, *161*, 2727-2731.

(92) Lunt, R. R.; Benzinger, J. B.; Forrest, S. R. Relationship between Crystalline Order and Exciton Diffusion Length in Molecular Organic Semiconductors. *Adv. Mater.* **2009**, *22*, 1233-1236.

(93) Gregg, B. A., Sprague, J. and Peterson, M. W. Long-Range Singlet Energy Transfer in Perylene Bis(phenethylimide) Films. *J. Phys. Chem. B.* **1997**, *101*, 5362-5369.

(94) Hofmann, S.; Rosenow, T. C.; Gather, M. C.; Lussem, B.; Leo, K. Singlet Exciton Diffusion Length in Organic Light-Emitting Diodes. *Phys. Rev. B* **2012**, *85*, 245209-245216.

(95) Cross, A. J.; Fleming, G. R. Analysis of Time-Resolved Fluorescence Anisotropy Decays. *Biophys. J.* **1984**, *46*, 45-56.

(96) Beechem, J. M.; Brand, L. Time-Resolved Fluorescence of Proteins. *Annu. Rev. Biochem.* **1985**, *54*, 43-71.

(97) Szymanski, C., Wu, C. F., Hooper, J., Salazar, M. A., Perdomo, A., Dukes, A., and McNeill, J. Single Molecule Nanoparticles of the Conjugated Polymer MEH-PPV, Preparation and Characterization by Near-Field Scanning Optical Microscopy. *J. Phys. Chem. B.* **2005**, *109*, 8543-8546.

(98) Kurokawa, N.; Yoshikawa, H.; Masuhara, H.; Hirota, N.; Hyodo, K. Morphology, fluorescence properties, and their photothermal changes of poly(substituted thiophene) films revealed by near-field fluorescence microspectroscopy. *J. Microsc. Oxford* **2001**, *202*, 420-424.

(99) Colborne, R. S. Precipitation of Polymer Solutions. *J. Polym. Sci.* **1955**, *18*, 55-62.

(100) Yang, Z.; Huck, W. T. S.; Clarke, S. M.; Tajbakhsh, A. R.; Terentjev, E. M. Shape-Memory Nanoparticles from Inherently Non-Spherical Polymer Colloids. *Nat. Mat.* **2005**, *4*, 486-490.

(101) Wu, C. F.; Szymanski, C.; Cain, Z.; McNeill, J. Conjugated Polymer Dots for Multiphoton Fluorescence Imaging. *J. Am. Chem. Soc.* **2007**, *129*, 12904-12905.

(102) Wang, X. L.; Groff, L. C.; McNeill, J. D. Multiple Energy Transfer Dynamics in Blended Conjugated Polymer Nanoparticles. *J. Phys. Chem. C* **2014**, *118*, 25731-25739.

(103) Binnig, G.; Quate, C. F.; Gerber, C. Atomic Force Microscope. *Phys. Rev. Lett.* **1986**, *56*, 930-933.

(104) Rugar, D.; Hansma, P. Atomic Force Microscopy. *Physics Today* **1990**, *43*, 23-30.

(105) Giessibl, F. J. Advances in Atomic Force Microscopy. *Rev. Mod. Phys.* **2003**, *75*, 949-983.

(106) Martin, Y.; Williams, C. C.; Wickramasinghe, H. K. Atomic Force Microscope–Force Mapping and Profiling on a Sub 100Å Scale. *J. Appl. Phys.* **1987**, *61*, 4723-4729.

(107) Sulchek, T.; Yaralioglu, G. G.; Quate, C. F.; Minne, S. C. Characterization and Optimization of Scan Speed for Tapping-Mode Atomic Force Microscopy. *Rev. Sci. Instrum.* **2002**, *73*, 2928-2936.

(108) Zhong, Q.; Inniss, D.; Kjoller, K.; Elings, V. B. Fractured Polymer/Silica Fiber Surface Studied by Tapping Mode Atomic Force Microscopy. *Surf. Sci.* **1993**, *290*, L688–L692.

(109) Yu, C. Y.; Chen, C. P.; Chan, S. H.; Hwang, G. W.; Ting, C. Thiophene/Phenylene/Thiophene-Based Low-Bandgap Conjugated Polymers for Efficient Near-Infrared Photovoltaic Applications. *Chem. Mater.* **2009**, *21*, 3262-3269.

(110) Bazani, D. L. M.; Lima, J. P. H.; de Andrade, A. M. MEH-PPV Thin Films for Radiation Sensor Applications. *IEEE Sens. J.* **2009**, *9*, 748-751.

(111) Snaith, H. J.; Friend, R. H. Morphological dependence of charge generation and transport in blended polyfluorene photovoltaic devices. *Thin Solid Films* **2004**, *451*, 567-571.

(112) Sjöback, R.; Nygren, J.; Kubista, M. Absorption and Fluorescence Properties of Fluorescein. *Spectrochimica Acta Part A* **1995**, *51*, L7-L21.

(113) Weber, G.; Teale, F. W. J. Determination of the Absolute Quantum Yield of Fluorescent Solutions. *Trans. Faraday Soc.* **1957**, *53*, 646-655.

(114) Stewart, W. W. Synthesis of 3,6-Disulfonated 4-Aminonaphthalimides. *J. Am. Chem. Soc.* **1981**, *103*, 7615-7620.

(115) Arzhantsev, S.; Maroncelli, M. Design and Characterization of a Femtosecond Fluorescence Spectrometer Based on Optical Kerr Gating. *Appl. Spectrosc.* **2005**, *59*, 206-220.

(116) Kahlow, M. A.; Jarzeba, W.; DuBruil, T. P.; Barbara, P. F. Ultrafast Emission Spectroscopy in the Ultraviolet by Time-Gated Upconversion. *Rev. Sci. Instrum.* **1988**, *59*, 1098-1109.

(117) Collini, E.; Scholes, G. D. Coherent Intrachain Energy Migration in a Conjugated Polymer at Room Temperature. *Science* **2009**, *323*, 369-373.

(118) Hsu, J. W. P.; Yan, M.; Jedju, T. M.; Rothberg, L. J. Assignment of the Picosecond Photoinduced Absorption in Phenylene Vinylene Polymers. *Phys. Rev. B* **1994**, *49*, 712-714.

(119) Schaffer, J.; Volkmer, A.; Eggeling, C.; Subramaniam, V.; Striker, G.; Seidel, C. A. M. Identification of single molecules in aqueous solution by time-resolved fluorescence anisotropy. *J. Phys. Chem. A* **1999**, *103*, 331-336.

(120) Press, W. H.; Teukolsky, S. A.; Vetterling, W. T.; Flannery, B. P. *Numerical Recipes: The Art of Scientific Computing*; Third ed.; Cambridge University Press: New York, 2007.

(121) O'Connor, D. V.; Ware, W. R.; Andre, J. C. Deconvolution of Fluorescence Decay Curves. A Critical Comparison of Techniques. *J. Phys. Chem.* **1979**, *83*.

(122) Wahl, M. *Technical Note: Time-Correlated Single Photon Counting*; PicoQuant: Berlin, 2014.

(123) Chen, R. Apparent Stretched-Exponential Luminescence Decay in Crystalline Solids. *J. Lumin.* **2003**, *102*, 510-518.

(124) Sun, Y.; Day, R. N.; Periasamy, A. Investigating Protein-Protein Interactions in Living Cells Using Fluorescence Lifetime Imaging Microscopy. *Nat. Prot.* **2011**, *6*, 1324-1340.

(125) Al-Kaysi, R. O.; Ahn, T. S.; Muller, A. M.; Bardeen, C. J. The Photophysical Properties of Chromophores at High (100 mM and Above) Concentrations in Polymers and as Neat Solids. *Phys. Chem. Chem. Phys.* **2006**, *8*, 3453-3459.

(126) Wu, C. F., Bull, B. Christensen, K. and McNeill, J. Ratiometric Single-Nanoparticle Oxygen Sensors for Biological Imaging. *Angew. Chem. Int. Ed.* **2009**, *48*, 2741-2745.

(127) Wu, C. F.; Jin, Y. H.; Schneider, T.; Burnham, D. R.; Smith, P. B.; Chiu, D. T. Ultrabright and Bioorthogonal Labeling of Cellular Targets Using Semiconducting Polymer Dots and Click Chemistry. *Angew. Chem. Int. Ed.* **2010**, *49*, 9436-9440.

(128) Wu, C. F.; Chiu, D. T. Highly Fluorescent Semiconducting Polymer Dots for Biology and Medicine. *Angew. Chem. Int. Ed.* **2013**, *52*, 3086-3109.

(129) Koner, A. L.; Krndija, D.; Hou, Q.; Sherratt, D. J.; Howarth, M. Hydroxy-Terminated Conjugated Polymer Nanoparticles Have Near-Unity Bright Fraction and Reveal Cholesterol-Dependence of IGF1R Nanodomains. *ACS Nano* **2013**, *7*, 1137-1144.

(130) Emelianova, E. V., Athanasopoulos, S., Silbey, R. J., and Beljonne, D. 2D Excitons as Primary Energy Carriers in Organic Crystals: The Case of Oligoacenes. *Phys. Rev. Lett.* **2010**, *104*, 206405-206408.

(131) Kasha, M.; Rawls, H. R.; Ashraf El-Bayoumi, M. The Exciton Model in Molecular Spectroscopy. *Pure Appl. Chem.* **1965**, *11*, 371-392.

(132) Gammill, L. S.; Powell, R. C. Energy-Transfer in Perylene Doped Anthracene-Crystals. *Mol. Cryst. Liq. Cryst.* **1974**, *25*, 123-130.

(133) Powell, R. C.; Kepler, R. G. Evidence for Long-Range Exciton-Impurity Interaction in Tetracene-Doped Anthracene Crystals. *Phys. Rev. Lett.* **1969**, *22*, 636-639.

(134) Burkalov, V. M., Kawata, K., Assender, H. E., Briggs, G. A. D., Ruseckas, A., and Samuel, I. D. W. Discrete Hopping Model of Exciton Transport in Disordered Media. *Phys. Rev. B* **2005**, *72*, 075206-075210.

(135) Hillmer, H.; Hansmann, S.; Forchel, A.; Morohashi, M.; Lopez, E.; Meier, H. P.; Ploog, K. Two-Dimensional Exciton Transport in GaAs/GaAIAs Quantum Wells. *Appl. Phys. Lett.* **1988**, *53*, 1937-1939.

(136) Kelbauskas, L.; Bagdonas, S.; Dietel, W.; Rotomskis, R. Excitation Relaxation and Structure of TPPS4 J-Aggregates. *J. Lumin.* **2003**, *101*, 253-262.

(137) Credo, G. M.; Carson, P. J.; Winn, D. L.; Buratto, S. K. Nanoscale Photophysics of Alq(3) Films. *Synth. Met.* **2001**, *121*, 1393-1394.

(138) Marciniak, H.; Teicher, M.; Scherf, U.; Trost, S.; Riedl, T.; Lehnhardt, M.; Rabe, T.; Kowalsky, W.; Lochbrunner, S. Photoexcitation Dynamics in Polyfluorene-Based Thin Films: Energy Transfer and Amplified Spontaneous Emission. *Phys. Rev. B* **2012**, *85*, 214204-214213.

(139) Bolinger, J. C.; Traub, M. C.; Adachi, T.; Barbara, P. F. Ultralong-Range Polaron-Induced Quenching of Excitons in Isolated Conjugated Polymers. *Science* **2011**, *331*, 565-567.

(140) McNeill, J. D.; Kim, D. Y.; Yu, Z. H.; O'Connor, D. B.; Barbara, P. F. Near Field Spectroscopic Investigation of Fluorescence Quenching by Charge Carriers in Pentacene-Doped Tetracene. *J. Phys. Chem. B.* **2004**, *108*, 11368-11374.

(141) Brouwer, A. M. Standards for Photoluminescence Quantum Yield Measurements in Solution (IUPAC Technical Report). *Pure Appl. Chem.* **2011**, *83*, 2213-2228.

(142) Seybold, G.; Wagenblast, G. New Perylene and Violanthrone Dyestuffs for Fluorescent Collectors. *Dyes Pigm.* **1989**, *11*, 303-317.

(143) Tian, Z. Y.; Yu, J. B.; Wang, X. L.; Groff, L. C.; Grimland, J. L.; McNeill, J. D. Conjugated Polymer Nanoparticles Incorporating Antifade Additives for Improved Brightness and Photostability. *J. Phys. Chem. B.* **2013**, *117*, 4517-4520.

(144) Tvingstedt, K., Vandewal, K., Zhang, F., and Inganäs, O. On the Dissociation Efficiency of Charge Transfer Excitons and Frenkel Excitons in Organic Solar Cells: A Luminescence Quenching Study. *J. Phys. Chem. C* **2010**, *114*, 21824-21832.

(145) Simas, E. R., Gehlen, M. H., Pinto, M. F. S., Siquiera, J., and Misoguti, L. Intrachain Energy Migration to Weak Charge-Transfer State in Polyfluorene End-Capped with Naphthalimide Derivative. *J. Phys. Chem. A* **2010**, *114*, 12384-12390.

(146) Dykstra, T. E., Hennebicq, E., Beljonne, D., Gierschner, J., Claudio, G., Bittner, E. R., Knoester, J., and Scholes, G. D. Conformational Disorder and Ultrafast Exciton Relaxation in PPV-family Conjugated Polymers. *J. Phys. Chem. B.* **2009**, *113*, 656-667.

(147) Campoy-Quiles, M.; Heliotis, G.; Xia, R. D.; Ariu, M.; Pintani, M.; Etchegoin, P.; Bradley, D. D. C. Ellipsometric Characterization of the Optical Constants of Polyfluorene Gain Media. *Adv. Funct. Mater.* **2005**, *15*, 925-933.

(148) Haugeneder, A.; Neges, M.; Kallinger, C.; Spirkl, W.; Lemmer, U.; Feldmann, J.; Scherf, U.; Harth, E.; Gugel, A.; Mullen, K. Exciton Diffusion and Dissociation in Conjugated Polymer Fullerene Blends and Heterostructures. *Phys. Rev. B* **1999**, *59*, 15346-15351.

(149) List, E. J. W.; Creely, C.; Leising, G.; Schulte, N.; Schluter, A. D.; Scherf, U.; Mullen, K.; Graupner, W. Excitation Energy Migration in Highly Emissive Semiconducting Polymers. *Chem. Phys. Lett.* **2000**, *325*, 132-138.

(150) Shaw, P. E.; Ruseckas, A.; Samuel, I. D. W. Exciton Diffusion Measurements in Poly(3-hexylthiophene). *Adv. Mater.* **2008**, *20*, 3516-3520.

(151) Hennebicq, E.; Pourtois, G.; Scholes, G. D.; Herz, L. M.; Russell, D. M.; Silva, C.; Setayesh, S.; Grimsdale, A. C.; Mullen, K.; Bredas, J. L.; Beljonne, D. Exciton Migration in Rigid-Rod Conjugated Polymers: An Improved Forster Model. *J. Am. Chem. Soc.* **2005**, *127*, 4744-4762.

(152) Dias, F. B.; Knaapila, M.; Monkman, A. P.; Burrows, H. D. Fast and Slow Time Regimes of Fluorescence Quenching in Conjugated Polyfluorene-Fluorenone Random Copolymers: The Role of Exciton Hopping and Dexter Transfer along the Polymer Backbone. *Macromolecules* **2006**, *39*, 1598-1606.

(153) Yu, J.; Hu, D. H.; Barbara, P. F. Unmasking electronic energy transfer of conjugated polymers by suppression of O(2) quenching. *Science* **2000**, *289*, 1327-1330.

(154) Hooley, E. N.; Tilley, A. J.; White, J. M.; Ghiggino, K. P.; Bell, T. D. M. Energy Transfer in PPV-Based Conjugated Polymers: a Defocused Widefield Fluorescence Microscopy Study. *Phys. Chem. Chem. Phys.* **2014**, *16*, 7108-7114.

(155) Hu, D. H.; Yu, J.; Padmanaban, G.; Ramakrishnan, S.; Barbara, P. F. Spatial Confinement of Exciton Transfer and the Role of Conformational Order in Organic Nanoparticles. *Nano Lett.* **2002**, *2*, 1121-1124.

(156) Tenery, D.; Worden, J. G.; Hu, Z. J.; Gesquiere, A. J. Single Particle Spectroscopy on Composite MEH-PPV/PCBM Nanoparticles. *J. Lumin.* **2009**, *129*, 423-429.

(157) Hu, Z. J.; Tenery, D.; Bonner, M. S.; Gesquiere, A. J. Correlation between Spectroscopic and Morphological Properties of Composite P3HT/PCBM Nanoparticles Studied by Single Particle Spectroscopy. *J. Lumin.* **2010**, *130*, 771-780.

(158) Yu, J. B.; Wu, C. F.; Tian, Z. Y.; McNeill, J. Tracking of Single Charge Carriers in a Conjugated Polymer Nanoparticle. *Nano Lett.* **2012**, *12*, 1300-1306.

(159) Yu, J. B.; Wu, C. F.; Sahu, S. P.; Fernando, L. P.; Szymanski, C.; McNeill, J. Nanoscale 3D Tracking with Conjugated Polymer Nanoparticles. *J. Am. Chem. Soc.* **2009**, *131*, 18410-18414.

(160) Wu, C. F.; Bull, B.; Christensen, K.; McNeill, J. Ratiometric Single-Nanoparticle Oxygen Sensors for Biological Imaging. *Angew. Chem. Int. Ed.* **2009**, *48*, 2741-2745.

(161) Chan, Y. H.; Wu, C. F.; Ye, F. M.; Jin, Y. H.; Smith, P. B.; Chiu, D. T. Development of Ultrabright Semiconducting Polymer Dots for Ratiometric pH Sensing. *Anal. Chem.* **2011**, *83*, 1448-1455.

(162) Childress, E. S.; Roberts, C. A.; Sherwood, D. Y.; LeGuyader, C. L. M.; Harbron, E. J. Ratiometric Fluorescence Detection of Mercury Ions in Water by Conjugated Polymer Nanoparticles. *Anal. Chem.* **2012**, *84*, 1235-1239.

(163) Wu, C.; Bull, B.; Szymanski, C.; Christensen, K.; McNeill, J. Multicolor Conjugated Polymer Dots for Biological Fluorescence Imaging. *ACS Nano* **2008**, *2*, 2415-2423.

(164) Wu, C. F.; Chiu, D. T. Highly Fluorescent Semiconducting Polymer Dots for Biology and Medicine. *Angew. Chem. Int. Ed.* **2013**, *52*, 3086-3109.

(165) Wang, X. L.; Groff, L. C.; McNeill, J. D. Photoactivation and Saturated Emission in Blended Conjugated Polymer Nanoparticles. *Langmuir* **2013**, *29*, 13925-13931.

(166) Bretschneider, S.; Eggeling, C.; Hell, S. W. Breaking the Diffraction Barrier in Fluorescence Microscopy by Optical Shelving. *Phys. Rev. Lett.* **2007**, *98*, 218103-218101-218103-218104.

(167) Patterson, G.; Davidson, M.; Manley, S.; Lippincott-Schwartz, J. Superresolution Imaging using Single-Molecule Localization. *Annu. Rev. Phys. Chem.* **2010**, *61*, 345-367.

(168) Holzer, W.; Penzkofer, A.; Tillmann, H.; Horhold, H. H. Spectroscopic and Travelling-Wave Lasing Characterisation of Gilch-Type and Horner-Type MEH-PPV. *Synth. Met.* **2004**, *140*, 155-170.

(169) De Leener, C.; Hennebicq, E.; Sancho-Garcia, J. C.; Beljonne, D. Modeling the Dynamics of Chromophores in Conjugated Polymers: The Case of Poly (2-methoxy-5-(2 '-ethylhexyl)oxy 1,4-phenylene vinylene) (MEH-PPV). *J. Phys. Chem. B* **2009**, *113*, 1311-1322.

(170) Kohler, A.; Hoffmann, S. T.; Bassler, H. An Order-Disorder Transition in the Conjugated Polymer MEH-PPV. *J. Am. Chem. Soc.* **2012**, *134*, 11594-11601.

(171) Barbara, P. F.; Gesquiere, A. J.; Park, S. J.; Lee, Y. J. Single-Molecule Spectroscopy of Conjugated Polymers. *Acc. Chem. Res.* **2005**, *38*, 602-610.

(172) Schaller, R. D.; Snee, P. T.; Johnson, J. C.; Lee, L. F.; Wilson, K. R.; Haber, L. H.; Saykally, R. J.; Nguyen, T. Q.; Schwartz, B. J. Nanoscopic interchain aggregate domain formation in conjugated polymer films studied by third harmonic generation near-field scanning optical microscopy. *J. Chem. Phys.* **2002**, *117*, 6688-6698.

(173) Wu, C. F.; McNeill, J. Swelling-controlled polymer phase and fluorescence properties of polyfluorene nanoparticles. *Langmuir* **2008**, *24*, 5855-5861.

(174) Nguyen, T. Q.; Doan, V.; Schwartz, B. J. Conjugated polymer aggregates in solution: Control of interchain interactions. *J. Chem. Phys.* **1999**, *110*, 4068-4078.

(175) Mikhnenko, O. V.; Blom, P. V. M.; Nguyen, T. Q. Exciton Diffusion in Organic Semiconductors. *Energy and Environmental Science* **2015**, *Advance Article*, 1-22.

(176) Yip, W. T.; Hu, D. H.; Yu, J.; Vanden Bout, D. A.; Barbara, P. F. Classifying the photophysical dynamics of single- and multiple-chromophoric molecules by single molecule spectroscopy. *J. Phys. Chem. A* **1998**, *102*, 7564-7575.

(177) Grey, J. K.; Kim, D. Y.; Donley, C. L.; Miller, W. L.; Kim, J. S.; Silva, C.; Friend, R. H.; Barbara, P. F. Effect of temperature and chain length on the bimodal emission properties of single polyfluorene copolymer molecules. *J. Phys. Chem. B.* **2006**, *110*, 18898-18903.

(178) Lee, Y. J.; Kim, D. Y.; Barbara, P. F. Effect of sample preparation and excitation conditions on the single molecule spectroscopy of conjugated polymers. *J. Phys. Chem. B.* **2006**, *110*, 9739-9742.

(179) Kim, D. Y.; Grey, J. K.; Barbara, P. F. A detailed single molecule spectroscopy study of the vibronic states and energy transfer pathways of the conjugated polymer MEH-PPV. *Synth. Met.* **2006**, *156*, 336-345.

(180) Bardeen, C. J. The Structure and Dynamics of Molecular Excitons. *Annu. Rev. Phys. Chem.* **2014**, *65*, 127-148.

(181) Lee, J. H.; Gomez, I. J.; Sitterle, V. B.; Meredith, J. C. Dye-labeled polystyrene latex microspheres prepared via a combined swelling-diffusion technique. *J. Colloid Interf. Sci.* **2011**, *363*, 137-144.

(182) Yan, M.; Rothberg, L. J.; Papadimitrakopoulos, F.; Galvin, M. E.; Miller, T. M. Defect Quenching of Conjugated Polymer Luminescence. *Phys. Rev. Lett.* **1994**, *73*, 744-747.

(183) Yan, M.; Rothberg, L. J.; Kwock, E. W.; Miller, T. M. Interchain Excitations in Conjugated Polymers. *Phys. Rev. Lett.* **1995**, *75*, 1992-1995.

(184) Papadimitrakopoulos, F.; Konstadinidis, K.; Miller, T. M.; Opila, R.; Chandross, E. A.; Galvin, M. E. The Role of Carbonyl Groups in the Photoluminescence of Poly(p-phenylenevinylene). *Chem .Mater.* **1994**, *6*, 1563-1568.

(185) Beljonne, D.; Cornil, J.; Silbey, R.; Millié, P.; Bredás, J. L. Interchain Interactions in Conjugated Materials: The Exciton Model Versus the Supermolecular Approach. *J. Chem. Phys.* **2000**, *112*, 4749-4758.

(186) Bjorklund, T. G.; Lim, S. H.; Bardeen, C. J. Use of picosecond fluorescence dynamics as an indicator of exciton motion in conjugated polymers: Dependence on chemical structure and temperature. *J. Phys. Chem. B.* **2001**, *105*, 11970-11977.

(187) Spano, F. C. Excitons in Conjugated Oligomer Aggregates, Films, and Crystals. *Annu. Rev. Phys. Chem.* **2006**, *57*, 217-243.

(188) Spano, F. C. The Fundamental Photophysics of Conjugated Oligomer Herringbone Aggregates. *J. Chem. Phys.* **2003**, *118*, 981-994.